DYNAMICAL STRUCTURE ANALYSIS OF FIVE BINARY GALAXY CLUSTERS OBSERVED WITH XMM-NEWTON X-RAY OBSERVATORY

by

BURCU BEYGU

B.S., Physics, Istanbul University, 2003

Submitted to the Institute for Graduate Studies in
Science and Engineering in partial fulfillment of
the requirements for the degree of
Master of Science

Graduate Program in Physics
Boğaziçi University
2009

ACKNOWLEDGEMENTS

I am very grateful to my thesis advisor Prof. Dr. E. Nihal Ercan for her support during my Msc. She always encouraged and helped me whenever I was in a difficult situation. I am also thankful to Dr. Murat Hüdaverdi for introducing me clusters of galaxies and for teaching me data analysis.

I would like to thank to my friends Erol Ertan and Kaan Atak for enlightening me in some specific topics related to computation and physics and Selin Manukyan for her support. Finally I am grateful to my parents for their infinite support for my education.

ABSTRACT

DYNAMICAL STRUCTURE ANALYSIS OF FIVE BINARY GALAXY CLUSTERS OBSERVED WITH XMM-NEWTON X-RAY OBSERVATORY

Clusters of galaxies are thought to form by accretion of galaxies along the cosmic filaments, and merging of clusters formed earlier. Observations and hydrodynamic simulations show the strong effects of mergers on physical conditions of Intra Cluster Mediumn (ICM). In this work, we investigate five relatively nearby Abell clusters; A3705 (z= 0.089), A2440 (z= 0.090), A2933 (z= 0.092), A3888 (z= 0.152) and A115 (z= 0.193). Temperature and metal abundance maps are created by wavelet algorithms. Peculiar regions are spectrally studied and large scale deviations are observed. Abell 2440, Abell 2933 and Abell 115 are found to be in ongoing merging phase. One of them, Abell 3888, is found to be in a dynamical state with a possible merging of galaxy groups. Only Abell 3705 is found not to show any merging activity. Our studies are consantrated on individual portions (regions) extensively, thus the X-ray analyses done in this work for their X-ray spectra and temperature maps cover these individual portions, extensively. In this study, Abell 3705, Abell 2440, Abell 2933 and Abell 3888 are studied in a rather extensive way compared to the early work done on these clusters for the first time.

ÖZET

XMM-NEWTON X IŞINI GÖZLEMEVİ TARAFINDAN GÖZLENMİŞ BEŞ İKİLİ GALAXSİ KÜMESİNİN DİNAMİK YAPISININ ANALİZİ

Galaksi kümelerinin, kozmik ağ boyunca galaksilerin yığılmasıve daha önce oluşmuş galaksi kümelerinin bir araya gelmeleri sonucu oluştuklarıdüşünülmektedir. Gözlemler ve hidrodinamik simülasyonlar, kümelerin ve daha kuçuk grupların bir araya gelme süreçlerinin, küme içi gazın (KİG) fiziği üzerinde kuvvetli etkileri olduğuna dair sonuçlar vermektedirler. Bu calımada, görece yakın beş Abell kümesi incelenmiştir; A3705 (z= 0.089), A2440 (z= 0.090), A2933 (z= 0.092), A3888 (z= 0.152) and A115 (z= 0.193). Sıcaklık ve metal bolluğu haritaları"wavelet" algoritması ile yaratılmıştır. Özel bölgeler seçilerek bu bölgelerin spektral analizleri yapılmış ve büyük ölçekteki farklılıklar gözlenmiştir. Abell 2440, Abell 2933 ve Abell 115' in, devam eden etkileşme ve birleşme safhasında oldukları bulunmuştur. Abell 3888 dinamik bir yapı sergilemektedir ve daha küçük ölçekte, galaksi gruplarının muhtemel birleşme safhasında olduğu sonucuna varılmıştır. Yalnızca Abell 3705' in analizinde birleşmeye dair bir bulguya rastlanmamıştır. Bu çalışmada, Abell 3705, Abell 2440, Abell 2933 ve Abell 3888 daha önceki çalışmalara kıyasla oldukça detayl bir ekilde incelenmişlerdir.

TABLE OF CONTENTS

LIST OF FIGURES

LIST OF TABLES

LIST OF SYMBOLS/ABBREVIATIONS

cD	Massive galaxies in the centres of galaxy clusters
h	Parameter incorporating the uncertainty in H_0
H_0	Hubble constant
$L_\odot$	Solar luminosity
$M_\odot$	Solar mass
q_0	Cosmological deceleration parameter
z	Redshift
$Z_\odot$	Metal abundance with respect to Sun
α	Right ascension
δ	Declination
APEC	Astrophysical plasma emission code
CCD	Coupled Charge Device
CMB	Cosmic Microwave Background
CXB	Cosmic X-ray background
EPIC	European Photon Imaging Camera
FWHM	Full width half maximum
ICM	Intra Cluster Medium
MOS	One of the three CCD cameras of the XMM-Newton
obs_id	Observation identity
PSF	Point Spread Function
PN	One of the three CCD cameras of the XMM-Newton
SAS	Science Analysis Software
VLA	Very Large Array
XMM-ESAS	XMM Extended Source Analysis Software
XWSM	The X-ray Wavelet Spectral Mapping

1. INTRODUCTION

Clusters of galaxies are large scale structures in the Universe with radiation powers of the order of $10^{43} - 10^{46} erg.s^{-1}$. They are formed from the gravitational collapse of the field galaxies and the subgroups, covering several Mpc. X-ray observations have provided us a detailed knowledge on the cluster structure, composition, and formation history as well as on the statistics of the galaxy cluster population. Most of our current systematic understanding of clusters of galaxies, the cluster population, the formation of large scale structure and the underlaying cosmological model is based on X-ray observations. Optical point of view defines clusters of galaxies as a only collection of galaxies. But X-ray observations show that clusters of galaxies are continous structures. This appears by the diffuse X-ray emission from the hot intracluster medium (ICM) which is a hot intracluster plasma with temperatures of the order of $10^6 - 10^8 K$. ICM fills the whole volume and determines the shape of the cluster and composes $\sim 10\%$ of the cluster's mass. The K-shell line of iron (Fe Ly-α) is the most prominent line in the X-ray spectrum. Thus X-ray studies of the ICM (temperature distribution, metal abundances, mass, etc) are very important for the understanding of dynamical evolution of the clusters of galaxies [1].

Some clusters show sub-structures or sub-clustering in their X-ray and optical observations. Binary clusters are such clusters which we can see two poles (two subclusters) as a diffuse shape in their X-ray images. X-ray and optical studies of binary clusters give informations about their dynamics, whether they are merging or moving away, etc. ICM is strongly affected by mergers. Strong shocks, rapid rotation, and turbulence are produced in the gas. Temperature analysis gives clues on this merging effects. New generation missions of XMM-Newton and Chandra enables us to map distribution of ICM temperature in detail. In this study, we analyzed XMM-Newton archival data of five nearby binary clusters of galaxies; Abell 3705, Abell 2440, Abell 2933, Abell 3888 and Abell 115 (Table 1.1).

We analysed their temperature distribution in order to examine their dynamical structures. We adopted a Hubble constant $H_0 = 70 km.s^{-1} Mpc^{-1}$, and a cosmological deceleration parameter of $q_0 = 0.5$. All abundances are given relative to solar using the tables of Anders & Grevesse [2].

In the first chapter, the historical and theoretical background of the clusters of galaxies are presented. While writing this chapter I profited deeply from these books and reviews and the references therein; first one is the book about the clusters of galaxies; *X-Ray Emission From Clusters Of Galaxies* by *Craig L. Sarazin* [3] and the second one is an extensive review about the history of the clusters; *From Messier To Abell: 200 Years Of Science With Galaxy Clusters* by *Andrea Biviano* [4]. There are also recently published very two books which I profited: *The Universe In X-Rays* [1] and *Merging Processes In Galaxy Clusters* [5]. The second chapter is about the XMM-Newton X-Ray Observatory. In the third chapter I presented the softwares and methods which are used in the data analysis. The fourth chapter contains the results of our analysis like spectra, temperature maps, images, and finally in the last chapter the results and a comparison of them with the litterature is presented.

Table 1.1. Observation log of the analyzed sources from XMM-Newton archive.

Source	z	α	δ	*obs_id*
Abell 3705	0.089	$20^h42^m00^s.72$	$-35^o13'54''.8$	0203020201
Abell 2440	0.090	$22^h23^m49^s.34$	$-01^o37'48''.3$	0401920101
Abell 2933	0.092	$01^h40^m41^s.05$	$-54^o34'33''.6$	0305060101
Abell 3888	0.152	$22^h34^m34^s.07$	$-37^o43'06''.9$	0404910801
Abell 0115	0.193	$00^h55^m50^s.48$	$+26^o24'43''.1$	0203220101

1.1. Historical Background

Historical background of the clusters of galaxies covers both technological and scientific developments and discoveries in optical, radio and X-ray observations. In this thesis, historical background of clusters of galaxies is described mainly based on Andrea Biviano's article named "*From Messier to Abell: 200 Years of Science With Galaxy Clusters*" and C. L. Sarazin's book "*X-ray Emission from Clusters of Galaxies*". The history of the scientific investigation of galaxy clusters lies back to the 18^{th} century, when the French astronomer Charles Messier and the German astronomer F. Wilhelm Herschel independently produced the first catalogues of nebulae and noticed remarkable concentrations of nebulae on the sky. In 1784, Charles Messier wrote about a clusters of galaxies; *Virgo*, in his catalogue of nebulae called " *Catalogue des nébuleuse et des amas d'étoiles que l'on découvre parmi les étoiles fixes, sur l'horizon de Paris* ".

In his work Messier noticed the remarkable concentration of nebulae in the Virgo constellation. However, his main concern was to define the position of nebulae in order not to misidentify them with new comets. Unlike Messier, after his investigations, Herchel had a diffrent approach to the nebulae which close to the modern understanding of the *Large Scale Structure of the Universe*. In 1785, he came up with idea saying that the *sideral system* where we inhabit is a nebulaea and he explained this in " *On The Construction of Heavens* ". Herchel describes the *Coma cluster of galaxies* as: "*...that remarkable collection of many hundreds if nebulae which are to be seen in what I have called the nebulous stratum of Coma Berenices* "

Hechel classified nearly 250 nebulae and recognized several other nearby clusters and groups of galaxies, such as Leo, Ursa Major, Hydra, NGC 4169 etc. After his death, his son John F.W Herchel continued to investigate the nebulae. He surveyed the southern sky from Cape of Good Hope, and catalogued over 6000 nebulae that in 1864 he collected in his *General Catalogue of Nebulae and Clusters of Stars*. During the first part of the XIX century, J. Herschel noted that the northern hemisphere has an excess of nebulae compared to the southern hemisphere, and he recognized several concentrations of nebulae (in Pisces and Fornax, in particular). He also remarked the existence of the Local Supercluster, with the Virgo concentration “ *being regarded as the main body of this system* ”, and our own Galaxy “ *placed somewhat beyond the borders of its densest portion, yet involved among its outlying members* ”.

In the same period with J. Herchel, d’Arrest and Proctor worked on new positions and finding charts of nebulae in Coma and Virgo clusters and in 1908 Dreyer published the *New General Catalogue* where approximatley 13000 nabulae were listed.

At the beginnig of the 1900’s, photography techniques provided a wide range of studies in astronomy and big steps are made on the investigations of clusters of galaxies. In 1906, Max Wolf made a very detailed description of the Coma and Perseus clusters then in 1918 Curtis added more nebulae to Wolf’s list, reaching a total of 300 nebulae in the Coma cluster. In the early years of 19^{th} century, the main goal of the photographic investigations of nebulae were to understand whether they were extra galactic objects or not. Another objective was to count them: Curtis estimate was 722 000 nebulae in 1918. This number increased to 60 millions nebulae by Hubble in 1936. Edwin Hubble’ s discovery of cepheids in M31 terminated the discussion about the location of nebulae. His work was a clear evidence for the extragalactic nature of nebulae. In the 1920’s he published his paper on the velocity-distance relation for extragalactic nebulae.

With the 1930’s optical research on clusters of galaxies gained a significant speed. Several people came up with very important discoveries, observations, catalogues and so on. It would be appropriate if we state the most crucial ones as Zwicky’s *dark matter*[1] estimate in 1937 [6] and Abell’s catalogue of rich clusters of galaxies in 1958 [7].

Zwicky drived the mass of Coma cluster, via the application of the virial theorem and published it in 1937. This exceptional work, *On The Masses of Nebulae and of Clusters of Nebulae*, is accepted one of the milestones in physics and in the history of clusters of galaxies. In his paper Zwicky clearly noticed that the mass of nebulae, derived from rotaion curves, are underestimated.

Abell's paper, *The Distribution of Rich Clusters of Galaxies*, is another milestone for the history of clusters of galaxies. The term *Abell cluster* used today for rich cluster shows clearly importance of his work. Abell's 2712 clusters were selected on red POSS[1] plates because he realized the advantage of the red band over the blue band for the identification of distant clusters. Abell's radius was subjectively chosen by looking at the projected overdensities of clusters, and yet is close to the cluster gravitational radius. Abell's subjective selection criteria were very well chosen, and even the background subtraction was quite accurate.

The association between radio sources and clusters of galaxies was first made by Mills in 1960 and Van Der Bergh in 1961. Radio emission from Abell clusters at a frequency of 1400 MHz has been surveyed by Owen, Jaffe & Perola and Owen et al. At lower frequencies there are a number of older surveys, as well as an extensive list based on the 4C Cambridge survey. These observations suggested that only sources detected in the inner portions (within 1/3 Abell radii) of the Abell clusters were likely to belong to the cluster, the rest being background objects. Observations at higher frequencies have been made by Andernach et al., Haslam et al. and Waldthausen et al. The more distant Abell clusters were searched for radio emission by Fanti et al., while the richest Abell clusters were observed by Birkinshaw. Jaffe surveyed a sample of high redshift clusters and found evidence of evolution in the radio luminosity of clusters for the range of redshifts $0.25 < z < 0.95$.

Before the launch of X-ray missions, X-ray observations were made with balloon or rocket borne detectors. The fist celestial object seen in X- ray was the sun. In 1966, the first X- ray detection of a cluster source from the region around the galaxy M87 in the center of the Virgo cluster was made by Byram et al. [8] and Bratd et al. [9] in 1966 and 1967, respectively, thus a new era has begun for the studies of clusters of galaxies. M87 is the first object identified as a source of extragalactic astronomical X-ray emission. Five years later the massive nearby clusters in the constellations Coma Berenices and Perseus were detected by Gursky et al. [10] and Fritz et al. [11]. With the launch of the Uhuru Satellite, the extended nature of the cluster X-ray sources could

[1]Palomar Observatory Sky Survey

be established and made a major advance in the study of X- ray clusters. Following X-ray missions like HEAO- 1, Einstein, Rosat and Asca have continued to observe the universe in X-rays. From 1966 to the present day, X-ray observations of clusters of galaxies have been making exceptional contributions in our understanding of these objects. New generation X-ray missions, XMM-Newton, Chandra and Suzaku, with large field of view, high image and energy resolutions keep to acquaint us about the X-ray nature of clusters of galaxies.

1.2. Observation Methods

1.2.1. Optical Observations

Optical observations historicaly are the first way to make astronomical observations and clusters of galaxies are also first studied in optical as explained in the $Historical Background$ chapter. Optical observations are still important for the clusters of galaxies. From optical observations we can measure and calculate physical properties such as redshifts, richness, luminosity functions, velocity of the galaxies in the clusters and mass of the clusters of galaxies. Optical observation is efficient at low and moderate redshifts to detect clusters and is neccesary to confirm the nature of the source. The main problem in optical observation is to distinguish the back and foreground galaxies from those belonging to the cluster, galaxies which are gravitaionaly bound.

1.2.1.1. Redshifts. Redshift is a tool which provide information about distance. It becomes more important as we deal with extragalactic objects. Redshift measurements can be done by photometry and by spectroscopy. First observations in order to calculate redshift and velocity of the galaxies were done by using Doppler Effect from spectroscopy. Figure 1.1 shows shifted spectral lines of calcium for diffrent cluster samples. Redshift measurements by using spectroscopy are usually done from optical observations rather than by X-ray observations because we can detect more photons in the optical domain than in the X-ray domain.

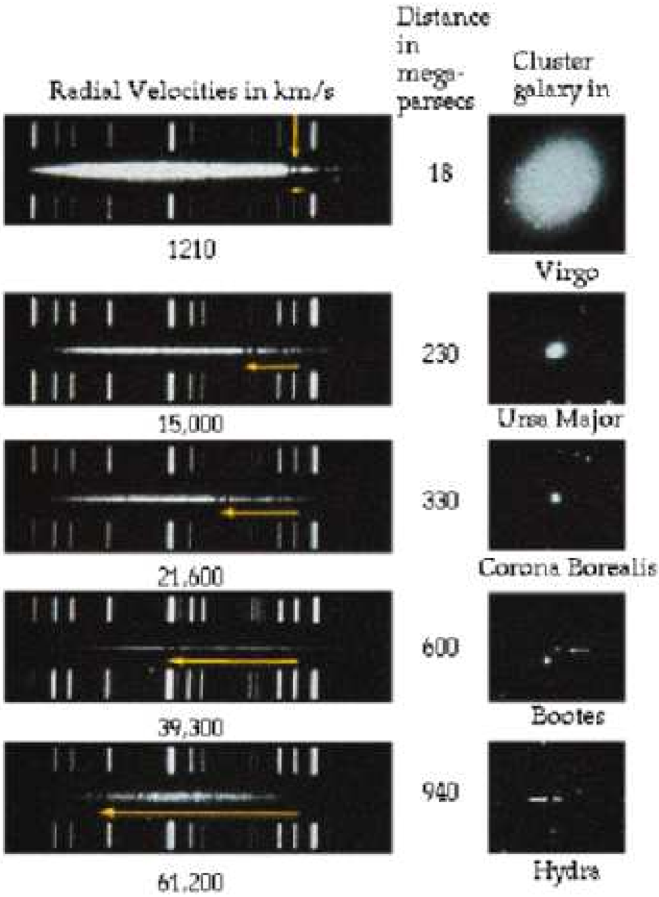

Figure 1.1. The appearance and redshifts of the H and K lines of calcium for five galaxies (Courtesy of Palomar/Caltech)

Photometric redshift measurements are done by the methode of using magnitudes of the first and tenth brightest galaxies [12]. Leir and van den Bergh have given improved estimates of redshifts for 1889 rich Abell clusters, using the magnitudes of the first and tenth brightest galaxies, and an estimate of the cluster radius. Their distance scale is calibrated using measured redshifts for 101 clusters. The photometric distance estimators derived from a larger sample of redshifts can be seen in Sarazin et al. [13]. The clusters in the Abell catalog were assigned to distance groups, based on the redshift estimated from the magnitude of the tenth brightest galaxy in the cluster. Similarly, clusters in the Zwicky catalog were placed in distance groups, based on the magnitudes and sizes of the brightest cluster galaxies.

1.2.1.2. Richness. The richness of a cluster is a measure of the number of galaxies associated with that cluster. Because of the presence of background galaxies, it is not possible to state with absolute confidence that any given galaxy belongs to a given cluster. Richness is a measure of the total number of galaxies that belong to a cluster. It is very difficult to determine the total galaxy populations of a cluster because: It depends on the magnitude limit to which one counts, clusters don't have clear boundaries and there is contamination from back and foreground galaxies.

Zwicky et al. [14] define the richness of their clusters as the total number of galaxies visible on the red Sky Survey plates within the cluster isopleth, the number of background galaxies expected is subtracted from the richness. These richnesses are very dependent on a cluster redshift.

Abell [7] has divided his clusters into richness groups using criteria that are nearly independent of distance that is, the magnitude range and area considered do not vary with redshift.*Richness class* defined by Abell varies from 0 to 5, with 5 being the richest clusters. Just [15] has found a slight richness-distance correlation in Abell's catalog; however, the effect is small and is probably explained by a slight incompleteness (10%) of the catalog for distant clusters [16]. Thus the Abell richnesses are very useful for statistical studies, but must be used with caution in studies of individual clusters.

1.2.1.3. Velocity and Density Profiles. There is a very important distinction between the velocity of a galaxy through space and its recessional velocity. First one is called *peculiar velocity* which is a velocity with respect to the local standard of rest or the random motion of a galaxy with respect to the Hubble recessional velocity. On the other hand *recessional velocity* is related to the expansion of the universe. It is said that the galaxy is being carried along with the surrounding space as the universe expands often called as *Hubble flow*. As we look at distant extragalactic objects, the contribution of their peculiar velocities to the physical velocities diminishes. Another important definition about velocity is the *velocity dispersion* which is the spread of velocities of galaxies in a cluster and it can be estimated by measuring the radial velocities of selected members.

The redshifts are determined from the mean radial velocity of galaxies in a cluster; in fact, the radial velocities of individual galaxies are distributed around this mean. It has been conventional to characterize this distribution by the dispersion σ_r (the mass-weighted radial velocity dispersion) of radial velocities about the mean

$$\sigma_r = \left\langle (v_r - \langle v_r \rangle)^2 \right\rangle^{1/2} \tag{1.1}$$

where v_r is the radial velocity, which is the component of the galaxy velocity along the line-of-sight. However, the velocity dispersion in a given cluster generally decreases with distance from the cluster center; in Coma and Perseus the decline is about a factor of two from the center to the outer edge. Moreover, the velocity dispersion can differ in different clumps of an irregular cluster showing subclustering. The observed mean galaxy velocity $\langle v_r \rangle$ will depend on the projected position in the cluster if the cluster is rotating. The projected shapes of many clusters are substantially flattened.

1.2.1.4. Luminosity Function. The luminosity function of galaxies in a cluster gives the relationship between the luminosities of the galaxies and their distribution between luminosities, number of galaxies in each bin of magnitude. In another words, it is the number of galaxies in the luminosity range $[L, L + dL]$ in a given volume, $N(L)dL$. Schechter' s analytic approximation for the differential luminosity function is

$$\Phi(L)dL = N^*(L/L^*)^{-\alpha} exp(-L/L^*) d(L/L^*) \tag{1.2}$$

where $\Phi(L)$is the number of galaxies with luminosities L to $L+dL$, N^* is a normalisation factor which defines the overall density of galaxies L^* is a characteristic luminosity and α defines the faint-end slope of the luminosity function, α is typically negative implying large numbers of galaxies with low luminosities.

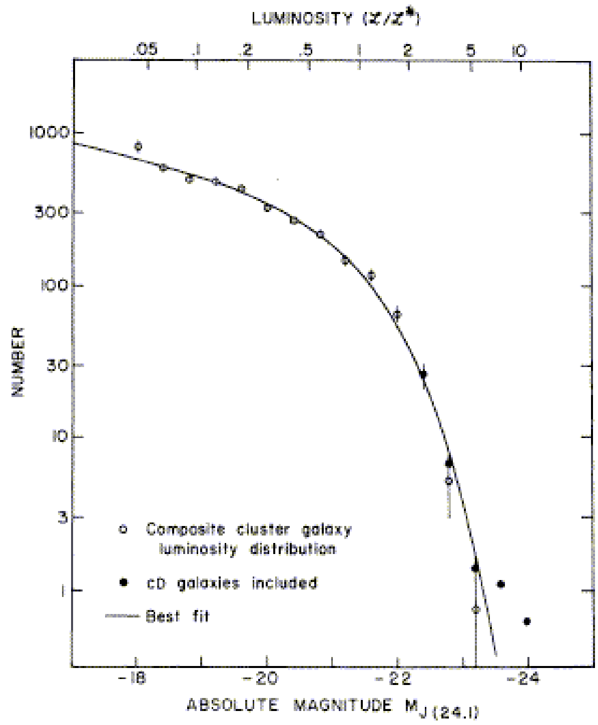

FIG. 2.—Best fit of analytic expression to observed composite cluster galaxy luminosity distribution. Filled circles show the effect of including cD galaxies in composite.

Figure 1.2. A schematic plot of the Schecter function obtained from 13 clusters, [80]

<u>1.2.1.5. Mass.</u> The first thing coming to mind when one mentions about the clusters of galaxies' mass is the *missing mass* (dark matter), first noticed by Zwicky in his milestone paper "*On the Masses Of Nebulae and of Clusters of Nebulae* [6]. In the 30's Hubble & Humason, aiming at a high-redshift extension of the velocity-distance relationship, measured several velocities for galaxies in clusters. In 1931, they provided the first estimates of the velocity dispersions in four clusters of galaxies. Hubble & Humason were interested in cluster velocity dispersions because they wanted to estimate the uncertainties in the cluster mean velocities, which were relevant to the velocity-distance relationship. Hubble & Humason noted that the velocity range spanned by Coma galaxies was larger than in other clusters (Virgo Pegasus, Pisces). This was a first hint of the relation between richness and velocity dispersion later established in 1981 by Bahcall [17]. Zwicky noticed the importance of Hubble & Humason's data and used virial theorem in order to calculate Coma Cluters's mass using Hubble's data set. Zwicky assumed that the clusters of galaxies are bound and self-gravitating systems

and the cluster distribution is stationary. Using virial theorem we get:

$$M_{tot} = \frac{R_G \langle v^2 \rangle}{G} \tag{1.3}$$

$\langle v^2 \rangle$ and R_G can be evaluated from the radial velocity distribution Then

$$\begin{aligned} M_{tot} &= \frac{3R_G\sigma_r^2}{G} \\ &= 7.0 \times 10^{14} M_\odot \left(\frac{\sigma_r}{1000km/s}\right)^2 \left(\frac{R_G}{Mpc}\right) \end{aligned} \tag{1.4}$$

Where σ_r is the mass-weighted radial velocity dispersion. For an average rich cluster $\sigma_r \approx 10^3 km/s$ and $R_G \approx 1Mpc$, inserting these values in the M_{tot} we get

$$M_{tot} \approx 10^{15} M_\odot$$

Another derivation of mass is treating the galaxies as test particles in dynamical equilibrium in the gravitational potential of the cluster assuming the galaxies and the total mass have the same spatial distribution. These calculations's results are generally consistent with the virial theorem determinations.

The problem appears when we look at the mass-to-light ratio of the system. Mass-to-light ratio of an astronomical object is the quotient between the total mass of a spatial volume and its luminosity. Any system composed solely of stars like the Sun would have a mass-to-light ratio of unity. The total luminosity of a cluster is $L_\odot \approx 10^{13} L_\odot$. Using masses derived from virial theorem and magnitudes of the galaxies at visual (V) or blue (B) magnitudes [18], [19] one finds

$$(M/L_V)_{tot} \approx 250 h_{50} M_\odot/L_\odot \quad and \quad (M/L_B)_{tot} \approx 325 h_{50} M_\odot/L_\odot \tag{1.5}$$

and the mass-to-light ratios found for the luminous portions of galaxies range from $(M/L_B)_{gal} \approx (1 - 12))\, h_{50} M_\odot/L_\odot$ with the large values corresponding to the E and S0 galaxies which predominate in compact regular clusters [3]. When we compare the mass of the total system with the mass derived from visible material,luminous portions of galaxies, we see that about 90% of the cluster mass does not originate from the galaxies. This is the so-called *missing mass* problem. It means that there is some amount of material forming about 90% of the cluster's total mass which can not bee seen in the optical wavelength. After the discovery of the X-ray nature of the clusters of galaxies, although it is seen that the hot intra cluster medium (ICM) is a more important mass component than the galaxies it did not solve the missing mass problem. Today we know that mass of a cluster of galaxy is formed $\sim 90\%$ of this missing mass so-called *dark matter* which the nature is still unknown.

Zwicky has also pointed out that for an accurate mass determination one should use *gravitational lensing effect* as the "simplest and most accurate mass determination". He was half a century in advance of observations. The missing mass idea was not accepted so easely by the scientific community. Long time poeple have searched for other explanations. Unfortunatley the general feeling of the scientific community about the dark matter issue was quite negative until 70's.

1.2.2. Radio Observations

The first detection of diffuse and extended radio emission in galaxy clusters dates back to 1959, when Large et al. [20] mapped for the first time the Coma cluster at radio wavelengths, detecting an extended radio source (Coma C) at its centre. The radio emission from clusters of galaxies (as well as most other extragalactic objects) is synchrotron emission due to the interaction of a nonthermal population of relativistic electrons with a magnetic field. Such nonthermal synchrotron emission generally has a spectrum in which the intensity $I_\nu(erg/cm^2Hzs)$ is well represented as a power-law over a wide range of frequencies ν

$$I_\nu = \nu^{-\alpha_r} \tag{1.6}$$

where α_r is the radio spectral index. Cluster radio sources generally have steeper radio spectra (values of $\alpha_r 1$) than radio sources in the field [21], [22], [23], [24].

Apart from their common properties (nature of the emission, steep radio spectra), diffuse and extended radio sources in clusters differ in their physical properties, in particular: size, position in the host cluster, intensity of polarised signal, morphology and association to other cluster physical properties (e.g. dynamical state, presence of a cooling flow). A working definition assigns cluster diffuse radio sources to three main classes: halos, relics and mini-halos [25]. Very schematically:

- Radio halos are extended ($\gtrsim$1 Mpc) diffuse radio sources at the centre of clusters, with a quite regular morphology, similar to the X-ray morphology of the system. Figure 1.3 shows 20 cm radio contours overlaid on the deep, R-band image [26] of the galaxy cluster Abell 2163, hosting one of the most extended and powerful halos known so far.

- Radio relics have similar extensions and are also detected in merging clusters, but usually they are located in the cluster outskirts and they have an elongated morphology. Figure 1.5 shows,from top to bottom, VLA image at 1.4 GHz of the "AGN relic" source in Abell 133 (z = 0.056), close to the radio emitting cD galaxy at the cluster centroid [27], VLA image at 1.4 GHz of the "Phoenix" source in the periphery of Abell 85 (z = 0.055) [27], X-ray contours (ROSAT data, 0.1-2.4 keV energy band) overlaid on the 843 MHz Molonglo Observatory Synthesis Telescope (MOST) image of A 3667 (z = 0.056) [28].

- Radio mini-halos are smaller sources ($\lesssim$ 500 kpc) located at the centre of cooling flow clusters. They surround a powerful radio galaxy. Figure 1.4 shows 327 MHz map of the mini-halo in the Perseus Cluster. The source is centred on the position of the cD galaxy NGC 1275 (indicated with a cross). The inset shows radio contours overlaid on the X-ray image of the central $1'$ region of Perseus [29], [30].

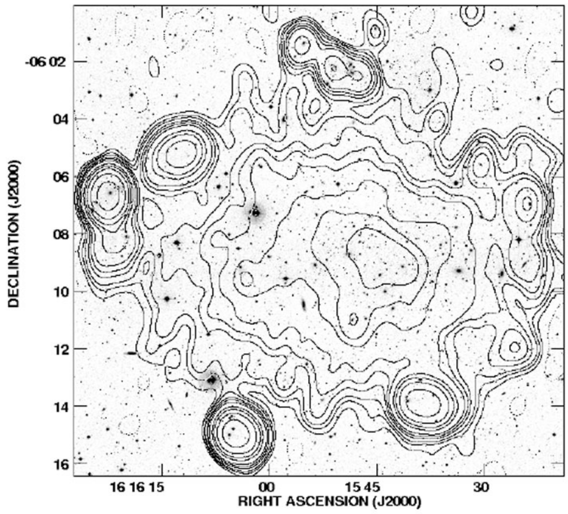

Figure 1.3. Radio halos observed in A 2163 (z= 0.203), [26].

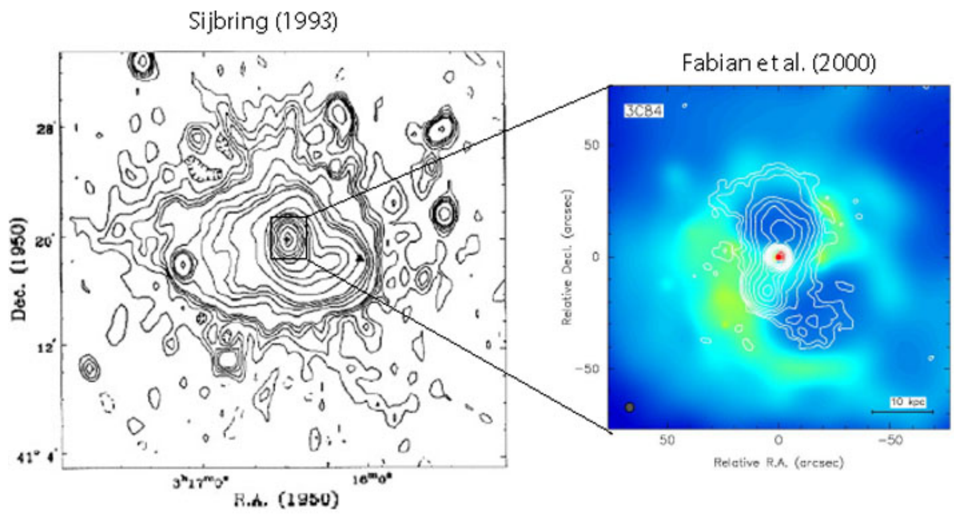

Figure 1.4. Map of the mini halo observed in Perseus Cluster (z = 0.018), [29], [30]

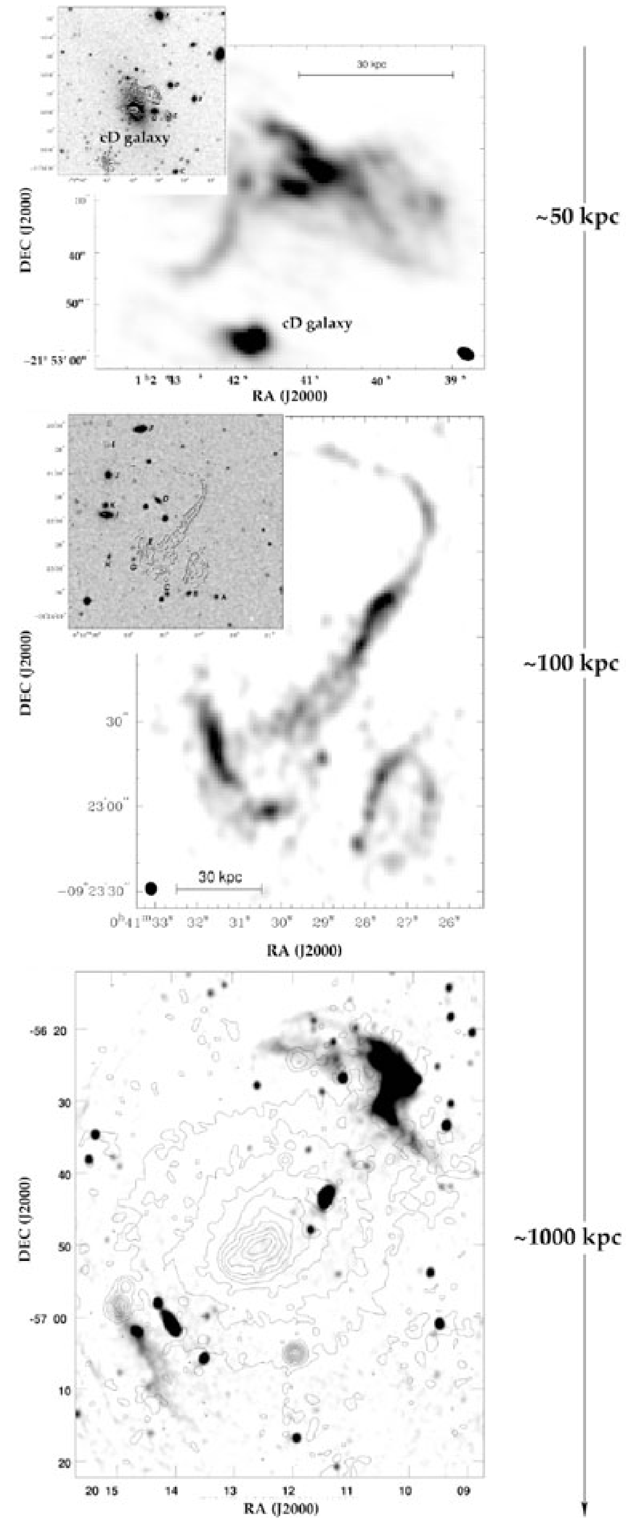

Figure 1.5. Examples of different diffuse radio sources in clusters classified as "radio relics ", [27]

1.2.3. X-Ray Observations

X- ray observations of clusters of galaxies have changed dramatically our understanding about these objects. Optical observations have been presenting clusters only as a group of indivudial objects (galaxies), however via the X- ray observations we see that they are "continous" structures and their boundaries are not clear. Optical surveys suffer from contamination - galaxies in front of and behind the cluster (but not part of the gravitationally bound group) can look like part of the cluster. This makes it difficult to detect rich clusters at high redshifts and poor clusters or groups at any redshifts. These problems can be avoided by using X-ray based surveys. X-ray surveys detect clusters based on emission from the hot gas in between the galaxies of the cluster. Observing the clusters in this way has several advantages: the X-ray emitting intracluster gas is much brighter than the background and is easily distinguished from the unresolved X-ray background. The presence of the X-ray gas guarantees the cluster is bound, and the observations are only limited by the exposure time, and not by the number of galaxies visible in the cluster.

Especially X-ray images of the clusters show clearly this continuous structure. These observations established a number of properties of clusters of galaxies. First, The medium among the galaxies forming a cluster is filled with hot plasma called *intra cluster medium* (ICM) which gives the main shape of the cluster and is the second massive constituent of a cluster of galaxies after the dark matter (the galaxies are the less ones). Second, X- ray luminousity of the ICM makes the clusters of galaxies the most X- ray luminous objects in the universe with radiation powers of the order of 10^{43}- 10^{46} ergs/s apart from quasars. Third, clusters of galaxies's sizes range from 1 to 10 Mpc. Forth, the X-ray emission from clusters is not time variable, as is the emission from many point sources of X-rays in our galaxy or in the nuclei of other galaxies. These results suggest that the emission is truly diffuse, and not the result of one or many compact sources. Today the simplest definition of a cluster of galaxies is that this is a sytem comprising the individual galaxies, a hot plasma occupying the space between the galaxies, and the dark matter providing most of the mass.

1.2.3.1. ICM, X-Ray Emission Processes and Spectrum . What we see in X-ray looking to the clusters of galaxies is the ICM. It is a hot plasma with temperatures of $10^6 - 10^7 K$ and densities of $10^{-2} - 10^{-5} electrons/cm^{-3}$. X-ray images and spectra of the clusters of galaxies give information basically about the brightness profile, mean temperature and metal abundances of these objects. Thus X-ray studies of ICM are very important in order to understand dynamical structures of the clusters of galaxies.

The main emissiom mechanism of clusters is thermal Bremsstrahlung from hot diffuse gas (ICM) [31] under the assumption of the particles populating the emitting plasma are at a uniform temperature and are distributed according to the Maxwell-Boltzman velocity distribution. The total emission by all particles in this population is called *thermal bremsstrahlung*. Bremsstrahlung (free- free radiation) is the process by which electrons radiate as they pass throug the attractive Coulomb field of the positive ions in the plasma. Hot gases at temperatures about 10^7 K emit Bremsstrahlung X-rays if they are optically thin. Optically thin implies that the gas is insufficiently thick and dense to absorb appreciably its own radiation. This means thatthe spectrum of X- rays observed is the same as the spectrum during their production. A hot gas emits principally by three processes 1) Bremsstrahlung, bound-bound emission, and free- bound emission. The last two processes involve the presence of atoms with at least some of theirs electrons remaining in bound orbits about the nucleus. Gaseous plasmas with normal astrophysical abundence of the elements are almost completely ionised at temperatures about 10^7 K. Therefore, the major emission process needs to be considered is Bremsstrahlng. Observed spectra show exponential decrease at high frequencies that is characteristic of bremsstrahlung. The emissivity (total emitted power ϵ_ν^{ff} in the cloud per unit volume) at a frequency ν of an ion of charge Z in a plasma with an electron temperature T_g is given by

$$\epsilon_\nu^{ff} = \frac{2^5 \pi e^6}{3 m_e c^3} \left(\frac{2\pi}{3 m_e k} \right)^{1/2} Z^2 n_e n_i g_{ff} \left(Z, T_g, \nu \right) T_g^{-1/2} exp \left(-\frac{h\nu}{kT_g} \right) \tag{1.7}$$

where $''ff``$ stands for $''free - free''$ (the electrons and protons are moving freely in the interection, i.e. they are not *bound* into other system), n_i and n_e are the number density of ions and electrons, respectively, $g_{ff}(Z, T_g, \nu)$ is the Gaunt corrections for quantum mechanical effects and for the effect of distant collisions which is of order unity over a wide range of temperature and density conditions. This spectrum cuts off in ν at approximately $h\nu/kT$, so the cut off is a useful means of determining the temperature of the plasma.This equation predicts that the emission from clusters should fall off rapidly at high frequencies. In cgs units the power emitted per cubic cm is

$$\epsilon_\nu^{ff} = 1.4 \times 10^{-27} T^{1/2} n_e n_i Z^2 g_B \tag{1.8}$$

where g_B is the frequency averaged gaunt factor for the thermal distribution of velocities, and is order of unity.

XMM-Newton, Chandra and Suzaku X-ray missions with high spectral resolutions permit us to observe and distinguish several heavy elements in the cluster spectra. Typical emission line observed from clusters of galaxies in X-ray is the K-shell line of iron (Fe Ly-α, n= 1 state) seen at the 6.5 - 7 keV range of the spectrum. Iron line was the first element detected in the X-ray spectrum of a cluster of galaxies (in Perseus cluster by Mitchell et al. [32]). Typical iron abundances are in the range of 0.3 - 0.5 with respect to the sun. Other heavy elements with strong enough lines to be observed are O, Ne, Mg, Si, S, Ar, Ca and Ni. The Fe K-shell lines have large equivalent widths and are in an isolated part of the spectrum so Fe is observationally easy and reliable to measure. Si, S, Ar, and Ca are all in isolated parts of the spectrum but have smaller equivalent widths so these are reliable but harder to measure. O, Mg, and Ne are in the energy range dominated by the Fe L-shell lines. With current X-ray spectrometer resolutions these elements cannot be measured independently of the iron lines. Thus, abundance measurements for these elements are more susceptible to systematic problems. Ni measurements should be reliable but the Ni K lines have smaller equivalent widths than Fe K and current telescopes and detectors have low efficiencies in this energy range. Figure 1.8 is an example of a cluster spectrum, Abell 496 observed with ASCA, which shows clearly Ne, Mg, Si,S, Ar, Ni and the famous Fe-K lines.

One has to remember that the observed spectrum is a projection of thermal emission along the line of sight because our observation is 2-dimensional but the cluster is a three dimensional object so determining the temperature gradients within the ICM is not easy.

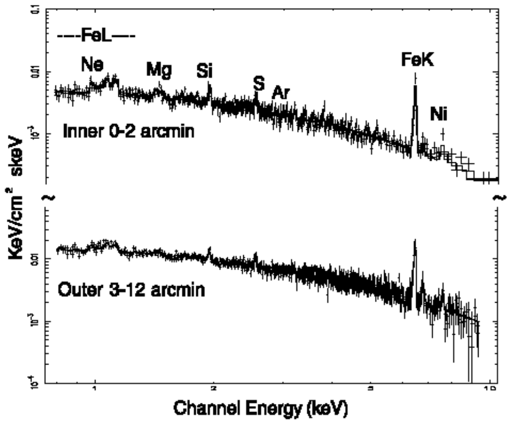

Figure 1.6. ASCA spectra of the inner and outer regions of Abell 496, [81]

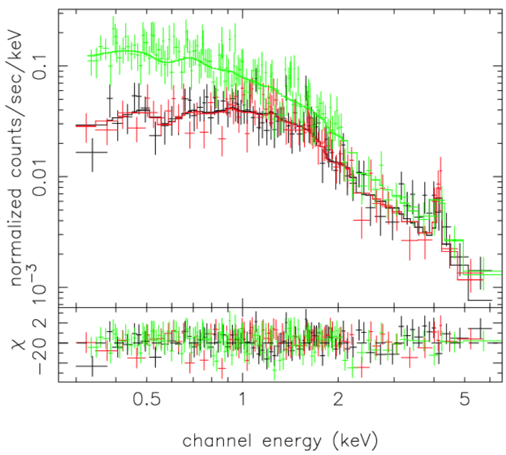

Figure 1.7. An example of EPIC spectra of galaxy cluster, [82]

Today, we know two sources for the enrichment of the ICM with heavy elements, the first one is the core collapse supernovae, type II, and the second is the thermonuclear explosions of white dwarfs, type Ia supernovae. Supernovae type II produce elements like O and Mg and supernovae type Ia produce Fe group elements and lighter elements like Si and S but very little O and Mg. [1], [3].

<u>1.2.3.2. Mass.</u> X-ray emission is proportional to the squared plasma density (there is a weak dependence on temperature) and ICM density can be reconstructed from

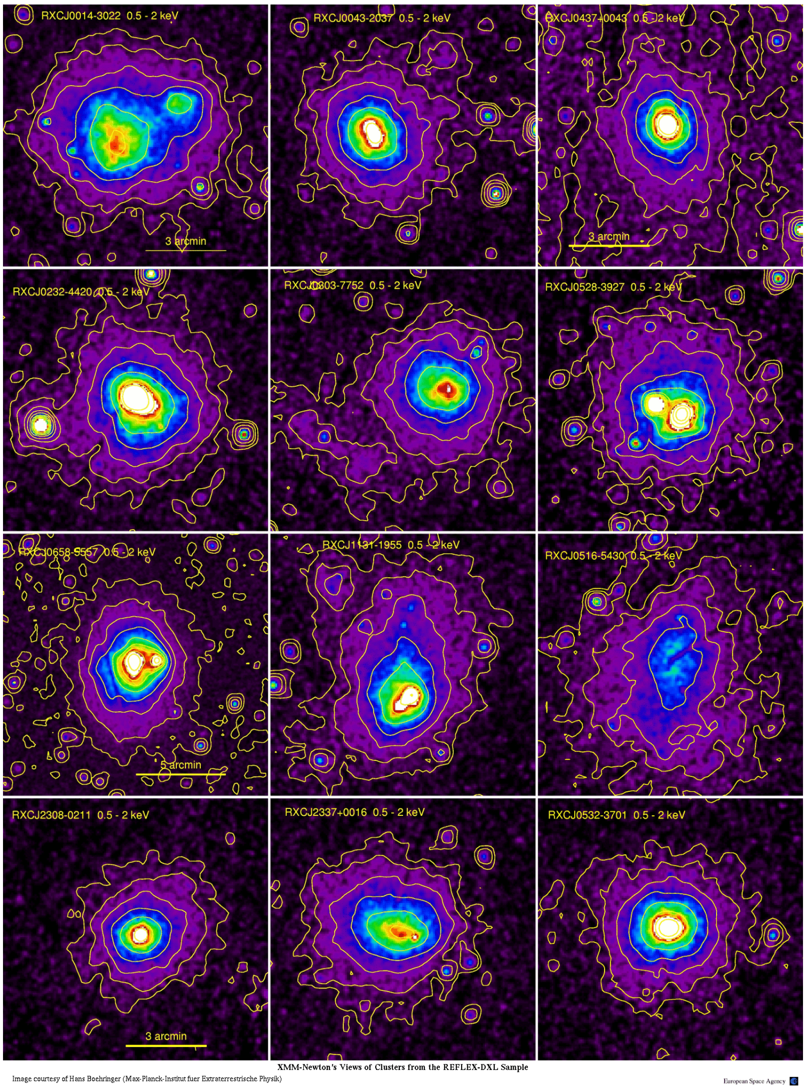

Figure 1.8. XMM-Newton's EPIC views of REFLEX-DXL galaxy clusters, with contours superimposed. Photo, ESA/XMM-Newton

the observed X-ray images. The X-ray method of mass determination is based on the assumption that the ICM constitutes an atmosphere, which is approximately in hydrostatic equilibrium in the cluster potential described by the equation

$$\frac{1}{\rho}\nabla P = \frac{-GM(r)}{r^2} \tag{1.9}$$

In most cases a spherically symmetric approximation is used and justified. Substituting the ideal gas law, $P = \frac{\rho k_B T}{\mu m_p}$ for the pressure P, assuming constant μ and solving for the cluster mass profile, the equation can be reformulated to yield

$$M(r) = -\frac{k_B T(r)}{G\mu m_p} r \left(\frac{dlog\rho}{dlogr} + \frac{dlogT_X}{dlogr} \right) \tag{1.10}$$

where m_p is the proton mass and μ is the mean molecular particle weight (~ 0.6 for a nearly fully ionized ICM plasma). The observables required for this equation are the absolute temperature profile $T_X(r)$ and the shape of the density profile $\rho(r)$, which are both obtained from X-ray observations (spectroscopy). Note that $M(r)$ is the total interior mass, both luminous and dark. Another mass measurement method is the gravitational lensing. There are some publications stating that the masses inferred from strong gravitaional lensing tend to be larger than those determined from X-ray observations [33].

<u>1.2.3.3. The X-Ray Luminosity Function.</u> The X-ray luminosity of clusters of galaxies are closely related to the cluster mass and is a function of gas density and temperature

$$L_X = n_e n_i T^{1/2} = \rho_{gas}^2 T_{gas}^{1/2} \tag{1.11}$$

where n_e and n_i are electron and ion densities, respectively. The X-ray luminosity function, the number of clusters per unit volume with X-ray luminosities in the range L_X to $L_X + dL_X$, provides a good estimate of the mass function of clusters of galaxies [34].

<u>1.2.3.4. The X-Ray Luminosity- Temperature Relation.</u> The X-ray luminosity- temperature ($L_X - T$) relation of galaxy clusters is one of the most fundamental parameter correlations, established from previous X-ray observations. Since the X-ray luminosity reflects temperature and density profiles of ICM, $L_X - T$ relation should contain information on the physical status and evolution of the ICM [35]. Observationally, the correlation is well approximated with a power- law function: $L_X \propto T^\alpha$, with $\alpha \sim 3$ [36],[37].

1.3. Classification

There are severals point of views for the classifications of clusters of galaxies according to their morphological properties. But in the first step we can divide the clusters of galaxies simply in two categories; *regular* and *irregular clusters* as Abell did [38], [39]. Table 1.2 shows briefly the main features of these two categories.

There are also morphological classifcations done by several scientifics, the most commons types are the Zwicky type [14], Bautz and Morgan (BM) type [40], Rood-Sastry (RS) type [41] and Oemler type [42] of clusters (see Table 1.3).

Zwicky classified clusters as compact, medium compact, and open. A compact cluster has a single significant concentration of galaxies, with more than ten galaxies appearing in contact as seen on the plate. A medium compact cluster has either a single concentration with ten galaxies separated by roughly their own diameters, or several concentrations. An open cluster lacks any pronounced concentration of galaxies.

Table 1.2. Two main categories of clusters of galaxies

Property	**Regular Clusters**	**Irregular Clusters**
Symmetry	High spherical symmetry	Little or no symmetry
Concentration	High concentration of members toward cluster center; show high richness	No marked concentration to a unique cluster center often two or more nuclei of concentration are present; show low richness
Types of galaxies	Often dominated by cD galaxies; all or nearly all galaxies in the first 3 or 4 magnitude intervals are elliptical and/or S0 galaxies	All types of galaxies are usually present except in poor groups, which may not contain giant ellipticals Late-type spirals and/or irregular galaxies present
Number of galaxies	Order of 10^3 or more	Order of 10 to 10^3
Subclustering	None or unimportant	More than one cores are present
X-ray luminosity	High	Low
Radio emission	%50	%20
Examples	Coma cluster; Corona Borealis cluster	Virgo cluster, Hercules cluster

Table 1.3. Morphological classification

Type	**Regular**	**Intermediate**	**Irregular**
Zwicky	Compact	Medium-compact	Open
Bautz-Morgan	I, I-II, II	II, II-III	II-III, III
Rood-Sastry	cD, B, L, C	L, C, F	F, I
Oemler	cD,spiral-poor	Spiral-poor	Spiral-rich

Bautz-Morgan classification scheme is based on brightest glaxy in cluster. *Type I* clusters have centrally located cD galxy, massive galaxies in the centres of galaxy clusters, *type II* cluster's central galaxy is somewhere between a cD and giant elliptical galaxy and *type III* clusters have no dominat central galaxy. Morgan [43] also classified clusters as type i if they contained large numbers of spirals and as type ii if they contained few spirals. Rood and Sastry classification is based on the projected distribution of the brightest 10 members. They recognize these types:

cD - single dominant cD (elliptical) galaxy (A2029, A2199)

B - dominant binary, like Coma

L - linear array of galaxies (Perseus)

C - single core of galaxies

F - flattened (IRAS 09104+4109)

I - irregular distribution (Hercules)

Oemler classified clusters by galaxy content; the fraction of cluster galaxies which are spirals (S), disk galaxies without spiral structure (S0s), or elliptical (Es). He also defined three classes of clusters; spiral-rich clusters, in which spirals (S) are the most common galaxies; spiral-poor clusters, in which spirals are less common and S0s are the most common galaxies; and cD clusters, which are dominated by a central cD galaxy and in which the great majority of galaxies are ellipticals or S0s.

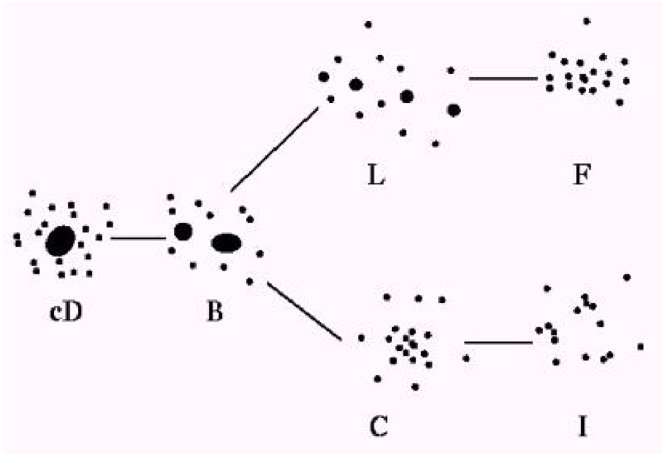

Figure 1.9. The Rood-Sastry cluster classification scheme

- cD clusters: 1 or 2 dominat cD galaxies, E:S0: $\sim$ 3:4:2
- Spiral rich: E:SO:S $\sim$ 1:2:3 (smilar to the field)
- Spiral poor: no dominant cD, E:S0:S $\sim$ 1:4:2

1.4. Merging Clusters of Galaxies

According to the standard model of hierarchical growth of large-scale structure small mass aggregates collapse and form galaxy clusters by the inhomogeneous accretion of matter. Mass units of various mass fall into the cluster potential and if these mass units are large enough they are observed as clusters mergers [1], [5].

As mentioned in the section 1.2.3 $X - Ray\ Observation$, the X-ray spectrum of the ICM displays emission lines of heavy elements. This indicates that the gas has been processed through stars in the cluster, so how did this mass escape from the clusters of galaxies? Another interesting subject is the galaxy evolution in the cluster or the predominance of early-type galaxies in a cluster. A possible solution for these problems is the merging scenerio of the clusters [5].

To identify merging clusters of galaxies first of all we need multi-wavelength research, especially optical and X-ray observations. Mainly we look for sub-structure (sub-cluster) signs both in optical and X-ray images (surface densities). In X-rays it is relatively easier to identify substructures, because diverse ICM concentrations are clearly seen on the X-ray image. Also density distributions of galaxies, gas and darkmatter are compared. Velocity distribution, mass ratios of the sub-clusters are examined. And finally temperature gradients in the ICM are investigated.

In this thesis, one had to focuse on creating temperature maps of the samples in order to see and compare temperature diffrences between substructures. Therefore, one has to start searching for deviations from regularity in physical properties like morphology, temperature and velocity distributions etc. Figure 1.10 is an illustrative example showing a simulation of temperature changes in the ICM during the different phases of merging. Time scale is between t=3.5 Gyr to t=7 Gyr (from top-left to bottom-right).

Cluster mergers with their huge release of gravitational binding energy ($\sim 10^{64}$ ergs) effects intensely the physics of the cluster medium in many aspects; temperature, metallicity, density distribution of the ICM, spatial distribution of galaxies and their star formation rates.

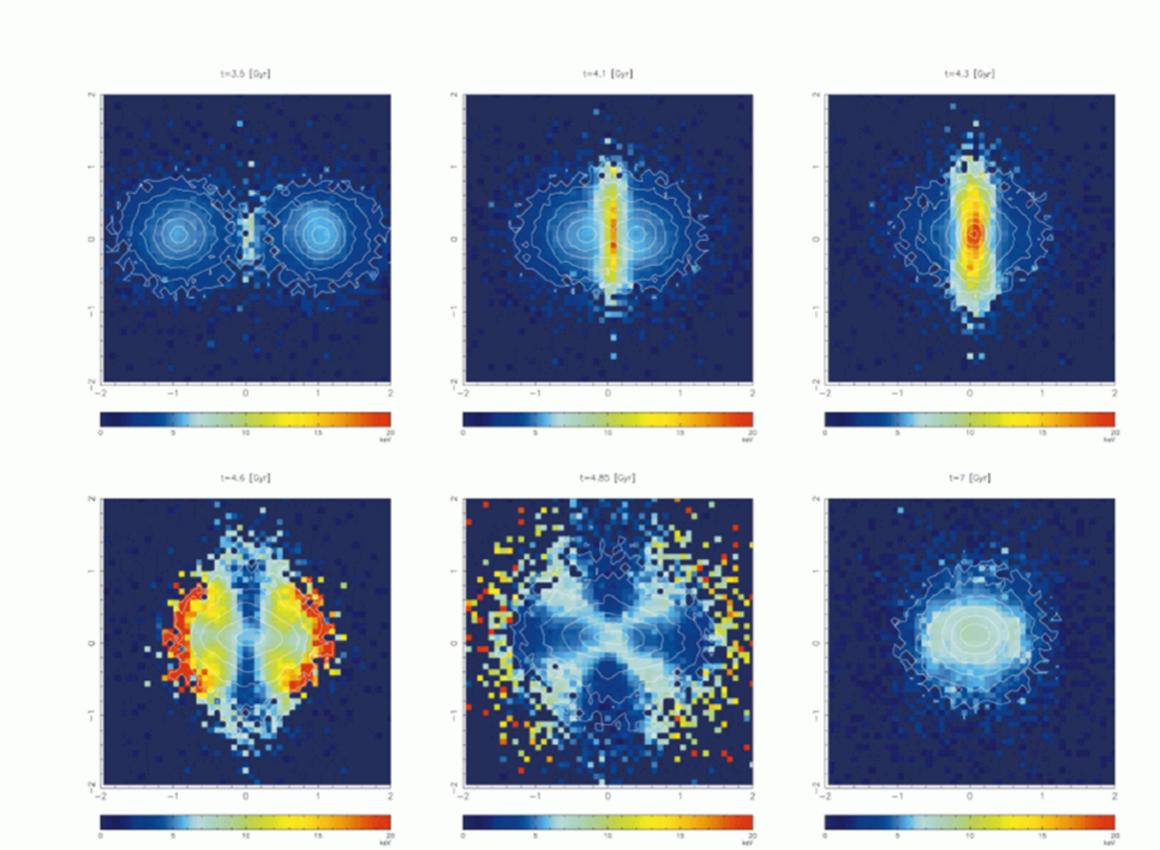

Figure 1.10. Temperature changes with time, Takizawa, 1999, taken from S. Maurogordato's presentation "Merging Clusters of Galaxies: An Optical View "

2. XMM-NEWTON X-RAY OBSERVATORY

XMM-Newton, *XMM* is for *X-Ray Multi Mirror*, is the second of ESA's four "cornerstone" missions defined in the Horizon 2000 Programme. It was launched on December 10th, 1999 and carries two distinct types of telescope: three Wolter type-1 X-ray telescopes, with different X-ray detectors in their foci and a 30-cm optical/UV telescope with a microchannel-plate pre-amplified CCD detector in its focal plane. Thus, XMM-Newton offers simultaneous access to two windows of the electromagnetic spectrum. Figure 2.1 shows different components of the XMM spacecraft and its payloada general, for further information visit the XMM-Newton website [44].

2.1. Spacecraft

2.1.1. Components

The XMM-Newton satellite is configured modularly and is composed of four main elements:

- The Focal Plane Assembly (FPA), consisting of the Focal Plane Platform (FPP) carrying the focal-plane instruments: two Reflection Grating Spectrometer (RGS) readout cameras, an EPIC PN and two EPIC MOS imaging detectors, and the data handling and power distribution units for the cameras. The EPIC and RGS instruments are fitted with radiators, which cool the CCD detectors via cold fingers.

- The Telescope Tube (a long carbon fibre tube), maintaining the relative position between the FPA and the MSP. Due to its length of 6.80 m, the Telescope Tube is physically composed of two halves: the upper and lower tubes. The upper tube includes two reversible venting and outgassing doors (VOD), and supports the outgassing baffle (OGB).

- The Mirror Support Platform (MSP), consisting of the platform itself and carrying the three mirrors assemblies (Mirror Modules + entrance and exit baffles + doors + two RGS grating boxes), the Optical Monitor (OM) and the two star-trackers.

- The Service Module (SVM), which carries the spacecraft subsystems and associated units providing the necessary resources to the satellite. Also attached to the SVM are the two solar-array wings, the Telescope Sun Shield (TSS) and the two S-band antennas mounted on their booms.

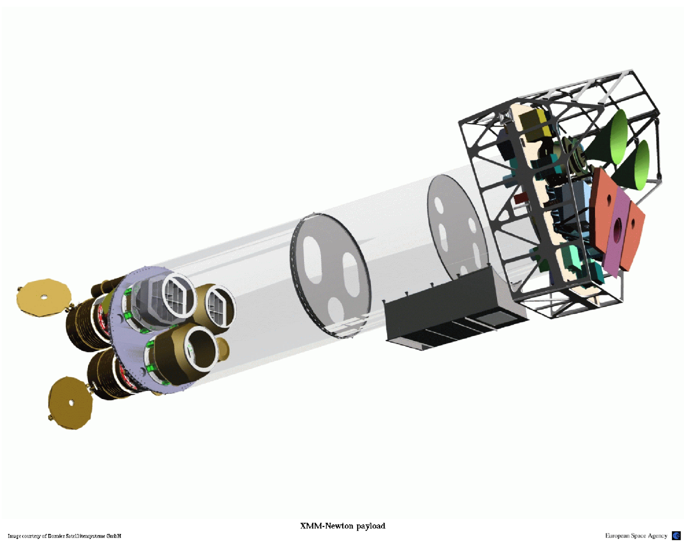

Figure 2.1. XMM-Newton payload. Illustration, ESA/XMM-Newton

In the Figure 2.1 one can see The X-ray telescopes, two with Reflection Grating Arrays, at the lower left. At the right end of the assembly, the focal instruments are shown: The EPIC-MOS cameras with their radiators (black/green ”horns”), the radiator of the EPIC-pn camera (violet) and those of the (light blue) RGS receivers (in orange). The black box at the bottom of the bus is the outgassing device.

2.1.2. XMM-Newton Orbit

XMM-Newton was launched on the 10th December 1999 by an Ariane 5 launcher into a highly elliptical orbit, with an apogee of about 115,000 km and a perigee of ca. 6000 km. XMM-Newton is operated with three ground stations, located at Perth, Kourou and Santiago de Chile (occasionally also ESAC, Madrid, Spain).

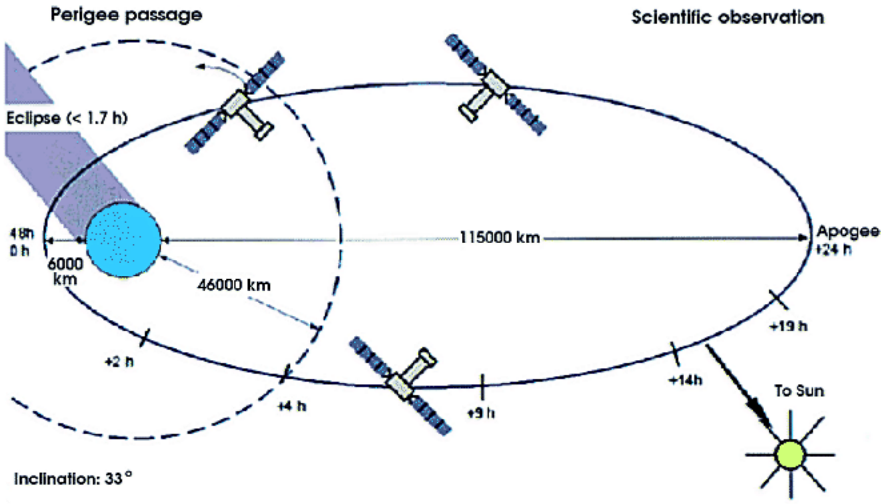

Figure 2.2. Sketch of the highly elliptical XMM-Newton orbit. Original figure provided by Dornier Satellitensysteme GmbH

Due to several perturbations, the orbit of XMM-Newton changes with time. In addition, an orbit correction manoeuvre was performed in February 2003 to ensure full ground station coverage during the entire science period. The orbital parameters for May 2009 (last update: May 2008) are listed in Table 2.1. Such an orbit provides the best visibility in the southern celestial sky.

Table 2.1. Orbital Parameters of XMM-Newton for March 2009

Inclination	58.8^o
Right ascension of ascending node	99.5^o
Argument of perigee	113.0^o
Apogee height	106,030 km
Eccentricity	0.58
Period	47.86 hours

2.2. Mirrors

2.2.1. Introduction

Each of the three X-ray telescopes on board XMM-Newton consists of 58 Wolter I grazing-incidence mirrors which are nested in a coaxial and cofocal configuration. The design of the optics was driven by the requirement of obtaining the highest possible effective area over a wide range of energies, with particular emphasis in the region around 7 keV. Thus, the mirror system had to utilize a very shallow grazing angle of $30'$ in order to provide sufficient reflectivity at high energies. The telescopes focal length is 7.5 meters and the diameter of the largest mirrors is 70 cm, to be compatible with the shroud of the launcher. Each telescope consists includes, apart from the mirror modules, baffles for visible and X-ray stray-light suppression and an electron deflector for diverting soft electrons. Two of the telescopes carry a Reflection Grating Array (RGA).

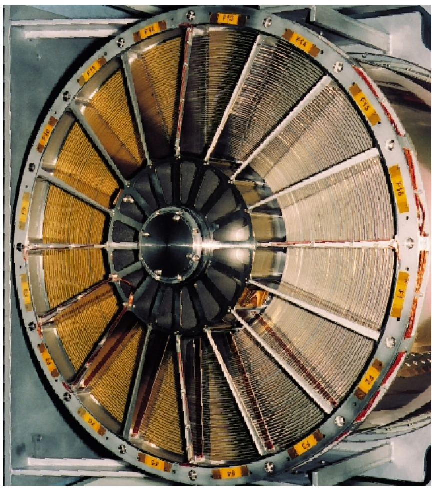

Figure 2.3. The XMM-Newton mirror modules on the backside of the XMM-Newton service module. One spider carrying a full set of 58 flight mirror shells is visible.Photo, ESA/XMM-Newton

2.2.2. Telescope Configuration

Each of the XMM-Newton telescopes consists of:

- The mirror assembly door, which protected the optics during integration, launch and early orbit phase,

- The entrance baffle, which provides visible straylight suppression at angles larger than 47°.

- The X-ray baffle.

- The Mirror Module.

- An electron deflector, which produces a circumferential magnetic field which prevents low energy electrons reflected by the mirrors reaching the focal plane detectors.

- In two of the telescopes, the Reflection Grating Array.

- The exit baffle, which provides an appropriate thermal environment.

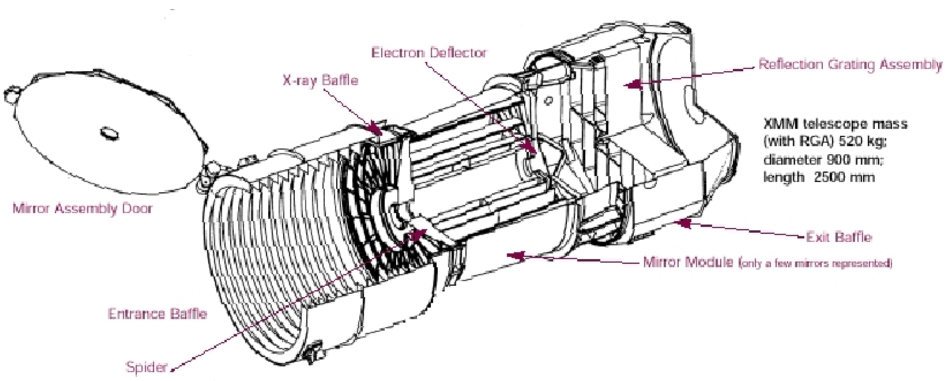

Figure 2.4. The 58 Wolter I mirrors of each telescope are bonded on their entrance aperture to the 16 spokes of a single spider made out of Inconel. Image courtesy ESA.

X-ray baffles are located in front of the mirror systems. They act as collimators and reduce considerably the amount of straylight in the field of view of the focal plane cameras. The spider (Figure 2.4) is connected to the support platform via an

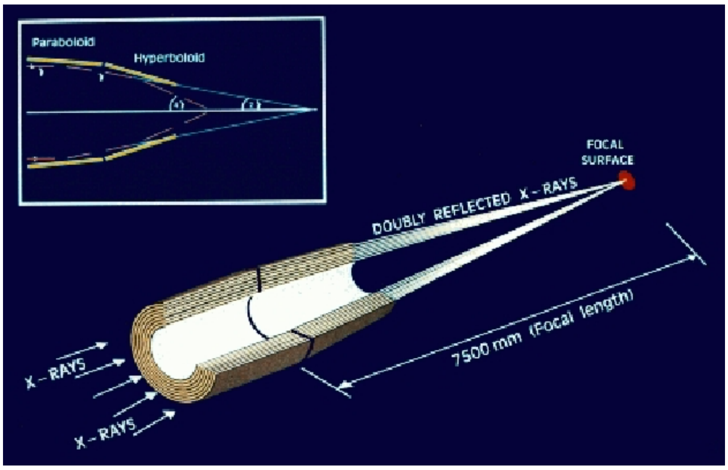

Figure 2.5. Light path in the XMM-Newton telescope with only an EPIC camera in its primary focus. Image courtesy ESA

aluminium interface structure (the MIS: Mirror Interface Structure) consisting of an outer cylinder and an interface ring. On two of the modules, the ring interfaces the mirror module to a Reflection Grating Assembly (RGA). To minimise the mechanical deformation of the mirrors and therefore the optical degradation, the flatness of the interface between the spider and the MIS had to be better than 5 micron.

The XMM-Newton X-ray baffle was constructed as two sieve-plates made out of circular strips. The plates were mounted coaxial to and coaligned with the front aperture cross section of the 58 mirror shells, such that they block single-reflection rays, but do not eclipse two-reflection rays. Each sieve plate is a disk 1 mm thick with 59 circular strips and 16 radial spokes. The offset of the two sieve plates from the front of the mirror system is 385 mm and 439 mm, respectively. All the baffle surfaces facing the mirrors are blackened.

The performance of the X-ray telescopes can be characterized by:

- Image Quality:

  The point spread functions and effective areas of the three telescopes were first characterized on-ground during an extensive calibration campaign. A comprehensive numerical model of the mirror system was used to generate an initial calibration database by extrapolating on-ground tests to in-orbit operation conditions and by interpolating between the finite number of measurement points.

On January 19 2000 the X-ray telescope FM2 saw "First Light", followed by FM3 and FM4. After "First Light" a number of observations were made during the commissioning phase in order to characterize the imaging performance of the telescopes. Analysis of the results indicated that the telescopes point responses measured in-orbit were basically the same as derived from on-ground calibration measurements out to $30''$. In particular, extended sources in the center of the telescope field of view can be studied with a $5''$ spatial resolution.

For on-axis sources, high energy photons are focused predominantly by the inner shells of the telescope. These inner shells apparently give better focus that the average hence the fractional encircled energy increases with increasing photon energy.

- Effective Area:

The design driver for the XMM-Newton telescopes was to achieve maximal area at low energies (2 keV) without sacrificing area at high energies (7 keV). XMM mirrors are most efficient in the energy range from 0.1 to 10 keV, with a maximum around 1.5 keV and a pronounced edge near 2 keV (the Au M edge). The design goal was to achieve a collecting area of 1900 cm^2 for energies up to 150 eV, 1500 cm^2 at 2 keV, 900 cm^2 at 7 keV, and 350 cm^2 at 10 keV, for each of the telescopes.

The effective area for each telescope was measured in the PANTER X-ray test facility illuminating the full aperture with line radiation between 0.28 and 10 keV, and using a copy of the ROSAT PSPC as focal plane detector.

- X-Ray Straylight Rejection:

  X-rays from outside the field of view can reach the sensitive area of the focal plane detectors by single reflection from the rear end of the hyperbola, if the source is at an off-axis angle between $20'$ and $80'$. Rays reflected just once from any one the parabolas cannot leave the mirror assembly because of the close packing of the mirror shells.

  The efficiency of the sieve plate system was ray traced and demonstrated to reduce the straylight level by a factor of 5 to 10 depending on the position in the focal plane. Pointings in the vicinity of the Crab Nebula confirmed the high efficiency of the baffles. The straylight collecting area of the EPIC detectors as a function of off-axis angle is about 3 cm^2 for sources located between $20'$ and $1.4°$ from the optical axis, and completely negligible at higher angles.

2.3. EPIC

2.3.1. Introduction

The XMM-Newton spacecraft is carrying a set of three X-ray CCD cameras, comprising the European Photon Imaging Camera (EPIC). Two of the cameras are MOS (Metal Oxide Semi-conductor) CCD arrays (referred to as the MOS cameras). They are installed behind the X-ray telescopes that are equipped with the gratings of the Reflection Grating Spectrometers (RGS). The gratings divert about half of the telescope incident flux towards the RGS detectors such that (taking structural obscuration into account) about 44 % of the original incoming flux reaches the MOS cameras. The third X-ray telescope has an unobstructed beam; the EPIC instrument at the focus of this telescope uses pn CCDs and is referred to as the pn camera.

The EPIC cameras offer the possibility to perform extremely sensitive imaging observations over the telescope's field of view (FOV) of 30 arcmin and in the energy

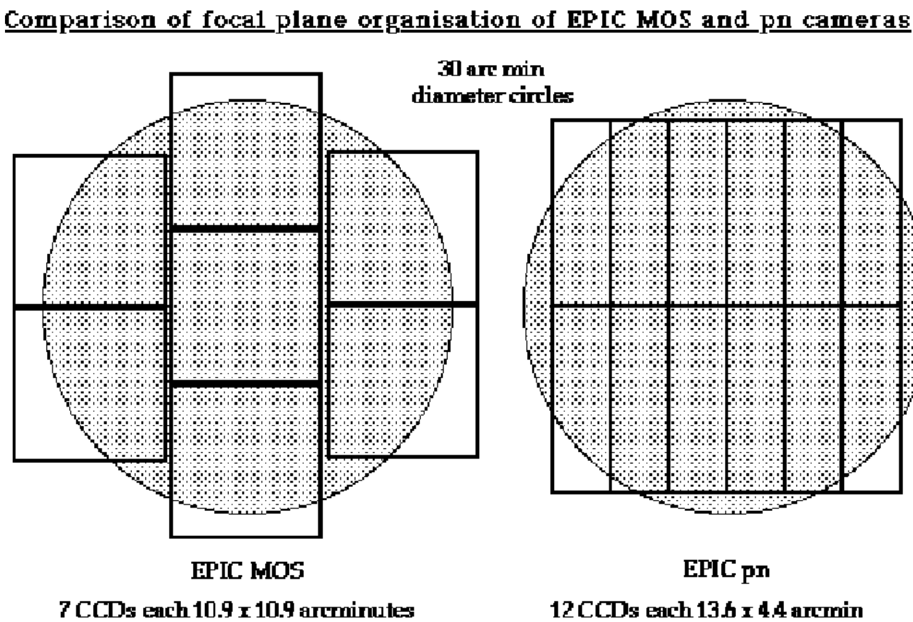

Figure 2.6. A rough sketch of the field of view of the two types of EPIC camera; MOS (left) and pn (right). The shaded circle depicts a diameter area. For the alignment of the different cameras with respect to each other in the XMM-Newton focal plane refer to the text

range from 0.15 to 15 keV with moderate spectral (E/Δ E $\sim$ 20-50) and angular resolution (PSF, 6 arcsec FWHM).

All EPIC CCDs operate in photon counting mode with a fixed, mode dependent frame read-out frequency, producing event lists, i.e. tables with one entry line per received event, listing (among others) attributes of the events such as the position at which they were registered, their arrival time and their energies. The two types of EPIC, however, differ in some major aspects. This does not only hold for the geometry of the CCD arrays and the instrument design but also for other properties, like e.g., their readout times.

Since 2005, scientific observations performed with MOS1 CCD6 switched of due to a micrometeoroid impact scattering debris into the focal plane.

Figure 2.7. Photography of the array of 7 CCDs of an EPIC MOS camera. Photo, ESA/XMM-Newton

2.3.2. MOS CCDs

The MOS EEV CCD22 (Figure 2.7) is a three-phase frame transfer device on high resistivity epitaxial silicon with an open-electrode structure; it has a useful quantum efficiency in the energy range 0.2 to 10 keV. The low energy response of the conventional front illuminated CCD is poor below 700 eV because of absorption in the electrode structure. For EPIC MOS, one of the three electrodes has been enlarged to occupy a greater fraction of each pixel, and holes have been etched through this enlarged electrode to the gate oxide. This gives an ”open” fraction of the total pixel area of 40 %; this region has a high transmission for very soft X-rays that would have otherwise be absorbed in the electrodes. In the etched areas, the surface potential is pinned to the substrate potential by means of ”pinning implant”. High energy efficiency is defined by the resistivity of the epitaxial silicon (around 400 Ohm-cm). The epitaxial layer is 80 microns thick (p-type). The actual mean depletion of the flight CCDs is between 35 to 40 microns: the open phase region is not fully depleted.

2.3.3. PN CCDs

The schematic view looking into the pn-CCD (Figure 2.8) introduces intuitively the advantages of the concept: X-rays hit the detector from the rear side. In the event

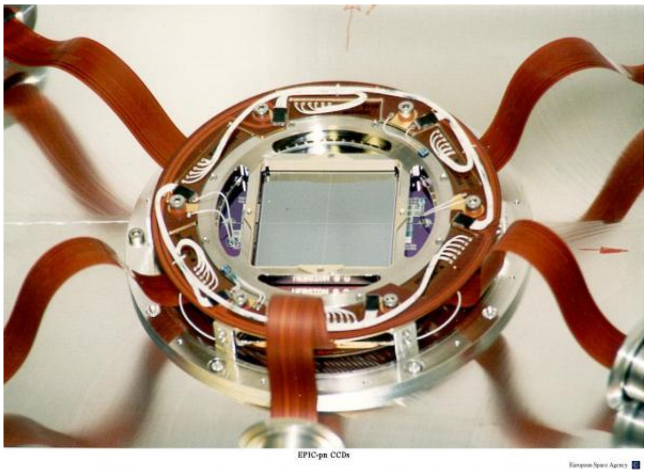

Figure 2.8. Photography of the 12 CCDs of the EPIC pn camera. Photo, ESA/XMM-Newton

of an X-ray interaction with the silicon atoms, electrons and holes are generated in numbers proportional to the energy of the incident photon. The average energy required to form an electron-hole pair is 3.7 eV at -90° C. The strong electric fields in the pn-CCD detector separate the electrons and holes before they recombine. Signal charges (in our case electrons), are drifted to the potential minimum and stored under the transfer registers. The positively charged holes move to the negatively biased back side, where they are 'absorbed'. The electrons, captured in the potential wells 10 microns below the surface can be transferred towards the readout nodes upon command, conserving the local charge distribution patterns from the ionization process. Each CCD line is terminated by a readout amplifier.

2.3.4. Operating Modes

The EPIC cameras allow several modes of data acquisition. Note that in the case of MOS the outer ring of 6 CCDs remain in standard full-frame imaging mode while the central MOS CCD can be operated separately. The pn camera CCDs can be operated in common modes in all quadrants for full frame, extended full frame and large window mode, or just with one single CCD (CCD0 in quadrant 1) for small window, timing and burst mode.

- "full frame" and "extended full frame" (pn only)

  In this mode, all pixels of all CCDs are read out and thus the full FOV is covered.

- "partial window"

  a) MOS

  In a partial window mode the central CCD of both MOS cameras can be operated in a different mode of science data acquisition, reading out only part of the CCD chip.

  b) pn

  In large window mode only half of the area in all 12 CCDs is read out, whereas in small window mode only a part of CCD number 4 is used to collect data.

- "timing"

  a) MOS + pn

  In the timing mode, imaging is made only in one dimension, along the column (RAWX) axis. Along the row direction (RAWY axis), data from a predefined area on one CCD chip are collapsed into a one-dimensional row to be read out at high speed. Since the 2 MOS cameras orientation differ by 90 degrees, the "imaging" directions in the 2 MOS are perpendicular to each other.

  b) pn only

  A special flavour of the timing mode of the EPIC pn camera is the "burst" mode, which offers very high time resolution, but has a very low duty cycle of 3%

2.3.5. Instrument Characteristics

One of the factors to be taken into account when determining the effective area of the EPIC cameras is their quantum efficiency. It is the quantum efficiency of the EPIC-MOS chips that limits the energy passband at its high energy end, while the pn camera can detect photons with high efficiency up to 15 keV.

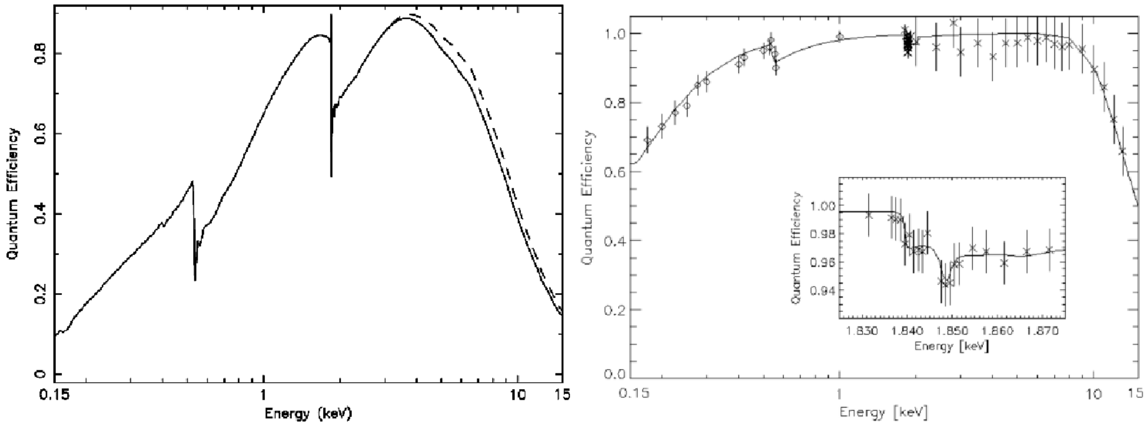

Figure 2.9. Quantum efficiency of the EPIC MOS1 (solid line) and MOS2 (dashed line) CCD1 chip as a function of photon energy. Quantum efficiency of the EPIC pn CCD chips as a function of photon energy (Struder et al., 2001)

2.3.6. Filters and Effective Area

As the EPIC detectors are not only sensitive to X-ray photons but also to IR, visible and UV light, the cameras include aluminised optical blocking filters to reduce the contamination of the X-ray signal by those photons.

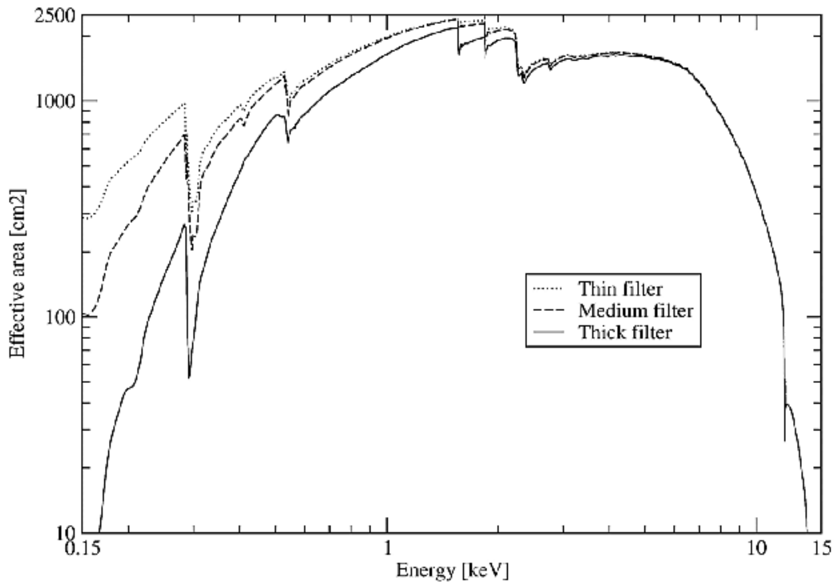

Figure 2.10. Combined effective area of all telescopes assuming that all cameras operate with the same filters, either open, thin, medium or thick

If such photons are registered by the EPIC detectors, the data analysis would be impeded in three ways:

- Shot noise on the optically generated photo-electrons will increase the overall system noise
- The energy scale will be incorrectly registered, because a nominally zero signal will have a finite offset. For each optically generated photo electron, the energy scale shifts by about 3.6 eV.
- Optically-generated photo electrons can lead to a saturation of electron traps, changing (improving) the charge transfer inefficiency.

There are four filters in each EPIC camera. Two are thin filters made of 1600 $\mathring{A}$ of poly-imide film with 400 $\mathring{A}$ of aluminium evaporated on to one side; one is the medium filter made of the same material but with 800 $\mathring{A}$ of aluminium deposited on it; and one is the thick filter. This is made of 3300 $\mathring{A}$ thick Polypropylene with 1100 $\mathring{A}$ of aluminium and 450 $\mathring{A}$ of tin evaporated on the film. The filters are self-supporting and 76 mm in diameter. The remaining two positions on the filter wheel are occupied by the closed (1.05 mm of aluminium) and open positions, respectively. The former is used to protect the CCDs from soft protons in orbit, while the open position could in principle be used for observations where the light flux is very low, and no filter is needed.

2.4. RGS

Behind two of the three X-ray telescopes, about half of the X-ray light is utilized by the Reflection Grating Spectrometers (RGS). Each RGS consists of an array of reflection gratings which diffracts the X-rays to an array of dedicated charge coupled devices (CCD) detectors. The RGS instruments achieve high resolving power (150 to 800) over a range from 5 to 35 $\AA$ [0.33 to 2.5 keV] (in the first spectral order). The effective area peaks around 15 $\AA$ [0.83 keV] (first order) at about 150 cm^2 for the two spectrometers.

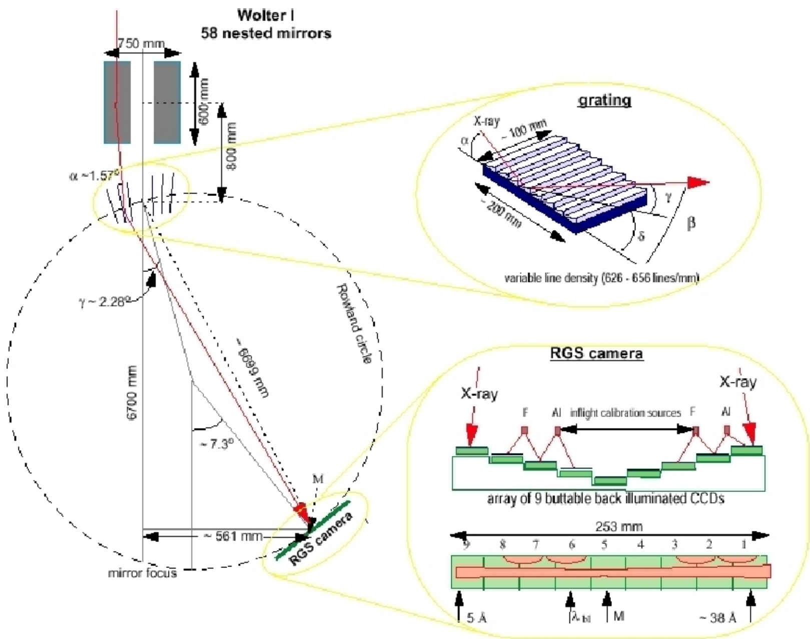

Figure 2.11. Schematic layout of the RGS (from Brinkman et al. 1998)

2.5. OM

The Optical/UV Monitor Telescope (XMM-OM) is mounted on the mirror support platform of XMM-Newton alongside the X-ray mirror modules. It provides coverage between 170 nm and 650 nm of the central 17 arc minute square region of the X-ray field of view, permitting routine multiwavelength observations of XMM targets simultaneously in the X-ray and ultraviolet/optical bands.

The XMM-OM consists of a Telescope Module and a separate Digital Electronics Module, of which there are two identical units for redundancy. The Telescope Module contains the telescope optics and detectors, the detector processing electronics and power supply. There are two distinct detector chains, again for redundancy. The Digital Electronics Module houses the Instrument Control Unit, which handles communications with the spacecraft and commanding of the instrument, and the Data Processing Unit, which pre-processes the data from the instrument before it is telemetered to the ground.

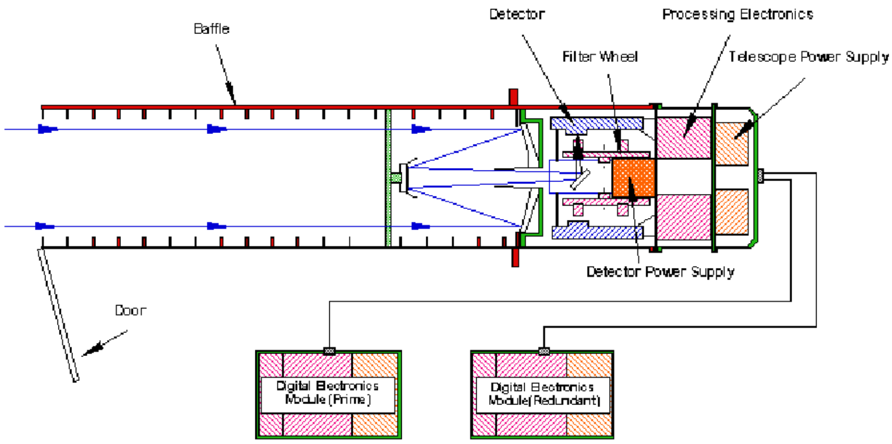

Figure 2.12. The components of Optical Monitor. Image courtesy ESA

3. DATA ANALYSIS

Data analysis in high energy astrophysics is a demanding proccess once you get the data from the satellite. Observational astrophysics requires knowledge of technology, computer science and a whole background of physics and surely statistics since technology has recently progressed a lot and an enourmous amount of information of high quality has been obtained.

The aim of astrophysical data analysis is to examine data coming from the satellites and produce scientifically meaningful results like spectra, images and light-curves which are the tools we use to understand the physics of the object in interest.

The aim of this thesis is to see the temperature distribution of the ICM between the sub-structures of the sample clusters of galaxies via spectral analysis.

3.1. Data Reduction

Observation Data Files of (ODFs) MOS cameras are processed by SAS 7.0.0 and those of PN's by SAS 7.1.0. We profited from SAS ABC-Guide (from NASA XMM-GOF) [45] and SAS Analysis Threads [46] for the data reduction. The event lists are generated by the tasks EPPROC for PN and EMCHAIN for MOS. The reason I used EMCHAIN instead of EMPROC for MOS is because I used XMM Extended Analysis Software (XMM ESAS) for the data reduction of the MOS cameras. XMM ESAS has its own scripts where EMCHAIN is used to create calibrated event lists from ODFs. All product (spectra, images, light curves) creations, only those of PN cameras, are mainly done by EVSELECT and XMMSELECT Graphical User Interface (GUI) [47] tasks, high background cleaning is done by creating Good Time Intervals (GTI) by TABGTIGEN and Ancillary Response Files (ARF) are created with the call for extended sources and a detector map is used. For PN data a threshold on the light curve counts is determined, defining low background intervals, then a corresponding GTI file created and used to filter the event list.

Table 3.1. Observation log of the EPIC cameras

Sources	**Date**	**Filter**	**Mode**			**Exposure (ks)**		
			MOS1	MOS2	PN	MOS1	MOS2	PN
Abell 3705	06.10.2004	medium	prime full window	prime full window	prime full window	24370	24375	20248
Abell 2440	18.11.2006	medium	prime full window	prime full window	prime full window extended	46428	46423	42540
Abell 2933	19.11.2005	medium	prime full window	prime full window	prime full window extended	31569	31574	27642
Abell 3888	02.05.2006	thin	prime full window	prime full window	prime full window extended	21213	21213	17041
Abell 115	16.07.2004	medium	prime full window	prime full window	prime full window extended	44070	44075	40680

For each cluster, spectral analysis is done for four regions (except Abell 3705, five regions are analysed). These regions are: binary parts (regions A and B), region between (region C) these binary poles and a bigger region (region D) covering these three regions. Only for Abell 3705 another region is added because of a faint elongation is seen from one of subclumps. Spectral analysis is done by Xspec v12 [48] and a thermal plasma model, Astrophysical Plasma Emission Code (APEC) [49], is used to fit all the data. In the spectral fitting *reduced* χ^2 and *Cash's statistics (C statistics)* [50] are used. When the null hypothesis probability was under 0.05 C-statistics is used and the spectrum is not grouped. C-statisitcs is used when the counts/bin become of the order of 1. In chi squared statistcs reduced chi square gives in general an idea to compare the goodness of fit mathematically with the model, however in C-statistics case there is no such a criteria, instead one has to make F-test, or for a good fit, *goodness* command in Xspec has to give a value around 50% for realizations which are smaller than best fit C- statistic of that data set. But in any case one has to make F- test. In this thesis, F-test are not made because of the limited time, only *goodness* values are taken care. The way to use C-statistic is to use the data spectrum without subtructing the background and without grouping (because when the data is grouped one looses data) and then to simultaneously fit to both the source and background files [51]. But it requires to know the background model and it means a lot of paremeters. In the XMM-ESAS cookbook [52] there is an example with 12 parameters. When there are significant instrumental lines in the spectrum one can add Gaussian lines to the spectral model or cut the problematic energy band (instrumental lines). In the first case, number of paremeters increases and sometimes it can causes diffucilties while fitting the model to the spectrum. In the latter case data is lost. In this thesis problematic energy ranges are taken off.

3.2. Background Analysis

Background analysis of the extended sources like clusters of galaxies is not an easy task since the source covers most of the camera's field of view and there is a high EPIC background, which will be mentioned in *EPIC* subsection in detail. Besides we do not know exactly where is the cluster's limit. Contributions of both instrumental background and Cosmic X-Ray Background (CXB) to the resultant spectrum are modelled however there could be a lot of parameters to take into account therefore, spectral analysis becomes complicated.

In order to extract a background for the spectral analysis one has mainly two alternatives; either one can use *blank sky event lists*, which are basicaly superpositions of pointed observations, provided by XMM- Newton or choose a background region from the same observation of the sample's. Both of these methods have their own advantages and disadvantages.

In this thesis I did not use the blank sky files because the amount of residual soft proton contamination, CXB and solar wind charge exchange contamination which is included in these observations are not clear,[2] instead I specified a region from the same observation for PN cameras and for MOS cameras used XMM ESAS which extracts the background from the same observation with more sophisticated methods.

If one picks a background region from the same observation, normally one has to

[2]Recently XMM-Newton Background Team offers an EPIC blank sky product request form where one can specify instrument specifications and other options like revolution, coordinates etc.

choose it in the same chip with the source because within the same EPIC camera every chip have diffrent instrumental background level. However since an extended source covers more than one chip one has to choose the background region from another chip. In this case one should take into account that both the extracted source and background spectra come from chips with different systematics and it means that one assumes the source region has the same background spectrum as the background region.

3.2.1. The X-Ray Background

One can divide the X-ray background in two; extragalactic X-ray background, CXB, and galactic X-ray background (GXB). The CXB emission is first discovered in 1962 from an observation intended to detect X-rays from the Moon. From then a lot of observations done by several X-ray missions in order to reveal the nature of this emission. CXB has an uniform distribution with small deviations from isotropy on a variety of angular scales. Its spectrum is similar to that which would be produced by ionized gas at nearly 40 keV and on large angular scales it appears quite diffuse. There are two theories concerning the origin of this emission, one is a thermal plasma hypothesis and the other one is discrete source hypothesis. Today, after the deep field observations of ROSAT, XMM-Newton and Chandra, it is accepted that the CXB is originated from discrete sources, mostly from unresolved AGN population, while the nature of the later needs still to be studied [53]. Galactic X-ray background is seen below 1 keV and thermal emission from hot gas is the likely source of this background flux. The emission below 0.3 keV is dominated by hot gas in a low density region within referred to as the Local Bubble, while the emission between 0.3 and 1.0 keV is of more uncertain origin.

3.2.2. EPIC Background

The EPIC background is briefly composed of instrumental background, like electronic noise etc., and non-instrumental background, like the astrophysical background. A very detailed table summarizing the EPIC background components and further information can be found in the *Calibration & Backgroun Treatment* page of the XMM-

Newton website. Here, a summary provided from XMM-Newton Background website and EPIC Background Files are presented [54].

Astrophysical background means GXB which is dominated by the thermal emission below 1 keV and CXB which is dominated by power low at higher energies. We can add solar wind charge exchange into the astrophysical background category as the photon component.

Noise component of the instrumental background becomes important below 200 eV. Another component is due to the interaction of particles with the structure surrounding the detectors and the detectors themselves become important at higher enrgies, above a few keV and has a flat spectrum. The most significant instrumental backgrounds are Al K α and Si K α emission lines of MOS cameras which are at $\sim$ 1.49 keV and $\sim$ 1.75 keV, respectively.

The particle induced background is composed of two components. One is an external flaring component which is due to soft protons (E$<$100 eV), probably accelerated by magnetospheric reconnection events and unrelated to the solar flares. Flares of higher count rates are usualy characterised with fast rise and fall times in the X-ray light curve. Figure 3.1 and 3.2 display examples of X-ray light curves showing flare effects and in which flares are removed respectively. The second one is the charged particles passing through the camera and responsible from the generation of fluorescent X-ray emission. For example we see these emissions as emission lines of aluminium and silicium in MOS which are characteristics of the camera body.

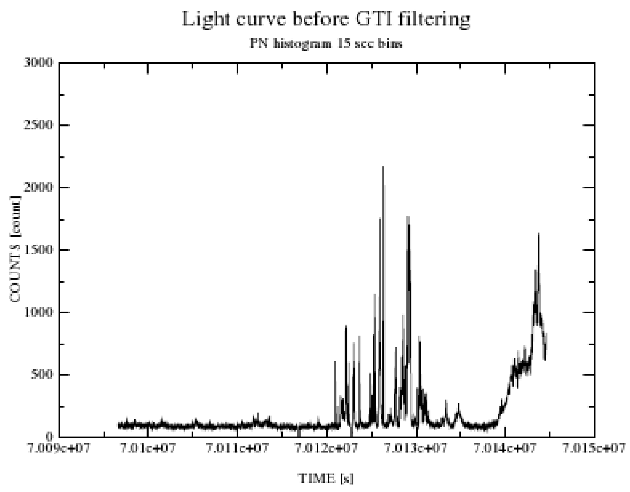

Figure 3.1. Example of a light curve effected by proton flares,Lumb, D.

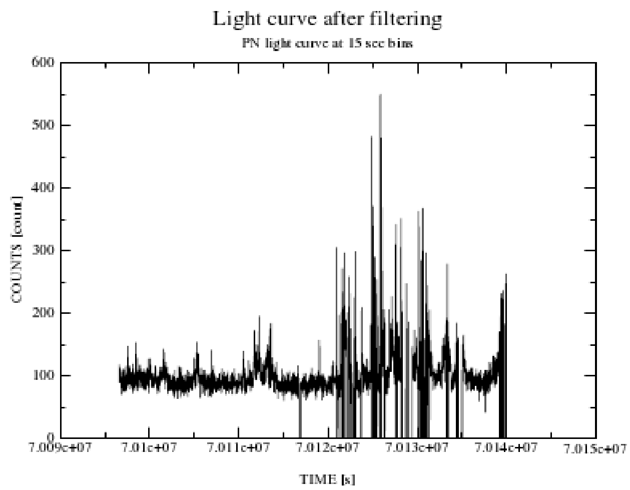

Figure 3.2. Example of a light curve with removed proton flares,Lumb, D.

3.3. Extended Sources Analysis Software

The Extended Source Analysis Software package (XMM-ESAS) [52] was developed at the NASA/GSFC XMM-Newton Guest Observer Facility (GOF) in cooperation with the XMM-Newton SOC and the Background Working Group. The XMM-ESAS package currently consists of both PERL scripts and stand-alone Fortran 77 programs. The output files are FITS standard and can be used in spectral fitting packages (e.g., Xspec) or with FITS image display software (e.g., fv or ds9). XMM-ESAS is based on the software used for the background modeling described in [55]. XMM-ESAS allows the user to model the quiescent particle background both spectrally and spatially for the EPIC MOS detectors. It will produce background spectra for user-defined regions of the detectors and background images. In this work, all the MOS1 and MOS2 spectra and mosaic images are extracted by using XMM-ESAS. Mosaic images shown in the *Results* chapter are background subtracted and exposure corrected images with and without point sources and all of them are created by *adapt-900* program which is an adaptive filtering routine used to create smoothed background subtracted and exposure corrected images for individual observations.

3.4. Wavelet Algorithm Package

The X-ray Wavelet Spectral Mapping (XWSM) package [56] is a set of tools dedicated to the mapping of spectroscopic parameters associated with the X-ray emission of the Inter Galactic Medium (IGM), within clusters and groups of galaxies. Spectroscopic parameters like the IGM brightness, temperature and metallicity can be estimated within specific regions of the field of view, or mapped by means of wavelet algorithms. The version of XWSM used in this thesis is specific to XMM data. XWSM used APEC model to fit spectra and do not add any additional Gaussian lines or cut some energy ranges which are dominated by instrumental background. All the temperature and metallicity maps shown in the *Results* chapter are created by using the observations from all three cameras, MOS1, MOS2 and PN, respectivley and between 0.30-10.00 keV energy ranges.

4. PREVIOUS OBSERVATIONS

Optical observations show that:

- Abell 3705 is an *irregular* cluster [57] with a bright cD galaxy and with Bautz-Morgan type III lies in a region of high stellar density with z= 0.0895 [58]. *Richness class* is 3, number of member galaxies within 1.5 h_{100}^{-1} Mpc from the cluster center is 40 and the robust velocity dispersion is $\sigma_{rob} = 958^{+94}_{-76}$ km/s [59]. According to Zabludoff et al. 2009 [60] and the references therein Abell 3705 shows no clear optical evidence of an ongoing major merger and z=0.0906.

- Abell 2440 is an *intermediate* galaxy cluster of *richness class 0* [7],[61] with Bautz-Morgan type II [59]. Redshift is measured, z=0.0904. Observations show that galaxy distribution has three main components, each associated with a giant elliptical galaxy [61].

- Abell 2933 is a *regular-intermediate* (RI) type cluster in the Abell system of cluster classification and its Bautz-Morgan type is *III* with a cD [62], [63]. Optical analysis shows bimodal substractures as a consequence of large cluster position angle, θ_o = 137.6, θ_x = 146.2, ellipticity, ε_o = 0.43, ε_x = 0.55 and significant center of mass shift, $sc_o = 0.20$, $sc_x = 0.23$ [62].

- Abell 3888 is a galaxy cluster with Bautz-Morgan type *I-II*, *richness class 2* and is a centarally condensed cluster dominated by bright ellipticals [64]. It is shown that there are three distinct subclumps of multiple galaxies in the core regions and the projected spatial distribution of galaxies in Abell 3888 is found elongated with an ellipticity $\varepsilon_o = 0.43$ [65].

- Abell 115 studies go back to 1958 (George Abell [7]). In this work, Abell 115 was one of the catalogued clusters and displayed with its coordinates. From 1958 to present date a lot of works are done for Abell 115. Most of these works deal with the strong radio galaxy 3C28.0 in the northern region. The radio morphology is intermediate between the classical Fanaroff-Riley I and II classes. A double sided radio jets through the northern pole is seen [66], [67], [68]. Abell 115 is a *richness class 3* galaxy cluster with Bautz-Morgan type III lies in a region of high stellar density after the optical observations [69],[70].

X- ray observations show that:

- Abell 3705 is defined as a cluster with super cluster richness class $\sim$ 10 and at a distance of 255 h^{-1} Mpc [71]. Its temperature is defined $kT_{peak} = 3.71^{+0.22}_{-022}$ keV after an XMM- Newton X-ray analysis done by using only MOS cameras and XMM-ESAS package with (0.5-10) keV region of the spectrum being fitted with background model parameters in addition to the APEC model [60].

- Abell 2440 is shown having double peaked X-ray morphology in Einstein IPC between (0.3-3.5) keV [61]. Angularly unresolved temperature is measured with Einstein MPC data is kT=9 keV (1σ >4.4 keV) [72]. Three giant ellipticals with small projected seperation from the bright X-ray core are observed and both X-ray emitting gas and the galaxy distribution define three significant peaks which are ceneterd with a giant elliptical [61]. Abell 2440 is possibly seen before the collision of the three subclusters as the gas distribution indicates [73]. The X-ray emission asymmetry which extends to the south-east between two elliptical's groups (regions A and B in this thesis) strongly suggests that there are ongoing gas interactions between them [61].

- Abell 2933 is seen with binary substructure morphology in X- ray observations [57], [62], [63]. It is a merger at the beginning of the interaction with a large impact parameter [74].

- Abell 3888 is not a relaxed cluster, its X-ray isophote are not circular and surface brightness obtained from XMM-Newton observations show an elongated, single-peaked distribution if the ICM [75]. There is a Seyfert 1 galaxy detected within

2 arcmin from the center therefore, an AGN contamination is possible, an XMM-Newton observation shows that the AGN contribution is about 10% of the total emission in the (0.5-2.0) keV [76] (and references therein). Temeperature and metal abundance measurements are 10.38 keV and 0.323 Z_o [77].

- Abell 115 shows a binary morphology in all X-ray observations. ASCA [78] temperature and metal abundance measurements for regions A, B and C are: 1)for 2 arc min; $kT = 4.85^{+0.45}_{-0.40}$ keV and $(0.21^{+0.08}_{-0.08})$ Z_o, $kT = 5.08^{+0.71}_{-0.61}$ keV and $(0.21^{+0.10}_{-0.10})$ Z_o, $kT = 6.25^{+0.93}_{-0.43}$ keV and $(0.21^{+0.12}_{-0.12})$ Z_o 2)for 3 arc min; $kT = 5.37^{+0.42}_{-0.39}$ keV and $(0.15^{+0.07}_{-0.07})$ Z_o, $kT = 5.52^{+0.62}_{-0.52}$ keV and $(0.13^{+0.07}_{-0.06})$ Z_o, $kT = 5.74^{+0.54}_{-0.42}$ keV and $(0.21^{+0.09}_{-0.09})$ Z_o, respectively. Spectra ranges are (0.7-10) keV for SIS and (0.8-10) keV GIS and spectral model used is Raymond & Smith with power law. Chandra observations [67] for northern subcluster and its core are: $kT = 3.43^{+0.09}_{0.09}$ keV, $kT = 2.19^{+0.08}_{0.08}$ keV and $(0.37^{+0.03}_{-0.03})$ Z_o, $(0.44^{+0.03}_{-0.03})$ Z_o, for southern subcluster are: $kT = 5.35^{+0.47}_{-0.46}$ keV, $(0.19^{+0.09}_{-0.08})$ Z_o and for connection region is $kT = 7.19^{+0.53}_{-0.46}$ keV, $(0.22^{+0.06}_{-0.06})$ Z_o. Spectral analysis is done between (0.5-6) keV with Raymond & Smith model [68]. X- ray observations indicate a merging effect.

5. RESULTS

In this chapter, the spectral analysis results of each cluster are shown separately in tables, maps, spectral fittings, images and graphs. First raw images of PN (in sky coordinates) and MOS (in detector coordinates) cameras with spectral and background regions are shown in each subsection. Four regions, A, B, C and D, are chosen for spectral analysis for each cluster except Abell 3705 (Abell 3705 has five regions). The optical images with X-ray contours and X-ray images with radio contours (only for Abell 115) are displayed. Background subtracted and exposure corrected images created by XMM-ESAS are displayed. Images with point sources are shown with a logarithmic scale while those without point sources are displayed with a square root scaling. Spectral results and their standart deviations are given in tables. Temperature and metallicity maps created by XWSM are shown. For each cluster observed and the model partical bakground spectra and radial profiles (of surface brighteness) of MOS1 and MOS2 from the full field of view are also displayed. The smooth part of the curves at $\sim$ 1.5 keV in the model partical background is the "bridge" where the Al K α and Si K α fluorescent instrumental lines affect the data [54]. Temporal fitting results of the two MOS cameras are shown for all cluster samples. In these figures, upper panel shows the light curve histogram for (2.5-12.5) keV band from the FOV. Red vertical lines on the Gaussian curve show the selection limits, blue vertical lines show the range for the Gaussian fit and the green curve is the Gaussian fit. In the bottom two panels green points indicate accepted data while black points indicate data excluded by the filtering algorithm of the XMM-ESAS. The middle panels displays the (2.5-12.5) keV band FOV light curve and the lower panel displays (2.5-12.5) keV band light curve from the unexposed corners of the instrument. Then PN's observations light curves and spectra of spectral regions with their backgrounds are shown. Lastly model fitted spectra of MOS and PN cameras are displayed.

5.1. Abell 3705

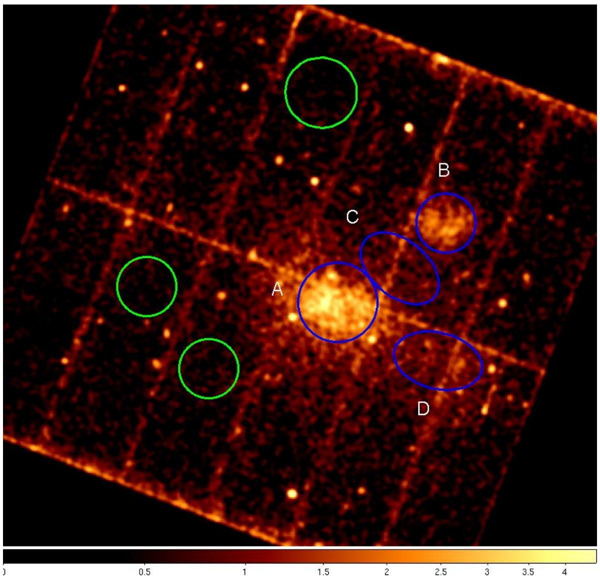

Figure 5.1. Abell 3705, raw image, regions chosen for spectral analysis on PN camera

On the cameras, regions A and B (Figures 4.1 and 4.2) cover 2 and 1,5 arc minutes, respectively.

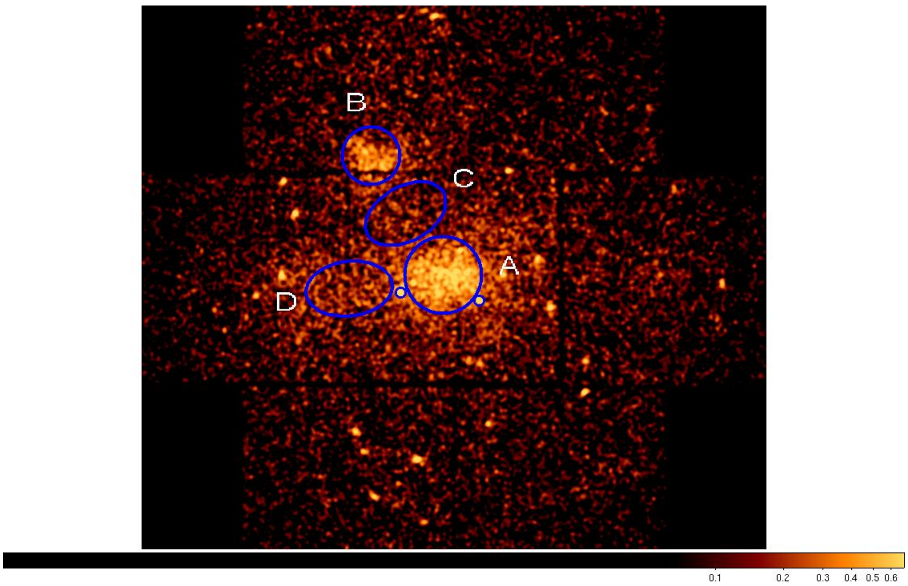

Figure 5.2. Abell 3705, raw image, regions chosen for spectral analysis on MOS2 camera

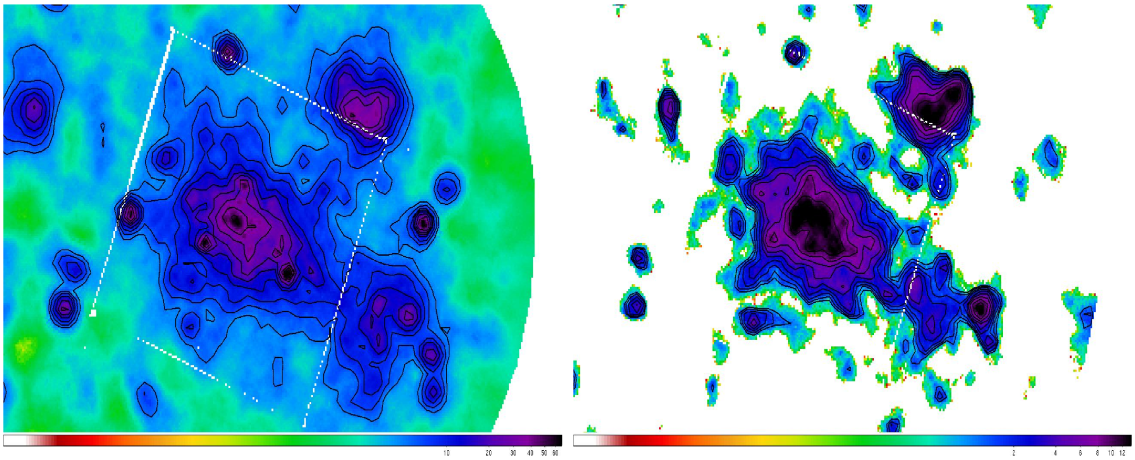

Figure 5.3. Abell 3705, background subtracted and exposure corrected image of MOS cameras in the (0.35-1.25) keV (leftt) and (2-8) keV (righ)

In soft band (Figure 4.3), connection between the regions A and D is present, also elongation between regions A and B is seen. In hard band connection between the regions A and B is not clear as in that of soft band however connection with the region D is still present.

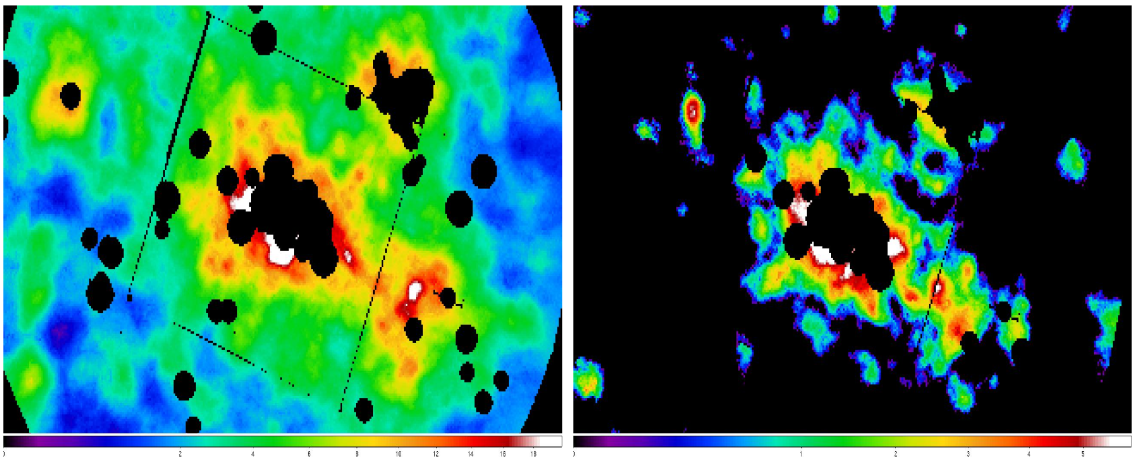

Figure 5.4. Abell 3705, background subtracted and exposure corrected image of MOS cameras with point sources are removed in the (0.35-1.25) keV (left) and (2-8) keV (right)

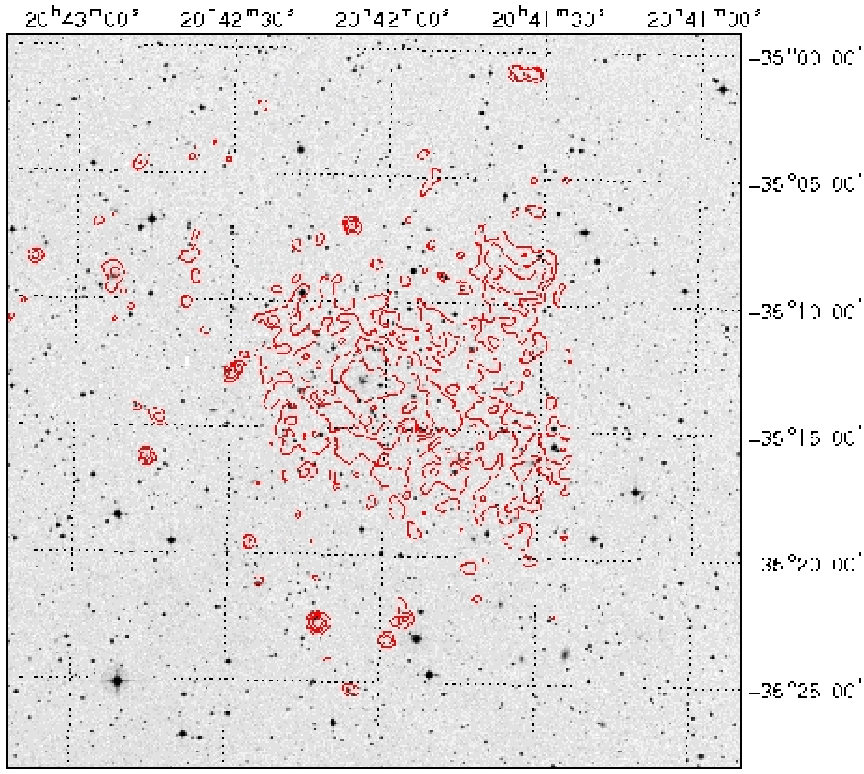

Figure 5.5. Abell 3705, X-ray contours over optical image

For each region spectra of the two MOS cameras are fitted simultaneously. Spectral results are displayed in Table 4.5 as follows: For both MOS cameras, spectral fitting of the region A is done by using chi statistics. Spectra from MOS1, MOS2 and PN are grouped in 25. The spectral data counts of these spectra are 2179, 2285 and 3679, respectively. Reduced chi-squared are 1.0179 for 133 degrees of freedom, 0.96397 for 124 degrees of freedom and the null hypothesis probabilities are 4.260930e-01 and 5.966700e-01, respectively. Difference between weihgted mean value of the temperature and temperature from MOS1 is 1.21 σ, from MOS2 is 0.53 σ and from PN is 1.32 σ. Difference between weihgted mean value of the metal abundance and metal abundance from MOS1 is 0.8 σ, from MOS2 is 0.6 σ and from PN is 2.25 σ.

For both MOS cameras and PN camera spectral fitting of the region B are done by using C statistics because data counts are not enough to use chi statistics so null hypothesis probabilities are always below 0.05 even instrumental lines are removed.

Spectrum from three cameras are not grouped. The spectral data counts are 467, 491 and 1020 respectively. For MOS and PN cameras, C-statistics are 505.40 for 840 degrees of freedom, 879.04 for 1441 degrees of freedom and goodness values are 86.00 % of realizations are smaller than best fit statistic 505.40 and 100.00 % of realizations are smaller than best fit statistic 879.04, respectively. Difference between weihgted mean value of the temperature and temperature from MOS1 is 1.5 σ, from MOS2 is 4.6 σ and from PN is 0.83 σ.

For both MOS cameras and PN camera spectral fitting of the region C are done by using chi statistics. Spectrum from MOS1, MOS2 and PN are grouped in 15 and in 35, respectively. The spectral data counts are 448, 372, and 638 respectively. These counts are also very low like those of region B but chi statistics gives higher values for null hypothesis probabilities while goodness values are always 100%. For MOS and PN cameras, reduced chi-squared are 1.203 for 46 degrees of freedom, 1.276 for 15 degrees of freedom and the null hypothesis probabilities are 1.623725e-01 and 2.073378e-01, respectively. Difference between weihgted mean value of the temperature and temperature from MOS1 is 2 σ, from MOS2 is 2 σ and from PN is 0.08 σ.

For both MOS cameras and PN camera spectral fitting of the region D are done by using chi statistics. Spectrum from MOS1, MOS2 and PN are grouped in 15. The spectral data counts are 622, 669, and 1069 respectively. For MOS and PN cameras, reduced chi-squared are 1.005 for 69 degrees of freedom, 0.9924 for 63 degrees of freedom and the null hypothesis probabilities are 4.657542e-01 and 4.932889e-01, respectively. Difference between weihgted mean value of the temperature and temperature from MOS1 is 0.45 σ, from MOS2 is 0.45 σ and from PN is 0.43 σ. Difference between weihgted mean value of the metal abundance and metal abundance from MOS1 is 1 σ and from MOS2 is 0.43 σ.

For both MOS cameras and PN camera spectral fitting of the region E are done by using chi statistics. Spectrum from MOS1, MOS2 and PN are grouped in 45 and in 65, respectively. The spectral data counts are 5853, 6152, and 9148 respectively. For MOS and PN cameras, reduced chi-squared are 1.1475 for 202 degrees of freedom, 1.0821 for 123 degrees of freedom and the null hypothesis probabilities are 7.385981e-02 and 2.515732e-01, respectively. Difference between weihgted mean value of the temperature and temperature from MOS1 is 0.6 σ, from MOS2 is 0.7 σ and from PN is 2.7 σ. Difference between weihgted mean value of the metal abundance and metal abundance from MOS1 is 2 σ, from MOS2 is 1.16 σ and from PN is 0.6 σ.

Large deviations in σ values are due to 1) different background subtraction methods are used, 2) poor statistics.

Table 5.1. Abell 3705, spectral results of temperature and metal abundances for each regions and their errors

Regions	MOS1		MOS2		PN	
	temperature (keV) & c.r.	metal abundance (Z_o) & c.r.	temperature (keV) & c.r.	metal abundance (Z_o) & c.r	temperature (keV) & c.r.	metal abundance (Z_o) & c.r
A	3.12 -0.33/+0.36	0.06 -0.06/+0.17	2.99 -0.31/+0.33	0.13 -0.13/+0.16	2.64 -0.23/+0.31	0.28 -0.12/+0.15
B	1.32 -0.32/+0.36	0 +0.03	1.7 -0.40/+0.34	0.14 -0.14/+0.22	1.04 -0.14/+0.06	0 0
C	2.5 -0.63/+0.80	0 +0.23	2.5 -0.79/+1.17	0.11 -0.11/+0.40	1.35 -0.06/+0.47	0 0
D	2.48 -0.60/+0.88	0.3 -0.24/+0.62	2.9 -0.68/+0.68	0.60 -0.43/+0.72	2.49 -0.63/+1.00	0 +0.22
E	3.26 -0.26/+0.32	0.23 -0.12/+0.15	3.28 -0.25/+0.31	0.18 -0.11/+0.13	2.6 -0.31/+0.45	0.07 -0.07/+0.12

Table 5.2. Abell 3705, weighted means and standart deviations of spectral results

Regions	weighted mean		standart deviation (σ)	
	temperature (keV)	metal abundance (Z_o)	temperature (keV)	metal abundance (Z_o)
A	2.89	0.10	0.19	0.05
B	1.14	0	0.12	0
C	1.74	0	0.38	0
D	2.69	0.51	0.47	0.21
E	3.14	0.11	0.20	0.06

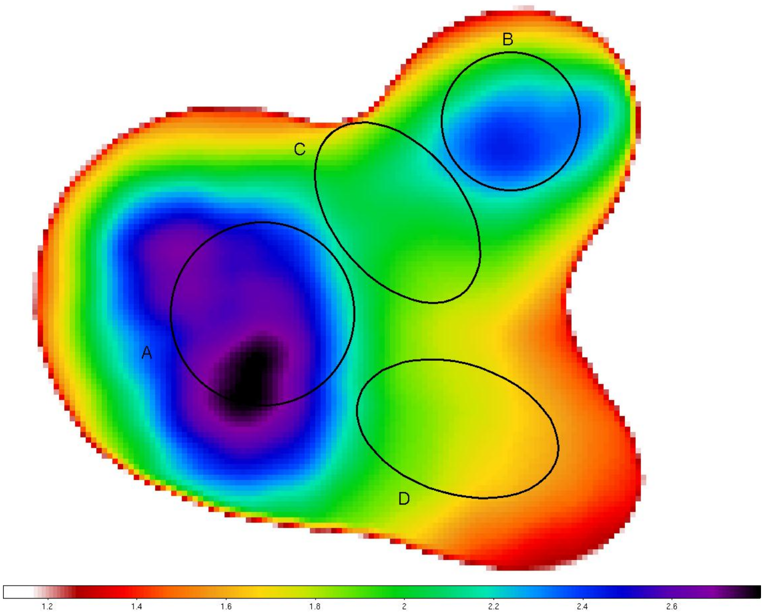

Figure 5.6. Abell 3705, temperature map extracted with XWSM. The color diagram is between 1.2-2.6 keV

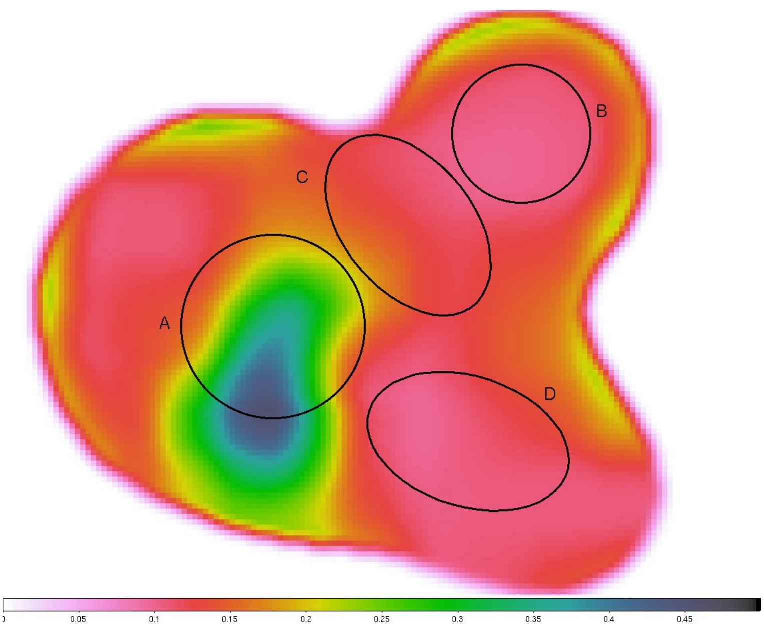

Figure 5.7. Abell 3705, metalicity map extracted with XWSM. The color diagram is between 0.05-0.45 Z_o

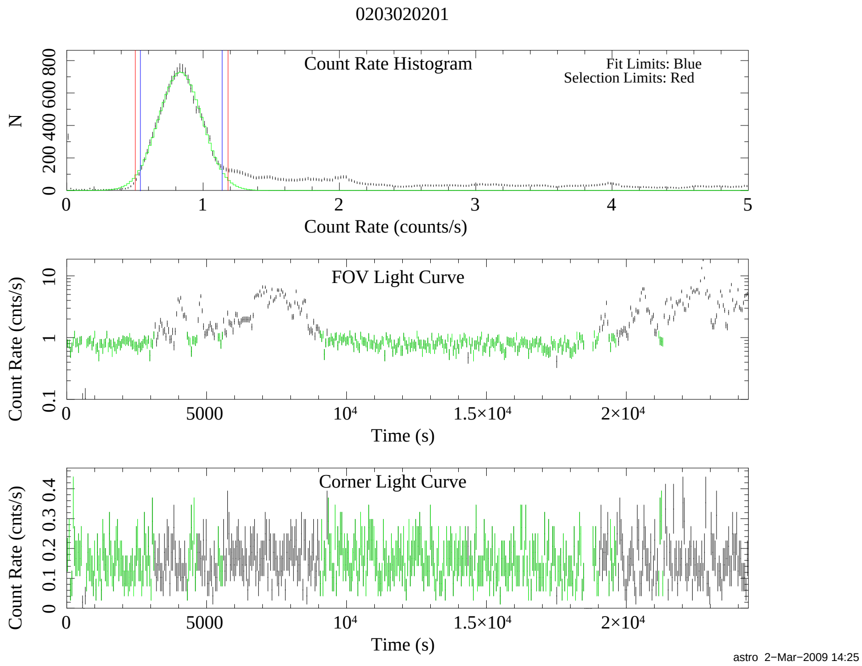

Figure 5.8. Abell 3705, temporal filtering results for the MOS1 observation

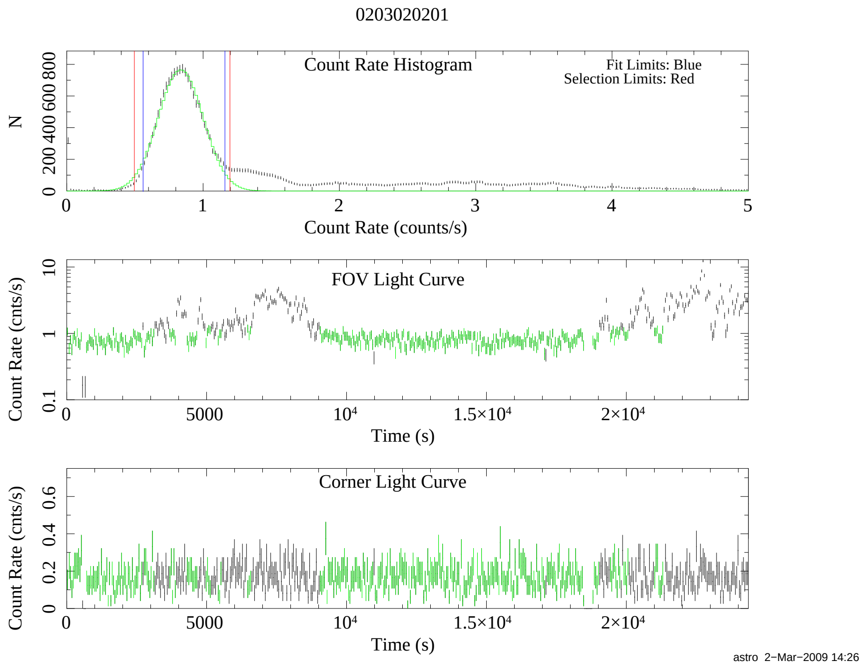

Figure 5.9. Abell 3705, temporal filtering results for the MOS2 observation

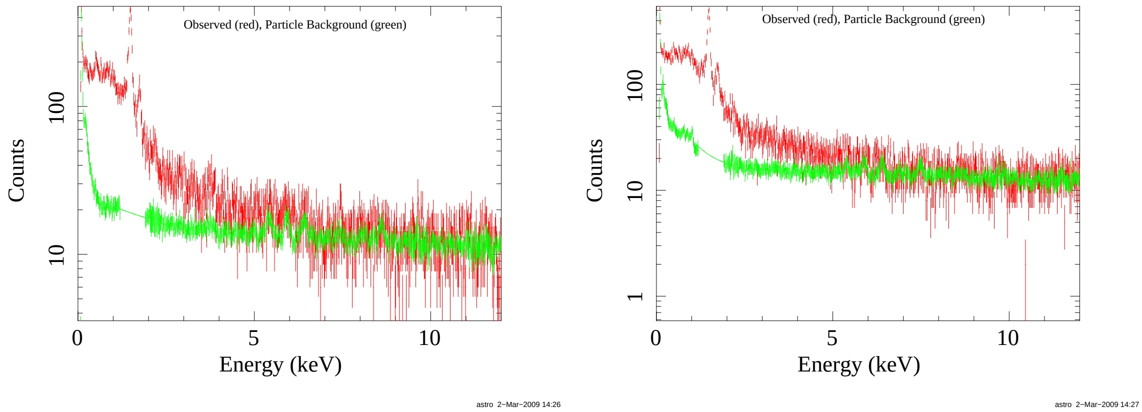

Figure 5.10. Abell 3705, observed spectrum and the model background spectrum of MOS1 and MOS2, respectively

Surface brighteness (Figure 4.11) in soft energy band of the observed spectrum (0.35-1.25 keV) is dominant compared to the hard enrgy band (0.20-8.00 keV) and continues until the edge of the camera first in a decreasing manner. Model partical background brightness is always higher than observed data. In hard band (lower panel), model partical background increases until the edge of the camera. Observed spectrum's surface brightness is very low compared to that of model partical bacground.

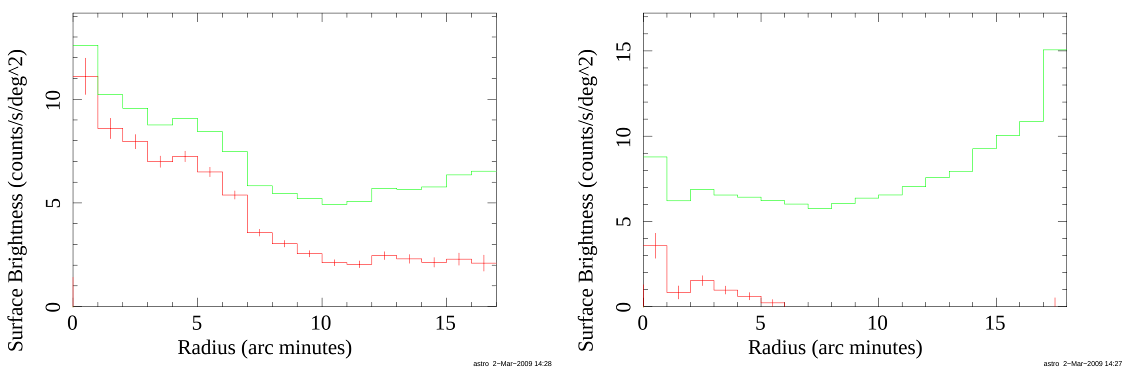

Figure 5.11. Abell 3705, radial profiles of the data for the 350-1250 eV and 200-8000 eV energy bands of the whole field of view

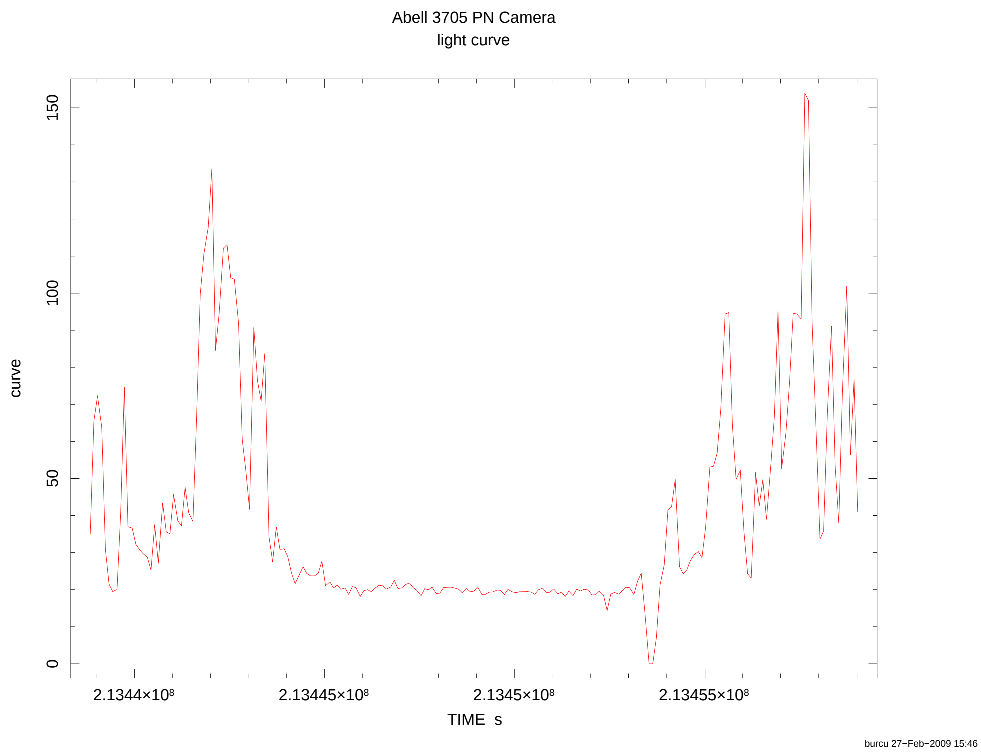

Figure 5.12. Abell 3705, unfiltered light curve of the PN data

The selected background spectra is compared with the observed data spectra (Figures 4.12 & 4.13). Spectrum of the region A (top of the figure) is above its background spectra up to $\sim$ 5 keV. After this point background begins to reach the same level. The observed spectrum B (second) is above the background spectrum up to $\sim$ 4 keV. Background begins to reach the same level after this. The spectrum of the region C shows the same behavior like region B. The spectrum of the region D (Figure 4.24, top) is also close to the background spectrum.The spectrum of the region E is always below the background spectrum. There is a clear instrumental emission line at $\sim$ 8 kev in both background and observed spectra of regions B, C, D and E. All spectra cover the energy range of 0.30-10.00 keV.

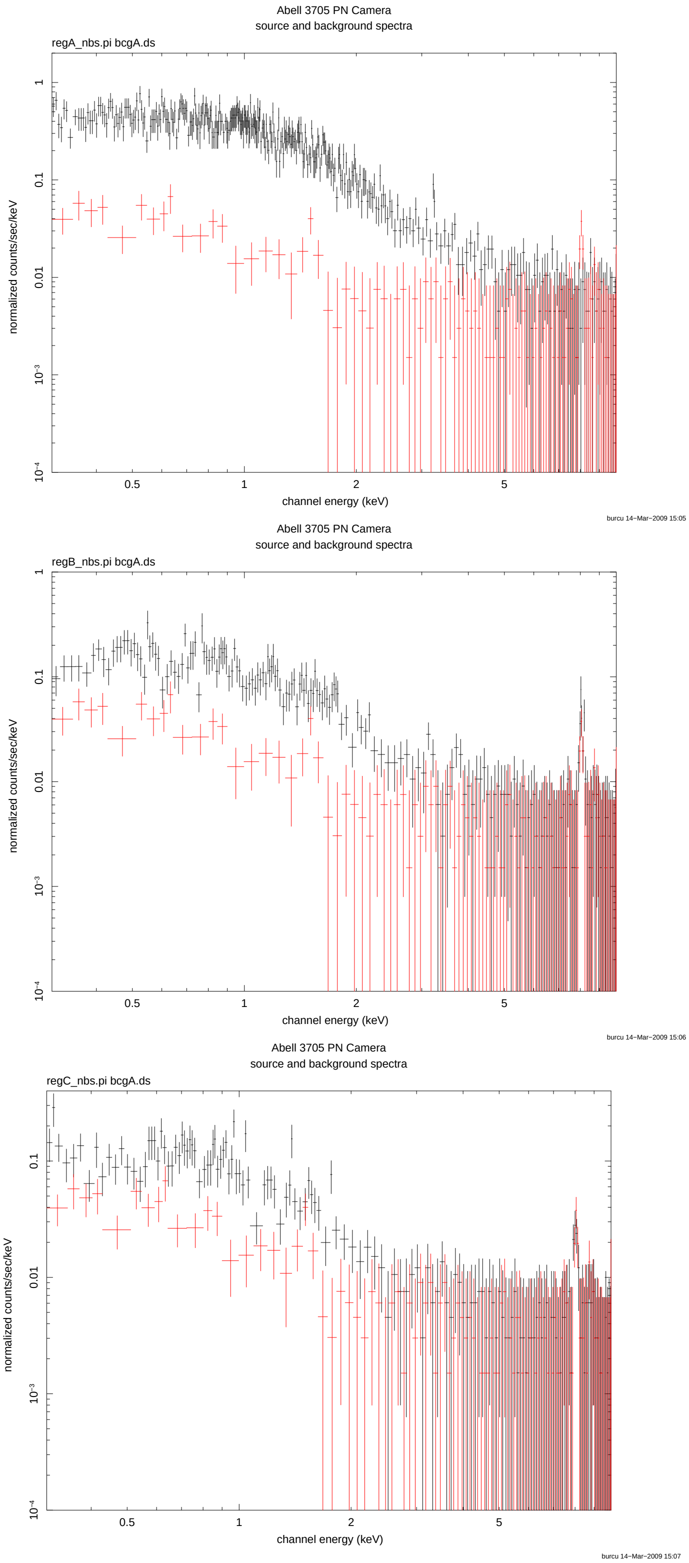

Figure 5.13. Abell 3705, selected regions (A,B and C) and their background spectra of the PN data

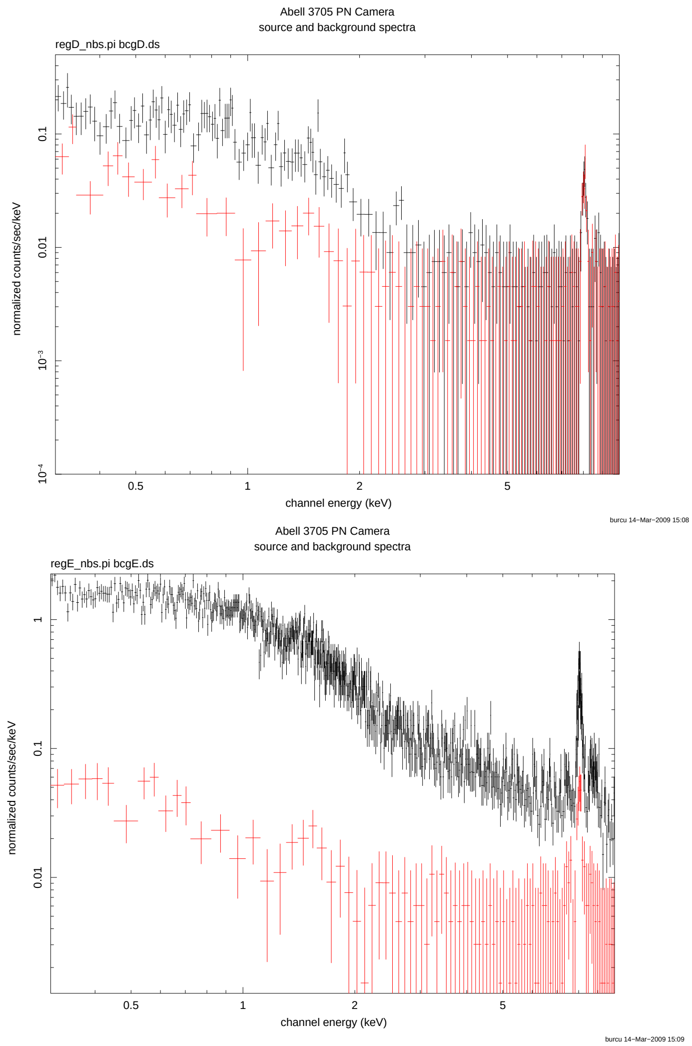

Figure 5.14. Abell 3705, observed and background spectra of regions D &E from PN

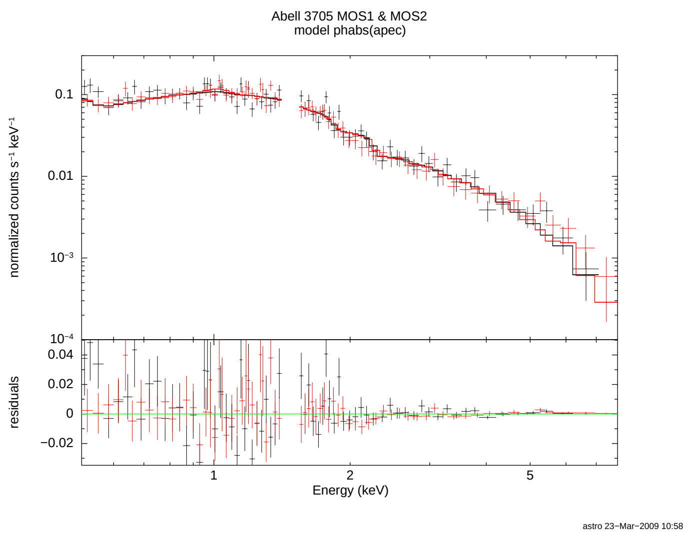

Figure 5.15. Abell 3705, MOS1 and MOS2 spectral fit (APEC) of region A

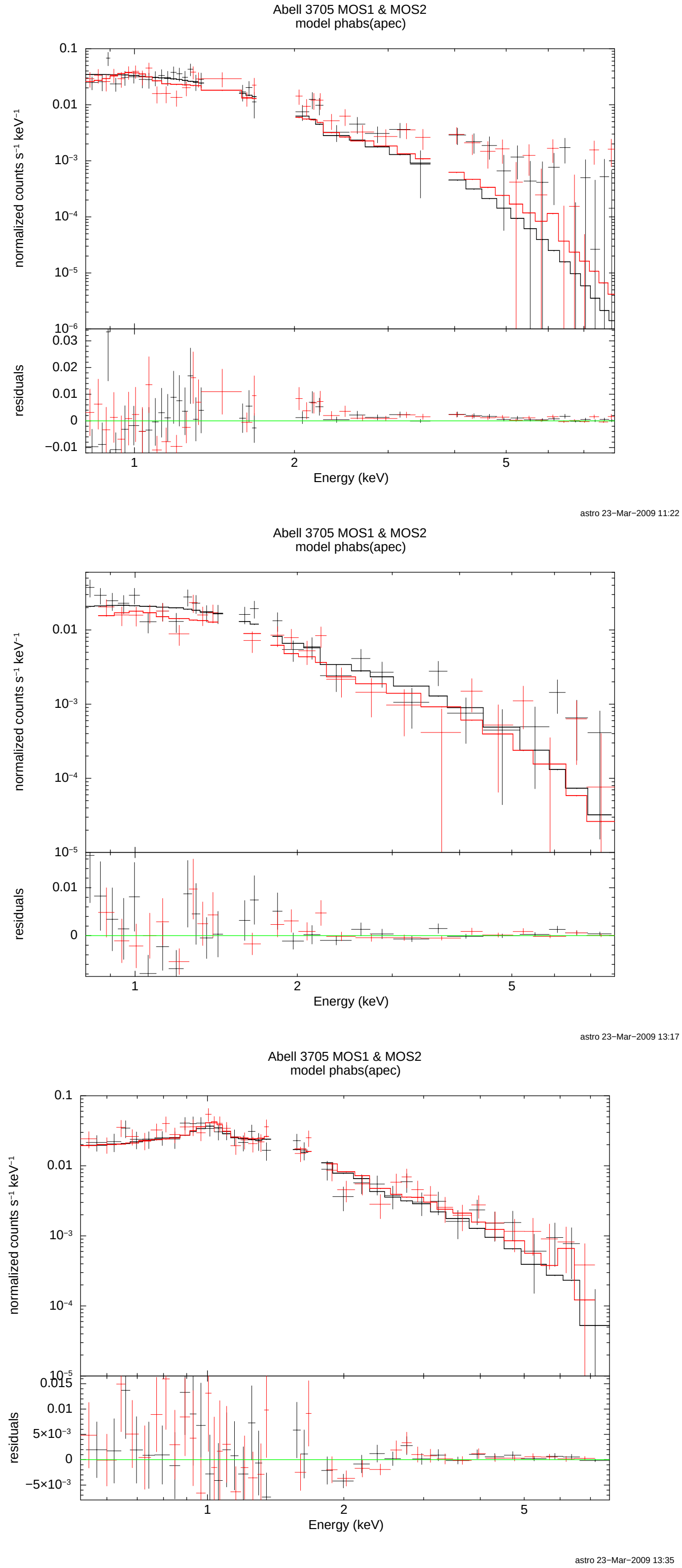

Figure 5.16. Abell 3705, MOS1 and MOS2 spectral fit (APEC) of three regions (B, C and D)

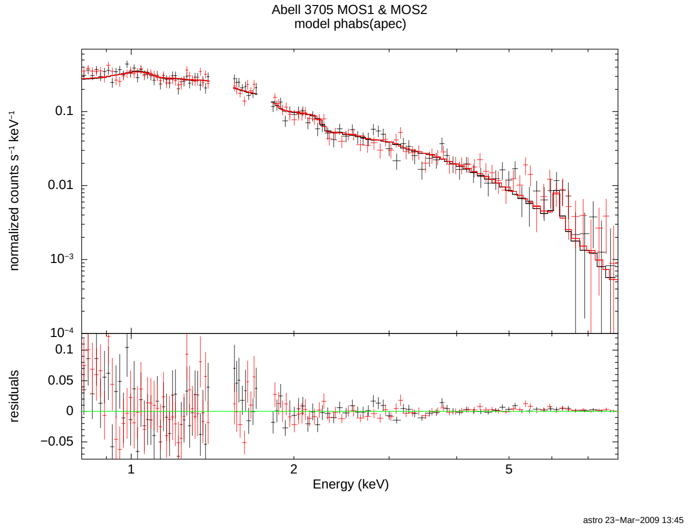

Figure 5.17. Abell 3705, MOS1 and MOS2 spectral fit (APEC) of region E

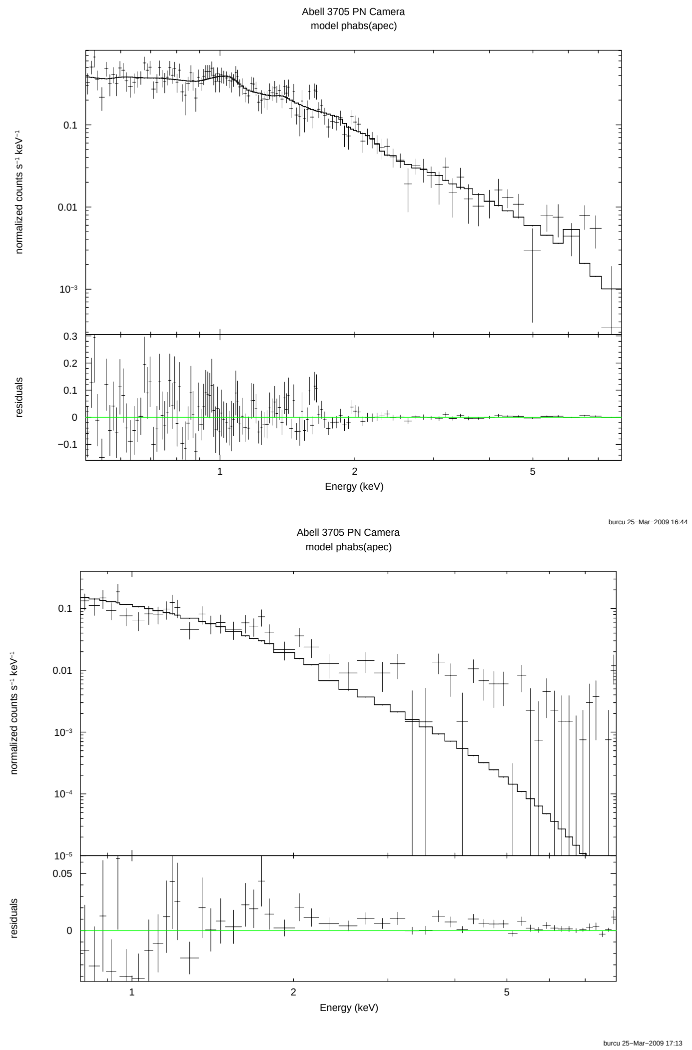

Figure 5.18. Abell 3705, PN spectral fit (APEC) of regions A and B

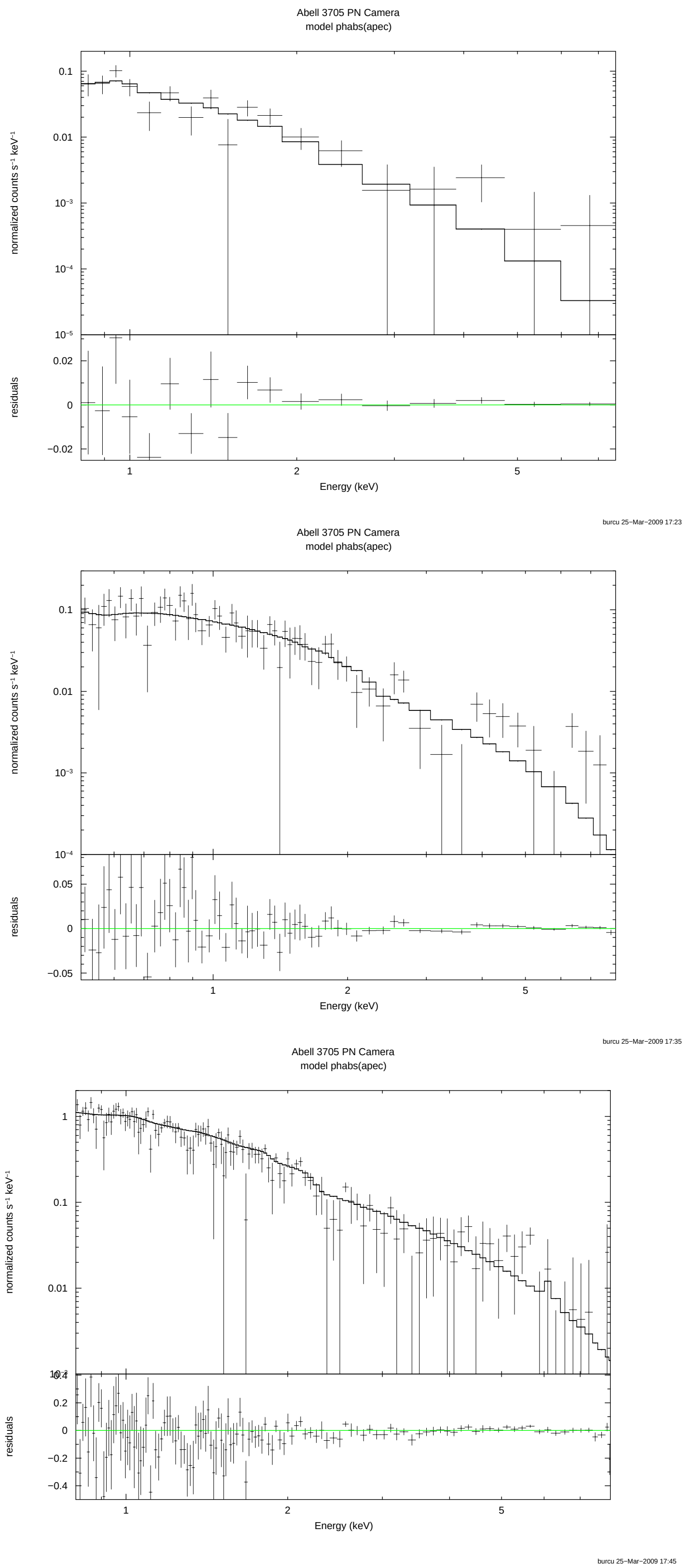

Figure 5.19. Abell 3705, PN spectral fit (APEC) of regions C, D and E

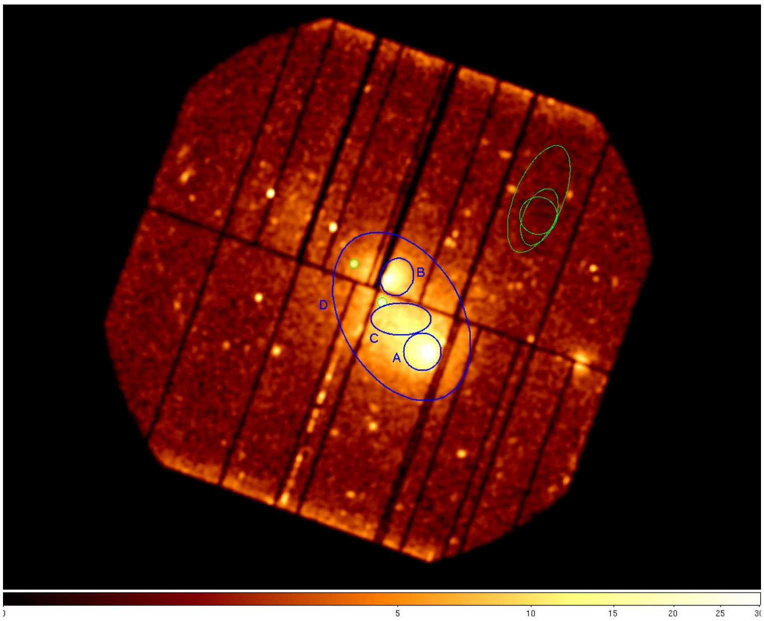

Figure 5.20. Abell 2440, raw image, regions chosen for spectral analysis on PN Camera

On the cameras, both regions A and B (Figures 5.20 and 5.21) cover 1 arc minutes.

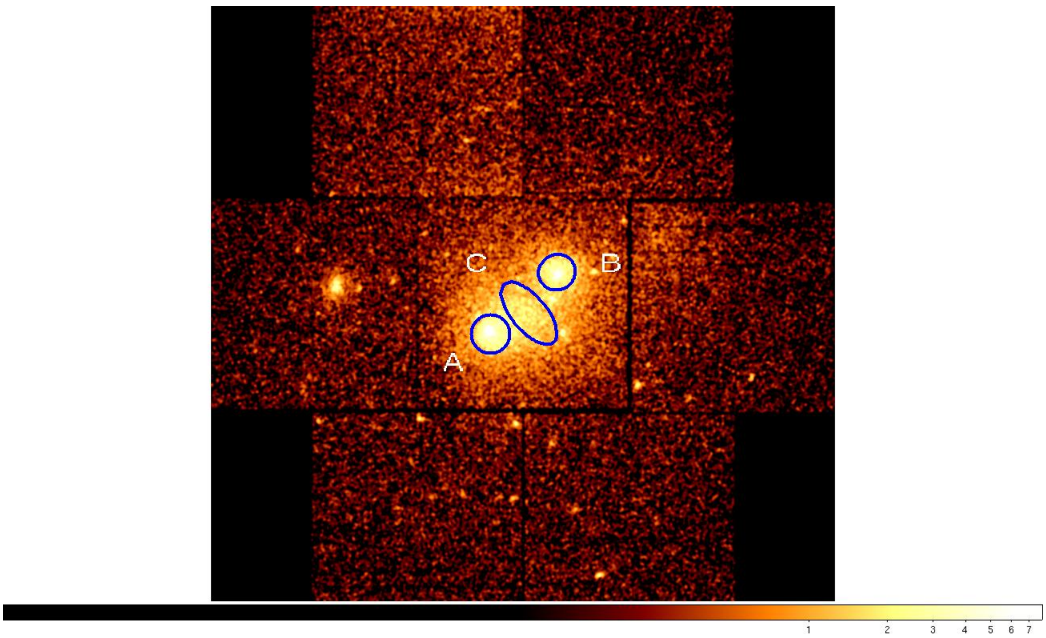

Figure 5.21. Abell 2440, raw image, regions chosen for spectral analysis on MOS2 Camera

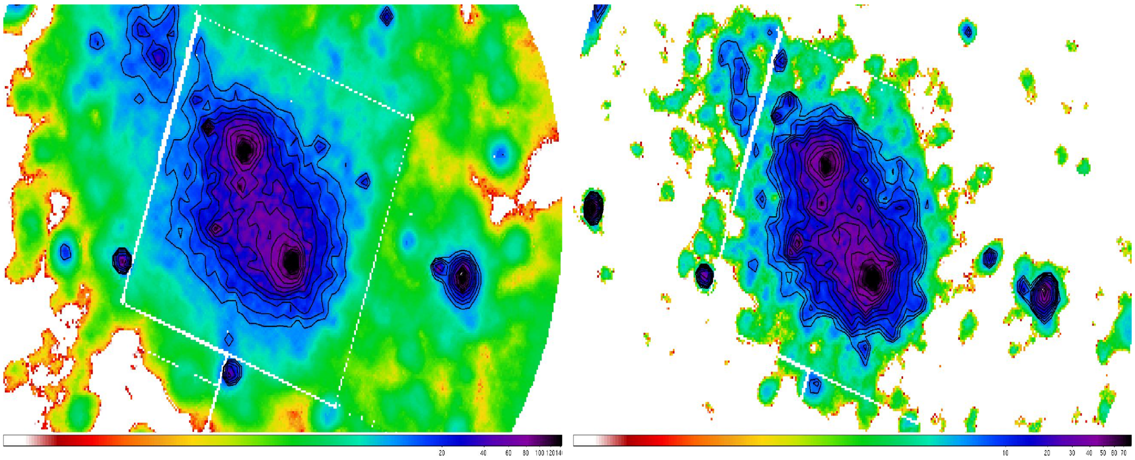

Figure 5.22. Abell 2440, background subtracted and exposure corrected image of MOS cameras in the (0.35-1.25) keV (left) and (2-8) keV (right)

The elongation between the two poles are clear in both soft and hard energy band. A structure connected to the region B is also present.

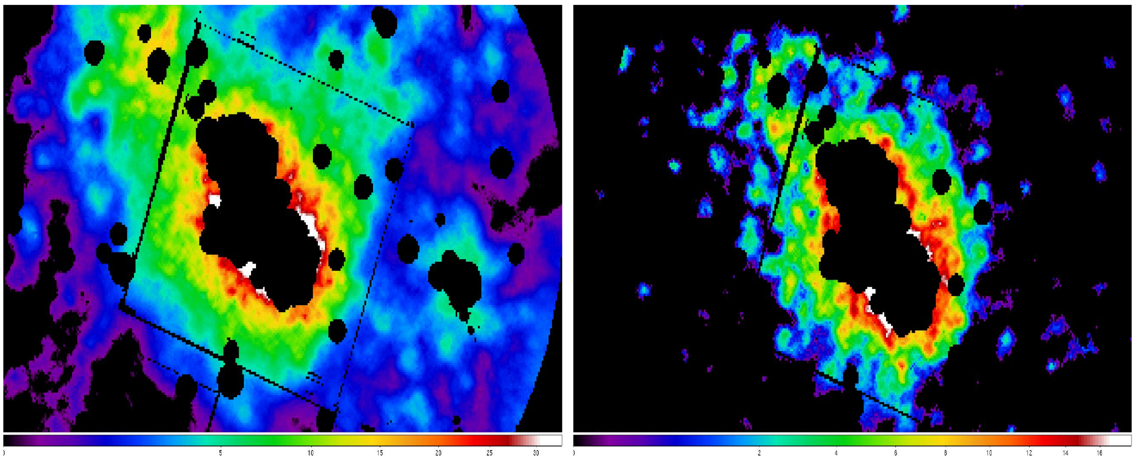

Figure 5.23. Abell 2440, background subtracted and exposure corrected image of MOS cameras with point sources are removed in the (0.35-1.25) keV (left) and (2-8) keV (right)

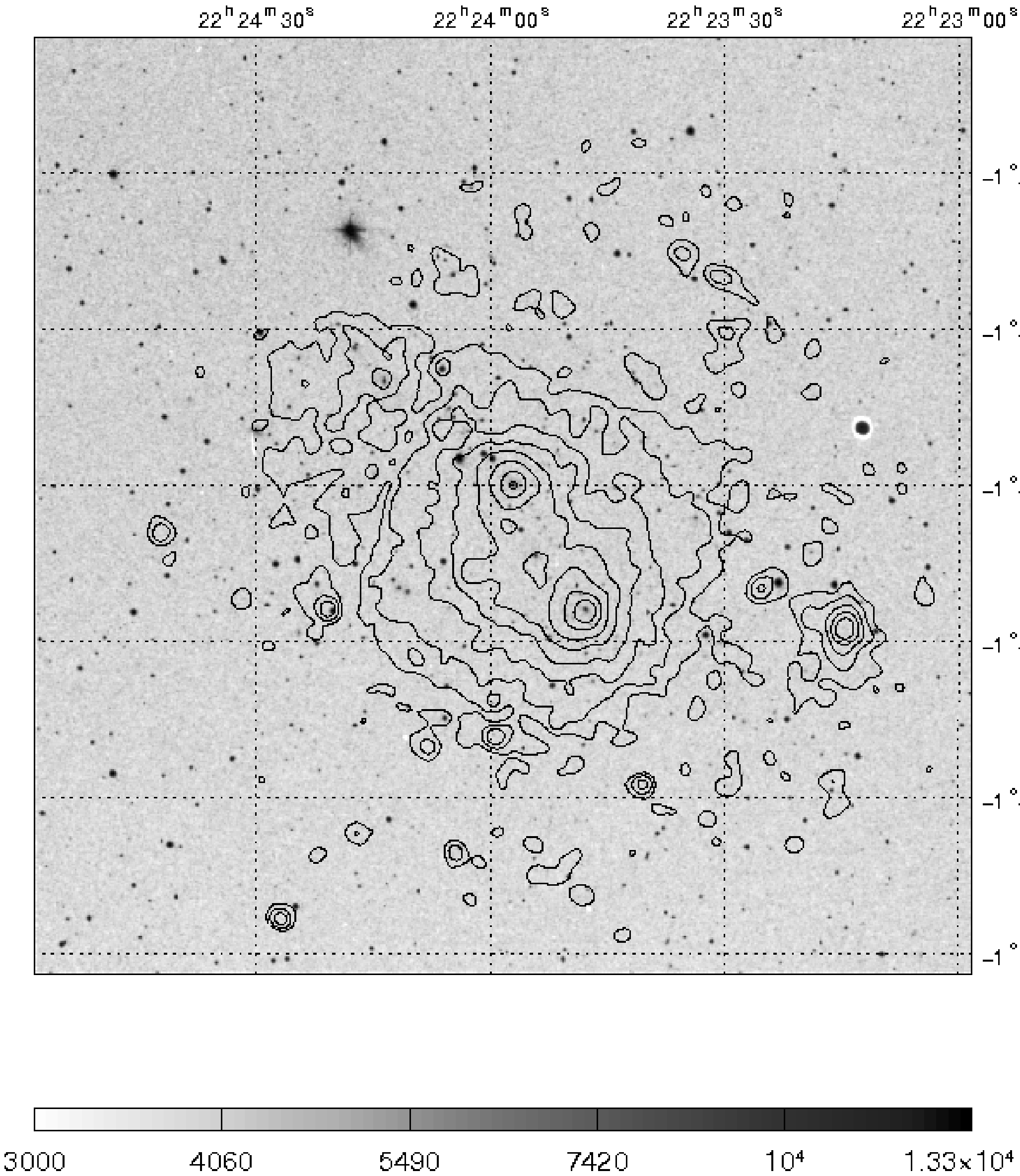

Figure 5.24. Abell 2440, X-ray contours over optical image

For each regions spectra of the two MOS cameras are fitted simultaneously. Spectral results are displayed in Table 4.3 as follows: For both MOS cameras, spectral fitting of the region A is done by using chi statistics. Spectra from MOS1, MOS2 and PN are grouped in 25. The spectral data counts of these spectra are 3681, 3933 and 8793, respectively. Reduced chi-squared are 1.1578 for 218 degrees of freedom, 1.0820 for 265 degrees of freedom and the null hypothesis probabilities are 5.489264e-02 and 1.714574e-01, respectively. Difference between weihgted mean value of the temperature and temperature from MOS1 is 0.6 σ, from MOS2 is 4.46 σ and from PN is 0.4 σ.

Difference between weihgted mean value of the metal abundance and metal abundance from MOS1 is 0.3 σ, from MOS2 is 3.1 σ and from PN is 1.3 σ.

For both MOS cameras and PN camera spectral fitting of the region B are done by using chi statistics. Spectrum from MOS1, MOS2 and PN are grouped in 15. The spectral data counts are 2633, 2913 and 4109 respectively. For MOS and PN cameras, reduced chi-squared are 1.0973 for 247 degrees of freedom, 0.91509 for 209 degrees of freedom and the null hypothesis probabilities are 1.406620e-01 and 8.053705e-01, respectively. Difference between weihgted mean value of the temperature and temperature from MOS1 is 1.47 σ, from MOS2 is 1.6 σ and from PN is 0.43 σ. Difference between weihgted mean value of the metal abundance and metal abundance from MOS1 is 0.57 σ, from MOS2 is 0.07 σ and from PN is 0.14 σ.

For both MOS cameras and PN camera spectral fitting of the region C are done by using chi statistics. Spectrum from MOS1, MOS2 and PN are grouped in 15. The spectral data counts are 3321, 3531, and 6080 respectively. For MOS and PN cameras, reduced chi-squared are 1.0167 for 297 degrees of freedom, 0.97966 for 294 degrees of freedom and the null hypothesis probabilities are 4.092152e-01 and 5.873766e-01, respectively. Difference between weihgted mean value of the temperature and temperature from MOS1 is 0.63 σ, from MOS2 is 1.83 σ and from PN is 0.53 σ. Difference between weihgted mean value of the metal abundance and metal abundance from MOS1 is 2.13 σ, from MOS2 is 1.63 σ and from PN is 2.5 σ.

For both MOS cameras and PN camera spectral fitting of the region D are done by using chi statistics. Spectrum from MOS1, MOS2 and PN are grouped in 25 and in 45, respectively. The spectral data counts are 24902, 25690, and 40153 respectively. For MOS and PN cameras, reduced chi-squared are 0.96005 for 586 degrees of freedom, 1.0952 for 476 degrees of freedom and the null hypothesis probabilities are 7.497213e-01 and 7.401127e-02, respectively. Difference between weihgted mean value of the temperature and temperature from MOS1 is 1.13 σ, from MOS2 is 1.13 σ and from PN is 1.5 σ. Difference between weihgted mean value of the metal abundance and metal abundance from MOS1 is 0.6 σ, from MOS2 is 3 σ and from PN is 2.3 σ.

Table 5.3. Abell 2440, spectral results of temperature and metal abundances for each regions and their errors

Regions	MOS1		MOS2		PN	
	temperature (keV) & err.	metal abundance (Z_o) & err.	temperature (keV) & err.	metal abundance (Z_o) & err.	temperature (keV) & err.	metal abundance (Z_o) & err.
A	3.90 -0.35/+0.37	0.60 -0.23/+0.26	4.66 -0.47/+0.52	0.26 -0.17/+0.19	3.93 -0.18/+0.18	0.70 -0.11/+0.13
B	3.56 -0.44/+0.43	0.54 -0.27/+0.34	3.15 -0.25/+0.27	0.63 -0.25/+0.29	3.37 -0.19/+0.25	0.64 -0.16/+0.18
C	4.18 -0.40/+0.57	0.03 -0.03/+0.15	4.54 -0.44/+0.52	0.07 -0.07/+0.14	3.83 -0.25/+0.25	0.40 -0.11/+0.12
D	4.27 -0.13/+0.13	0.36 -0.06/+0.06	4.27 -0.14/+0.18	0.29 -0.06/+0.06	4.06 -0.12/+0.12	0.45 -0.05/+0.05

Table 5.4. Abell 2440, weighted means and standart deviations of spectral results

Regions	weighted mean		standart deviation (σ)	
	temperature (keV)	metal abundance (Z_o)	temperature (keV)	metal abundance (Z_o)
A	3.99	0.57	0.15	0.1
B	3.31	0.62	0.17	0.14
C	3.99	0.2	0.30	0.08
D	4.18	0.38	0.08	0.03

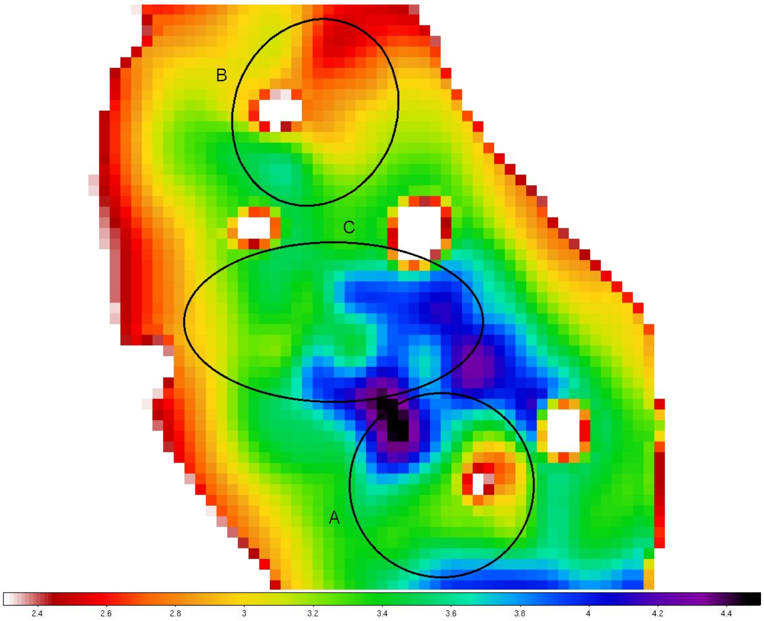

Figure 5.25. Abell 2440, temperature map extracted with XWSM. Color diagram is between 2.4-4.4 keV

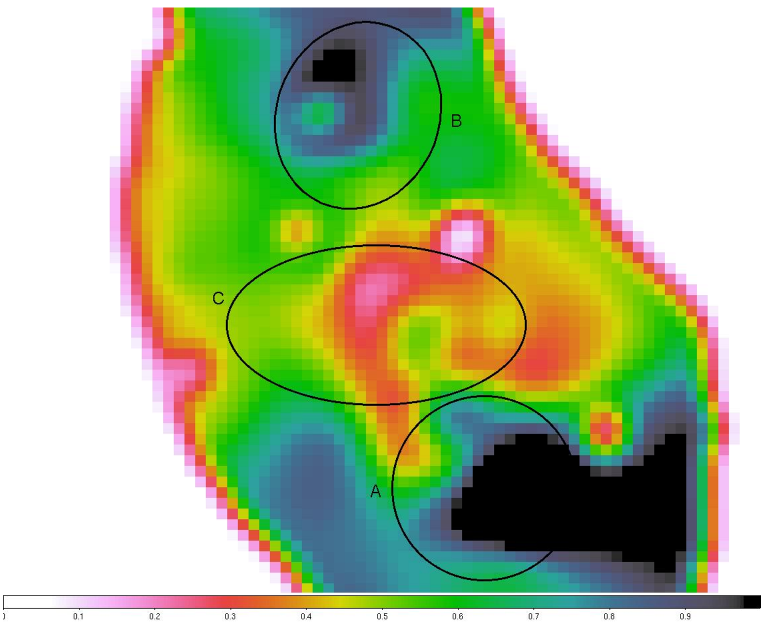

Figure 5.26. Abell 2440, metalicity map extracted with XWSM. Color diagram is between 0.1-0.9 Z_o

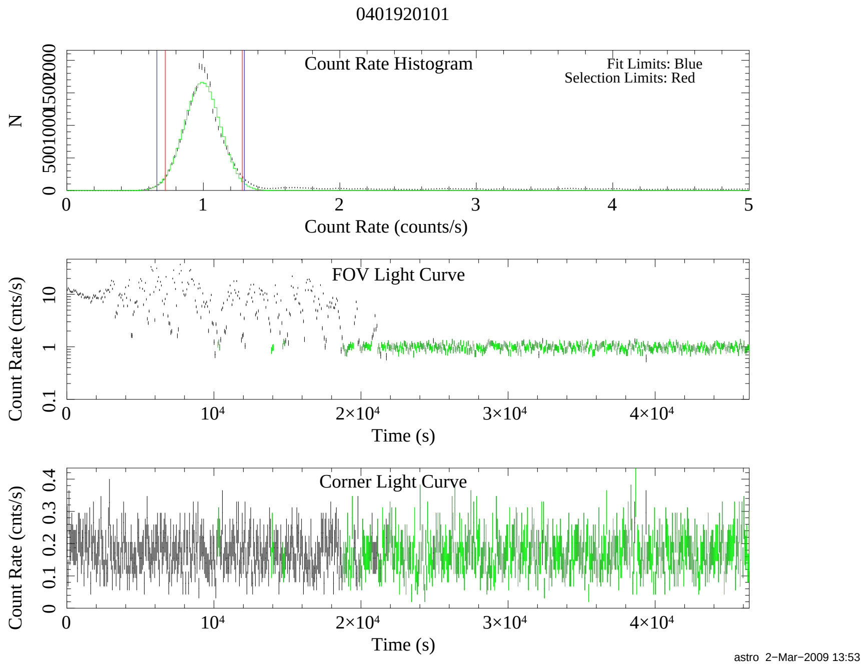

Figure 5.27. Abell 2440, temporal filtering resultsfor the MOS1 observation

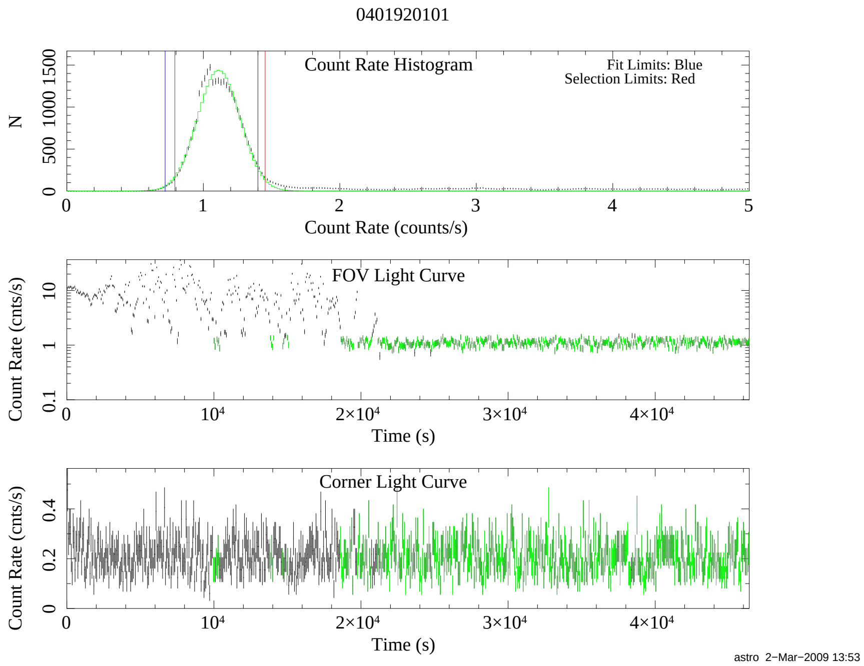

Figure 5.28. Abell 2440, temporal filtering resultsfor the MOS2 observation

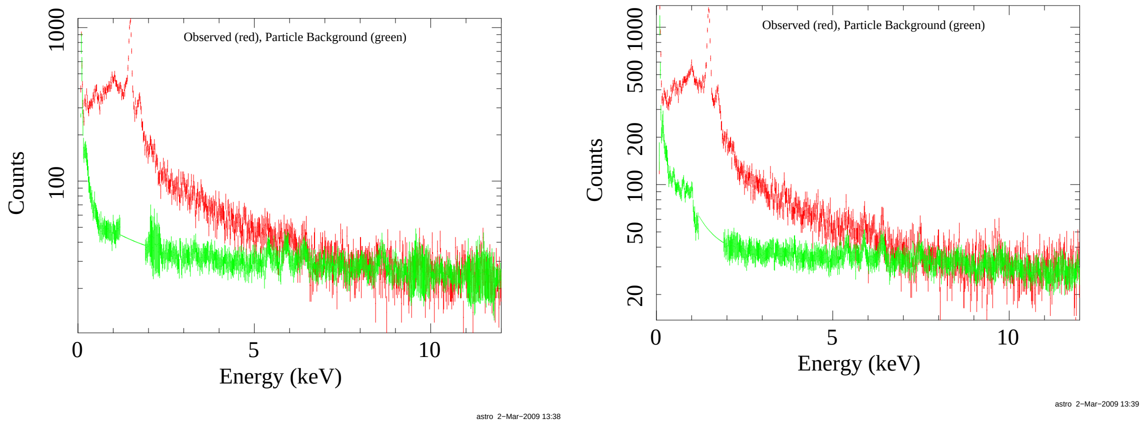

Figure 5.29. Abell 2440, observed spectrum and the model background spectrum of MOS1 and MOS2, respectively

Surface brighteness in soft energy band (Figure 4.30) of the observed spectrum (0.35-1.25 keV) is dominant compared to the hard enrgy band (0.20-8.00 keV) and continues until the near edge of the camera in a decreasing manner. It is below the model partical bacground specrum's brightness. In hard band, model partical background is nearly constant along the camera only around the radius 14 arc minutes it begins to increaseand continues until the edge of the camera. Surface brightness of the observed spectrum is very low.

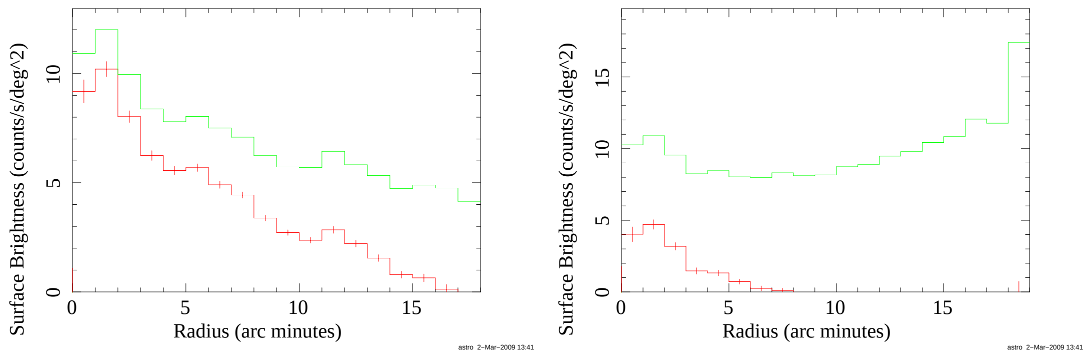

Figure 5.30. Abell 2440, radial profiles of the data for the (350-1250) eV and (200-8000) eV energy bands of the whole field of view

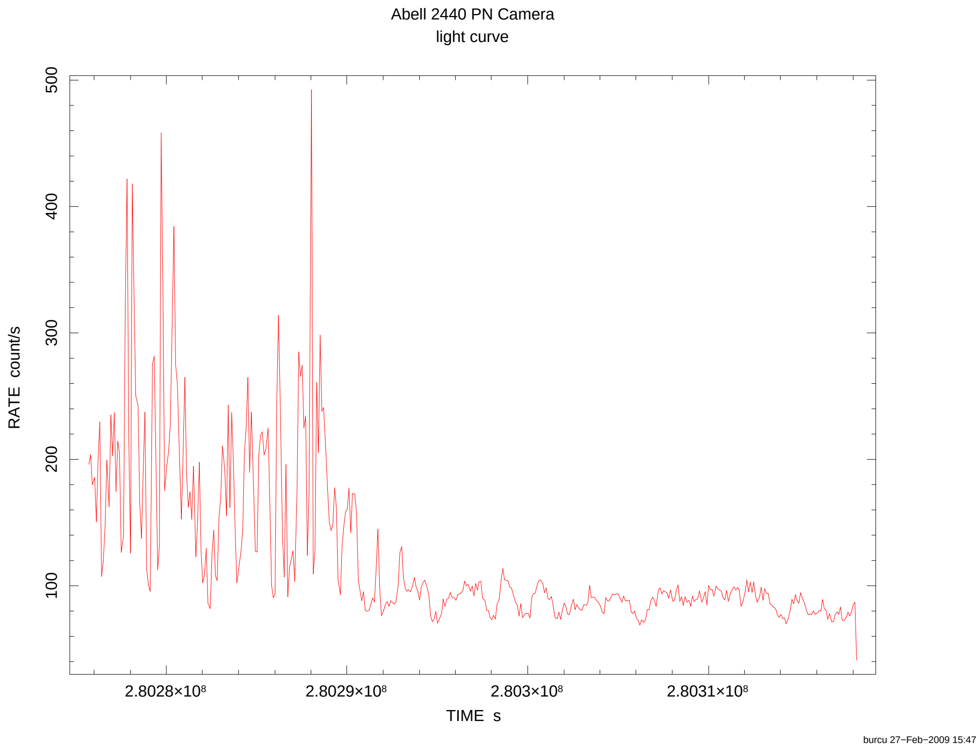

Figure 5.31. Abell 2440, unfiltered light curve of the PN data

We compared the selected background spectrum with the spectrum of the region which we want to make spectral anlysis (Figure 4.32). Spectra of the four regions are above their background spectra. Onlt at higher energies, around 7 keV, background and data spectra coincide. Instrumenral emission line around 8 keV and the Fe line around 6 keV are clearly seen in all spectra. All the spectra cover the energy range 0.30-10.00 keV.

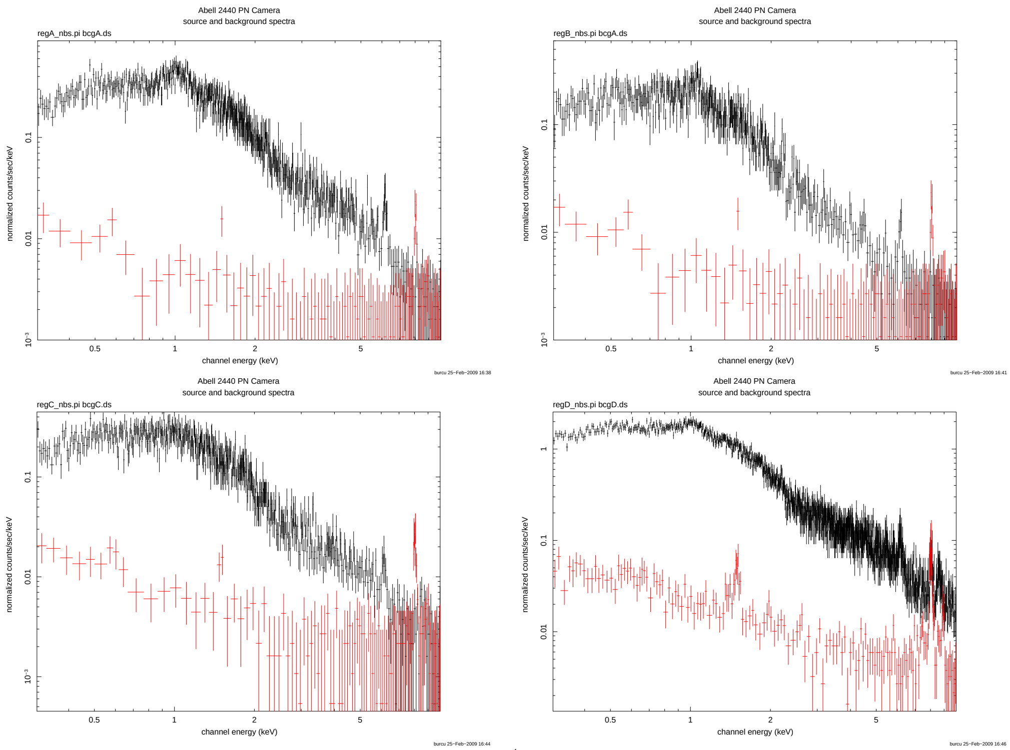

Figure 5.32. Abell 2440, selected regions (from left to right, top to bottom A, B, C, D) and their background spectra of the PN data

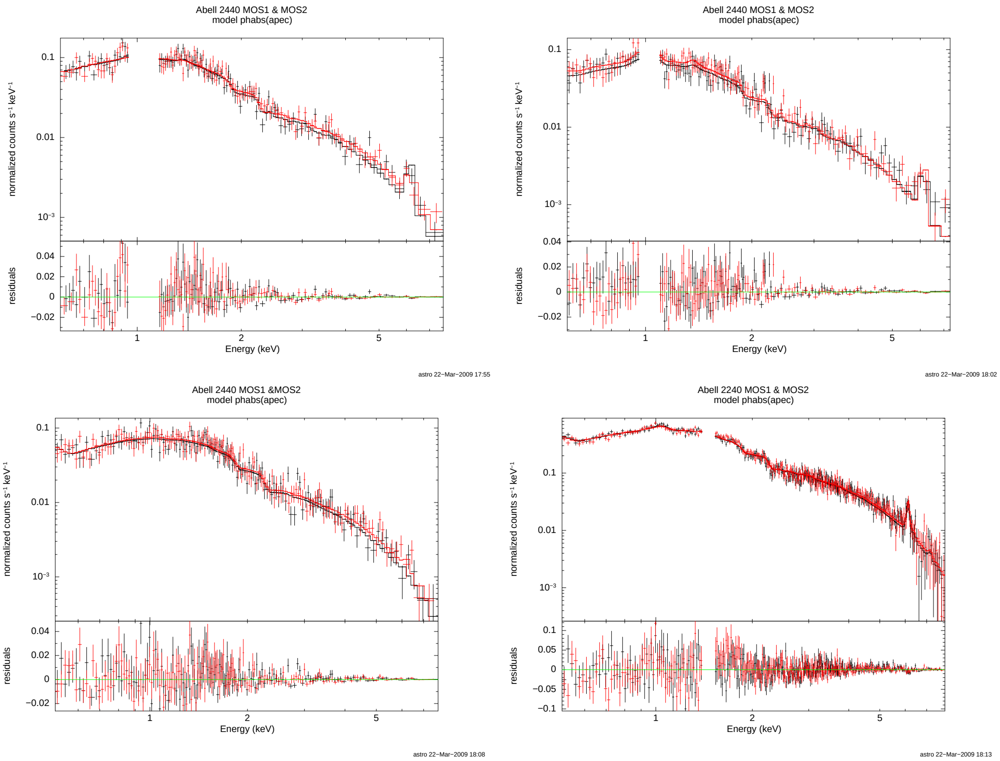

Figure 5.33. Abell 2440, MOS1 and MOS2 spectral fit (APEC) of the four regions (from left to right, top to bottom A, B, C, D)

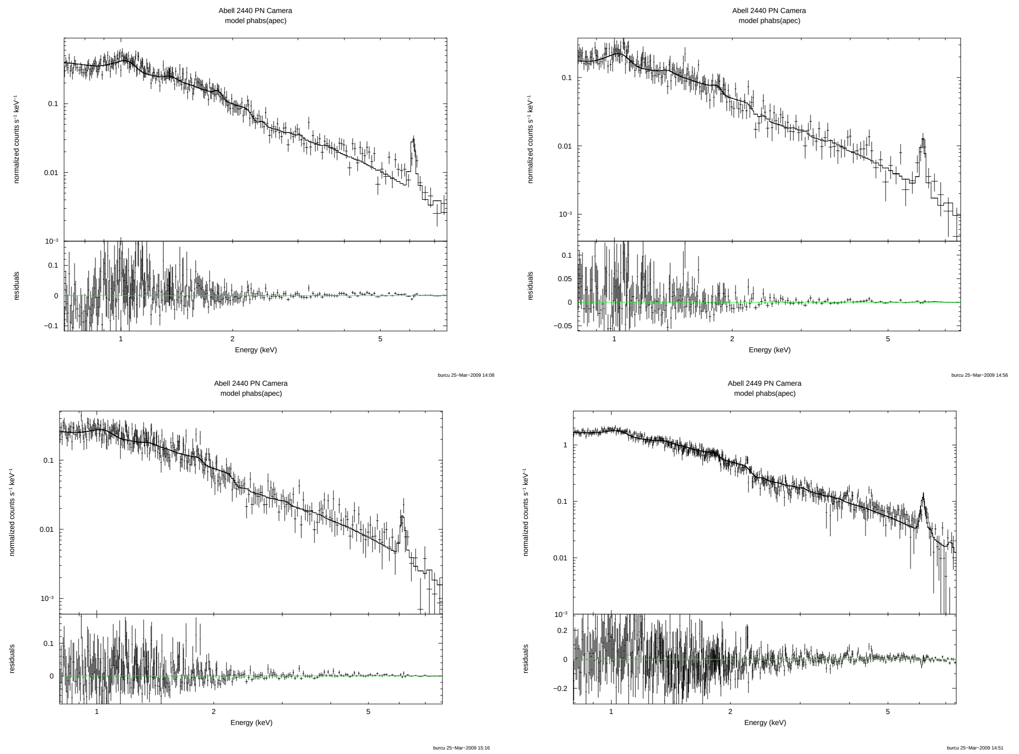

Figure 5.34. Abell 2440, PN spectral fit (APEC) of the four regions (from left to right, top to bottom A, B, C, D)

5.3. Abell 2933

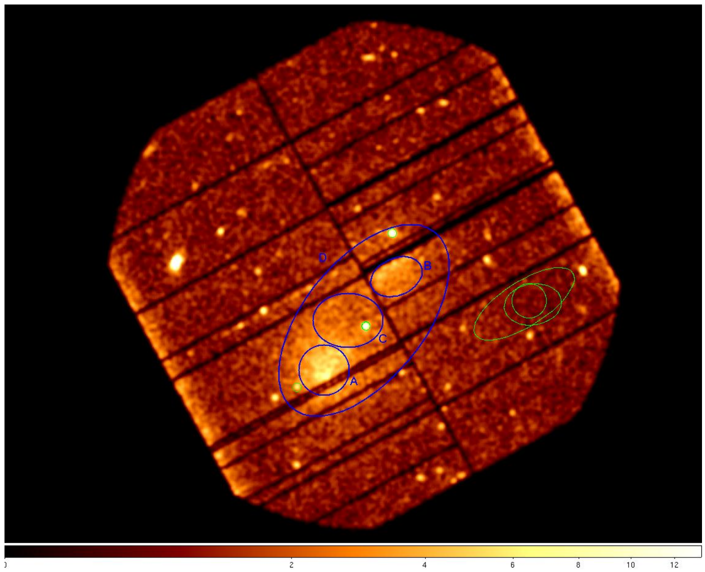

Figure 5.35. Abell 2933, raw image, regions chosen for spectral analysis on PN camera

On the cameras, both regions A and B (Figures 5.35 and 5.36) cover $\sim$ 1.5 arc minutes, Region B is an ellipse.

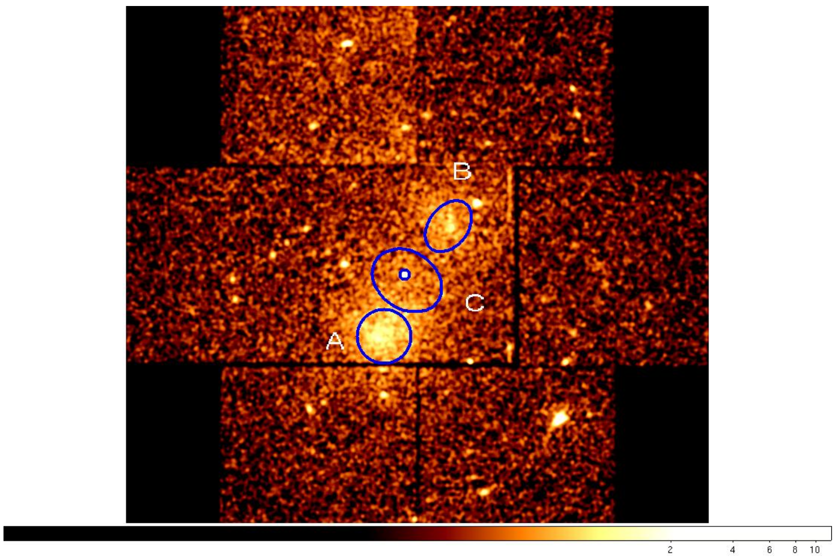

Figure 5.36. Abell 2933, raw image, regions chosen for spectral analysis on MOS2 camera

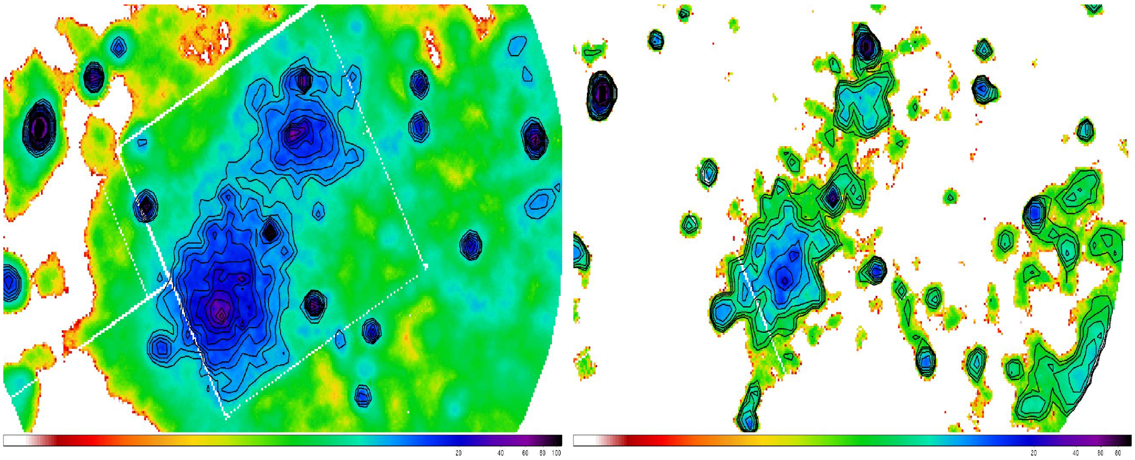

Figure 5.37. Abell 2933, Background subtracted and exposure corrected image of MOS cameras in the (0.35-1.25) keV (left) and (2-8) keV (right)

The elongation between the two poles are more clear in the soft band (Figure 4.37). In the hard band structure of the binary system is weak and not very detailed. There is no a strong connection between the two subtructures.

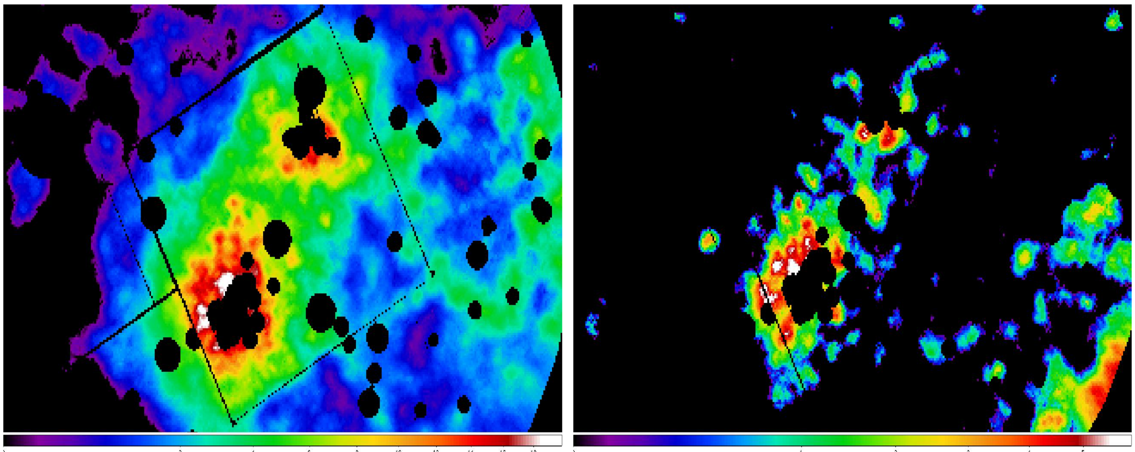

Figure 5.38. Abell 2933, background subtracted and exposure corrected image of MOS cameras with point sources are removed in the (0.35-1.25) keV (left) and (2-8) keV (right)

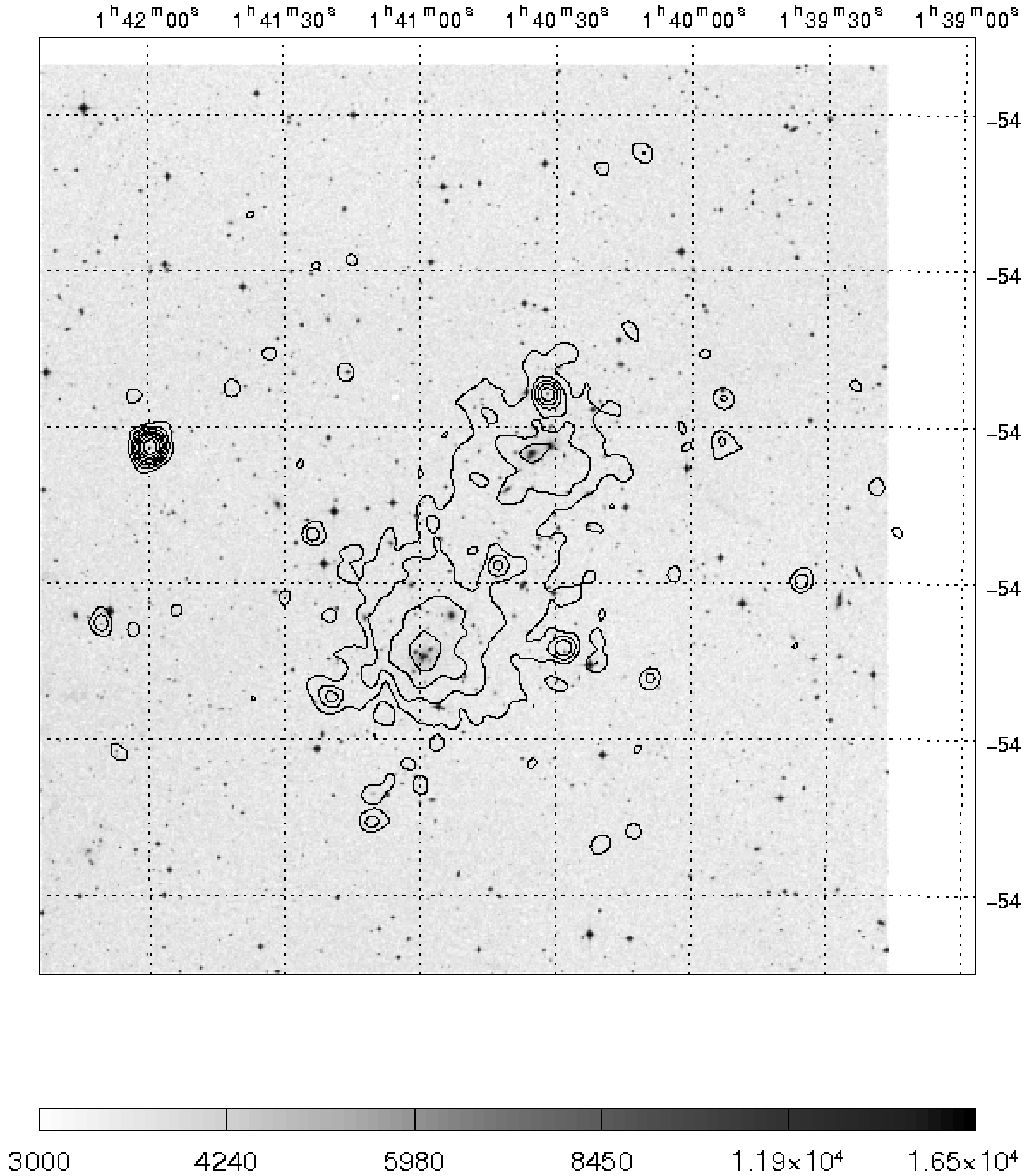

Figure 5.39. Abell 2933, X-ray contours over optical image

For each regions spectra of the two MOS cameras are fitted simultaneously. Spectral results are displayed in table 4.5 as follows: For both MOS cameras, spectral fitting of the region A is done by using chi statistics. Spectra from MOS1 and MOS2 are grouped in 15 and that of PN in 25. The spectral data counts of these spectra are 2098, 2185 and 4058, respectively. Reduced chi-squared are 0.72779 for 208 degrees of freedom, 0.98459 for 133 degrees of freedom and the null hypothesis probabilities are 9.988324e-01 and 5.340305e-01, respectively. Difference between weihgted mean value of the temperature and temperature from MOS1 is 0.15 σ, from MOS2 is 1.5 σ and from PN is 1.05 σ. Difference between weihgted mean value of the metal abundance and metal abundance from MOS1 is 2.6 σ, from MOS2 is 1 σ and from PN is 0.6 σ.

For both MOS cameras and PN camera spectral fitting of the region B are done by using chi statistics. Spectrum from MOS1, MOS2 and PN are grouped in 10 and 15, respectively. The spectral data counts are 1094, 1090 and 2134 respectively. For MOS and PN cameras, reduced chi-squared are 0.91943 for 163 degrees of freedom, 0.96832 for 121 degrees of freedom and the null hypothesis probabilities are 7.613494e-01 and 5.816316e-01, respectively. Difference between weihgted mean value of the temperature and temperature from MOS1 is 0.53 σ, from MOS2 is 0.09 σ and from PN is 0.53 σ. Difference between weihgted mean value of the metal abundance and metal abundance from MOS1 is 3 σ, from MOS2 is 3.3 σ and from PN is 0.57 σ.

For both MOS cameras and PN camera spectral fitting of the region C are done by using chi statistics. Spectrum from MOS1, MOS2 and PN are grouped in 25 and 35, respectively. The spectral data counts are 1347, 1495 and 3100 respectively. For MOS and PN cameras, reduced chi-squared are 0.97868 for 146 degrees of freedom, 1.086 for 78 degrees of freedom and the null hypothesis probabilities are 5.573894e-01 and 2.829015e-01, respectively. Difference between weihgted mean value of the temperature and temperature from MOS1 is 0.14 σ, from MOS2 is 0.88 σ and from PN is 1.34 σ. Difference between weihgted mean value of the metal abundance and metal abundance from MOS2 is 0.3 σ and from PN is 3 σ.

For both MOS cameras and PN camera spectral fitting of the region D are done by using chi statistics. Spectrum from MOS1, MOS2 and PN are grouped in 35 and 85, respectively. The spectral data counts are 9735, 9871 and 18741 respectively. For MOS and PN cameras, reduced chi-squared are 0.96161 for 324 degrees of freedom, 1.17229 for 176 degrees of freedom and the null hypothesis probabilities are 6.803794e-01 and 5.796729e-02, respectively. Difference between weihgted mean value of the temperature and temperature from MOS1 is 0.07 σ, from MOS2 is 0.07 σ and from PN is 0.07 σ. Difference between weihgted mean value of the metal abundance and metal abundance from MOS1 is 0.6 σ, from MOS2 is 0 σ and from PN is 0.8 σ.

Table 5.5. Abell 2933, spectral results of temperature and metal abundances for each regions and their errors

Regions	MOS1		MOS2		PN	
	temperature (keV) & c.r.	metal abundance (Z_o) & c.r.	temperature (keV) & c.r.	metal abundance (Z_o) & c.r.	temperature (keV) & c.r.	metal abundance (Z_o) & c.r.
A	2.92 -0.30/+0.34	0.45 -0.19/+0.25	3.25 -0.34/+0.38	0.12 -0.12/+0.18	2.74 -0.25/+0.33	0.27 -0.12/+0.15
B	2.56 -0.38/+0.58	0.33 -0.12/+0.31	2.70 -0.38/+0.55	0.35 -0.22/+0.38	2.90 -0.48/+0.55	0.08 -0.08/+0.20
C	3.09 -0.52/+0.64	0 +0.20	2.76 -0.42/+0.51	0.03 -0.03/+0.17	3.51 -0.58/+0.69	0.13 -0.13/+0.26
D	2.93 -0.24/+0.24	0.07 -0.07/+0.08	2.95 -0.23/+0.23	0.10 -0.07/+0.08	2.93 -0.29/+0.29	0.14 -0.09/+0.10

Table 5.6. Abell 2933, weighted means and standart deviations of spectral results

Regions	weighted mean		standart deviation (σ)	
	temperature (keV)	metal abundance (Z_o)	temperature (keV)	metal abundance (Z_o)
A	2.95	0.21	0.20	0.09
B	2.73	0.12	0.32	0.07
C	3.04	0.04	0.35	0.03
D	2.94	0.10	0.14	0.05

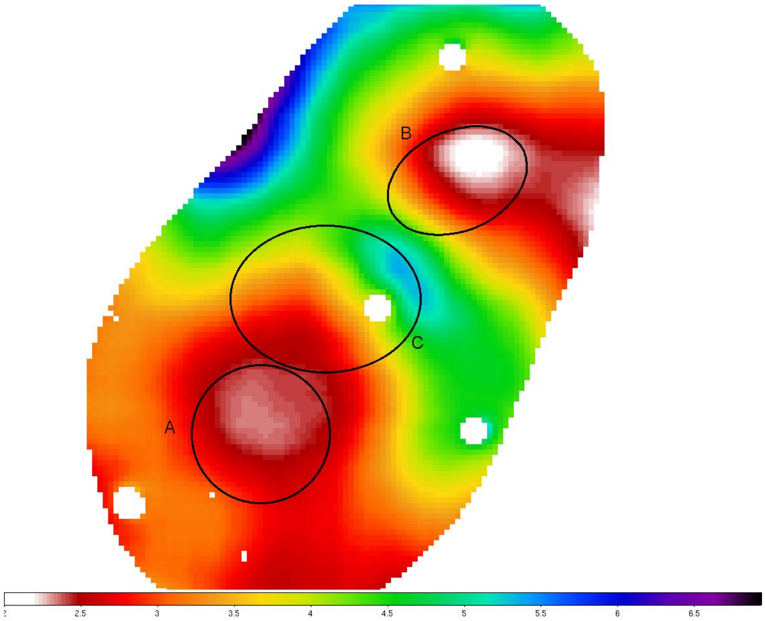

Figure 5.40. Abell 2933, temperature map extracted with XWSM. Color diagram is between 2-6.5 keV

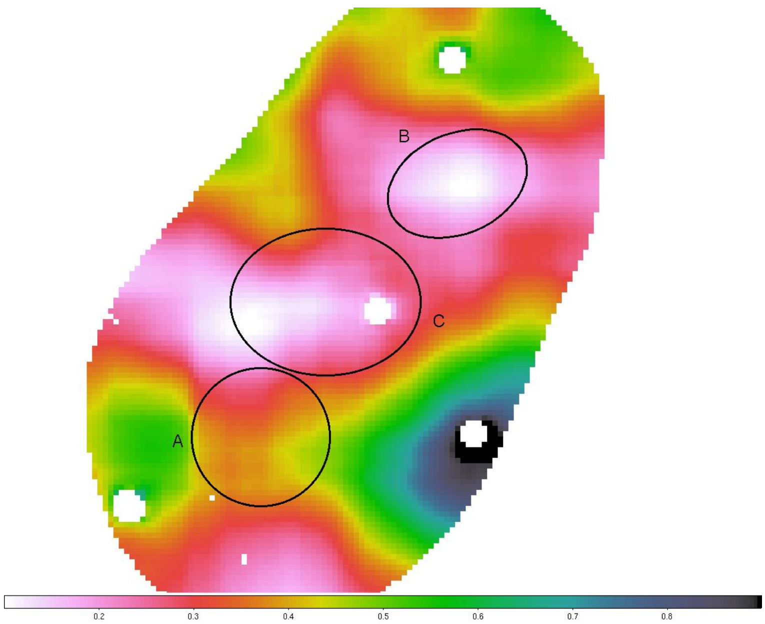

Figure 5.41. Abell 2933, metalicity map extracted with XWSM. Color diagram is between 0.2-0.8 Z_o

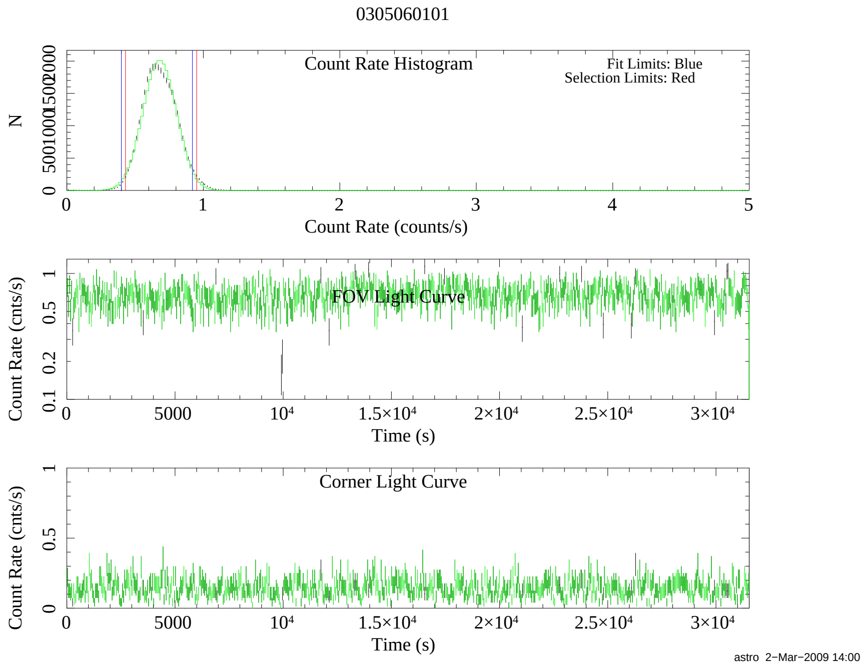

Figure 5.42. Abell 2933, temporal filtering resultsfor the MOS1 observation

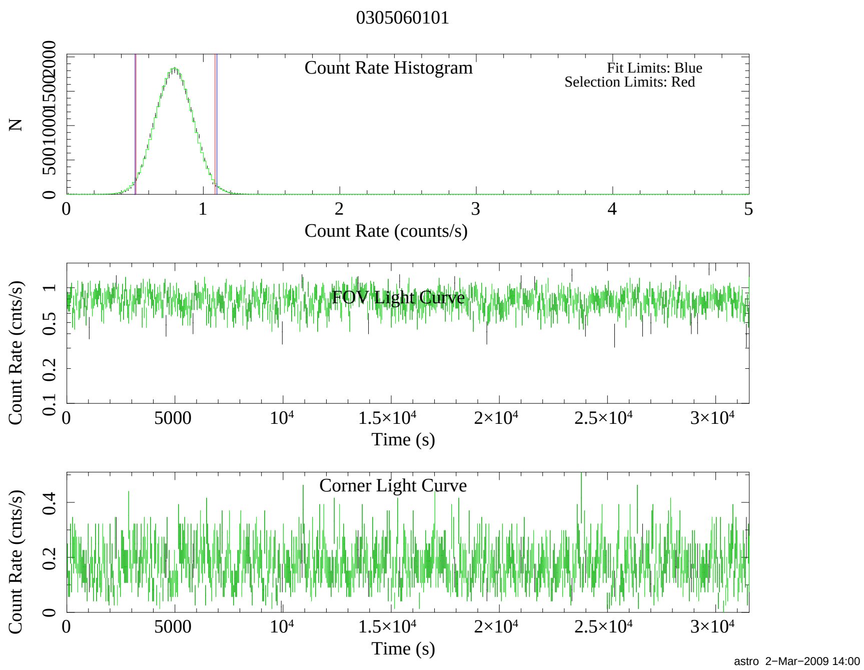

Figure 5.43. Abell 2933, temporal filtering resultsfor the MOS2 observation

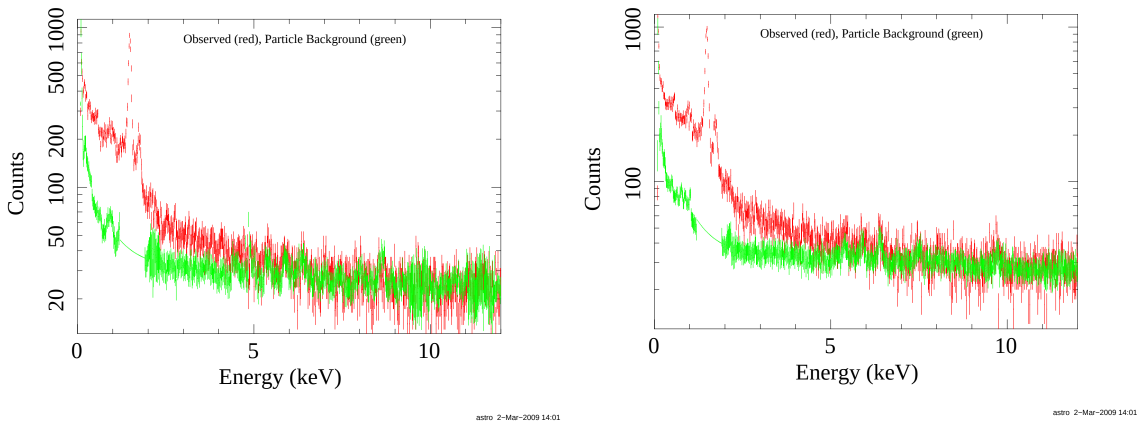

Figure 5.44. Abell 2933, observed spectrum and the model background spectrum of MOS1 and MOS2, respectively

Surface brighteness in soft energy band (Figure 4.45, left) of the observed spectrum (0.35-1.25 keV) is dominant compared to the hard enrgy band (0.20-8.00 keV) which is not seen, and continues until the near edge of the camera first in an increasing manner than in a decreasing manner. Both observed and model partical background brighteness make a pick around the radius 4 arc minute. Model partical background brightness is constant until the edge of the camera and always higher than observed data. In hard band, model partical backgroundincreases until the edge of the camera.

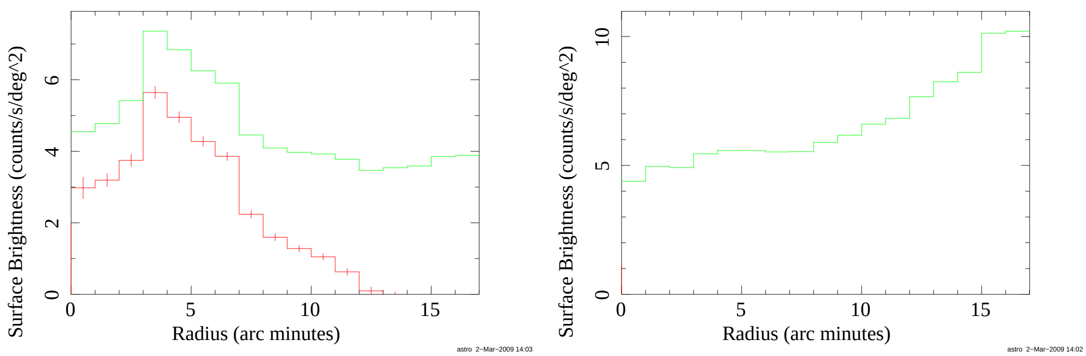

Figure 5.45. Abell 2933, radial profiles of the data for the (350-1250) eV and (200-8000) eV enrgy bands of the whole field of view

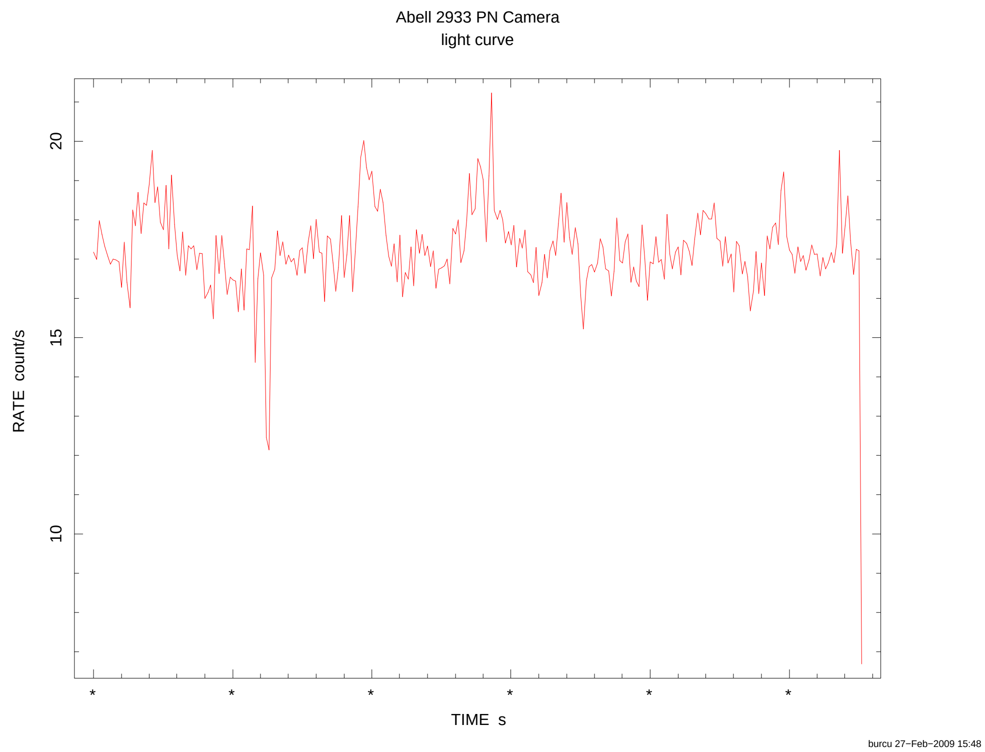

Figure 5.46. Abell 2933, unfiltered light curve of the PN data

We compared the selected background spectrum with the spectrum of the region which we want to make spectral anlysis (Figure 4.47). Spectra of the regions A and B (top of the figure) are above their background spectra until the 5 keV. After this point background begin to reach the same level with them. The spectrum of the region C (bottom-left) is above the background spectrum. The spectrum of the region D is also above the background spectrum, there is an emission line between 1-2 kev in both background and data spectra. Instrumenral emission line around 8 keV is clearly seen in all spectra. All the spectra cover the energy range 0.30-10.00 keV.

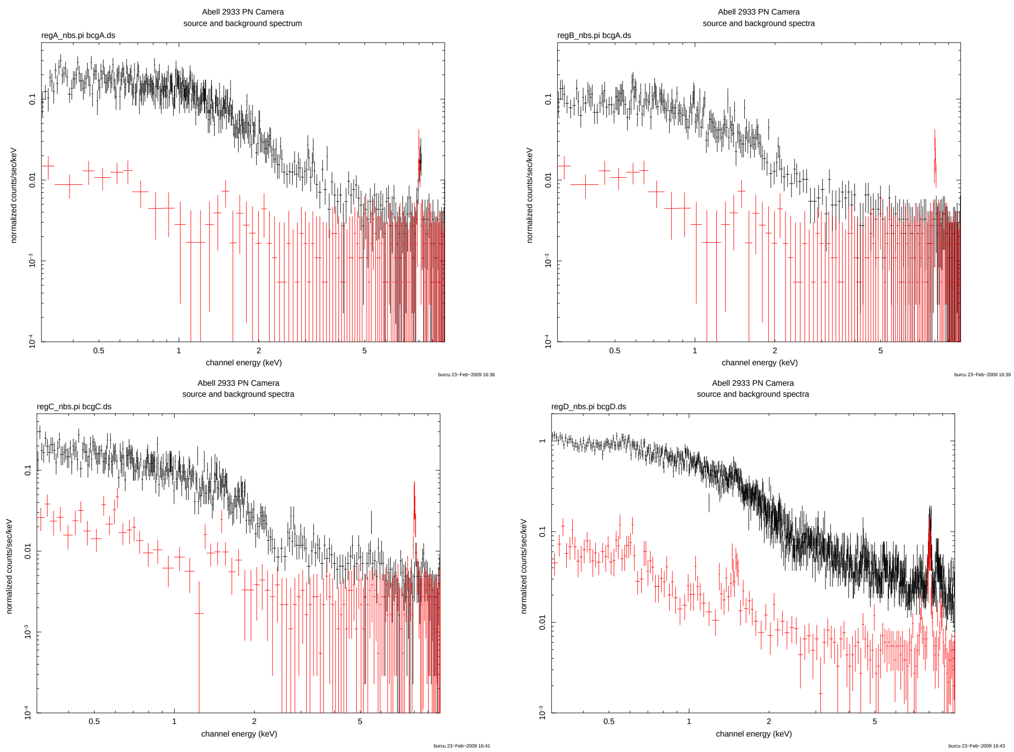

Figure 5.47. Abell 2933, selected regions (from left to right, top to bottom A, B, C, D) and their background spectra of the PN data

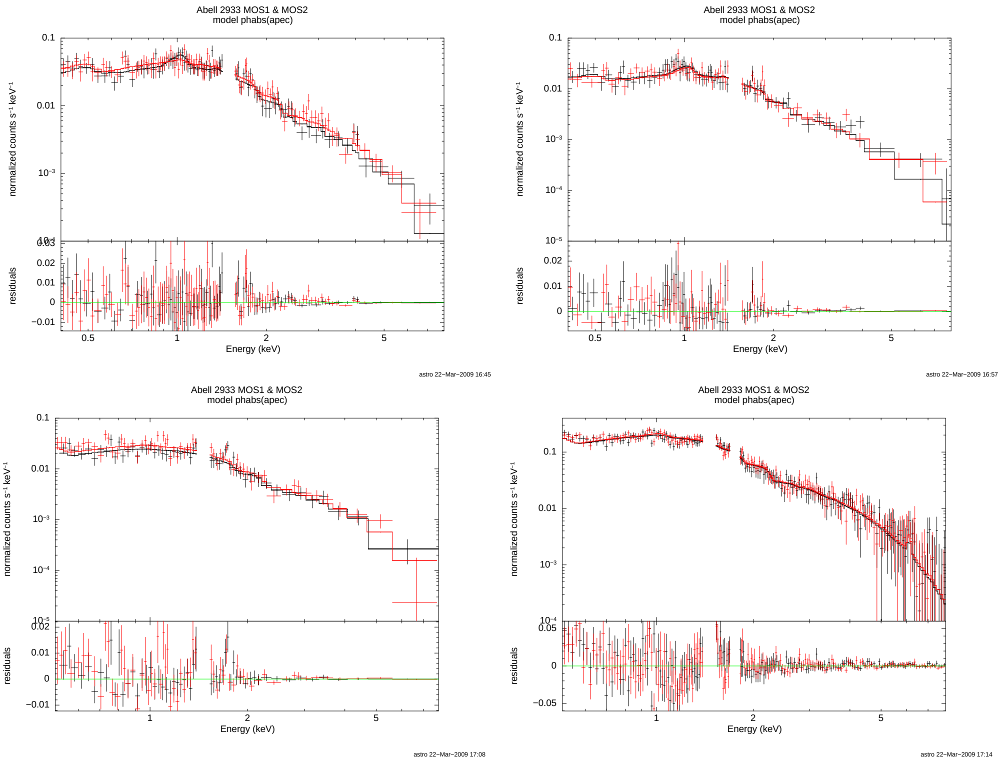

Figure 5.48. Abell 2933, MOS1 and MOS2 spectral fit (APEC) of the four regions (from left to right, top to bottom A, B, C, D)

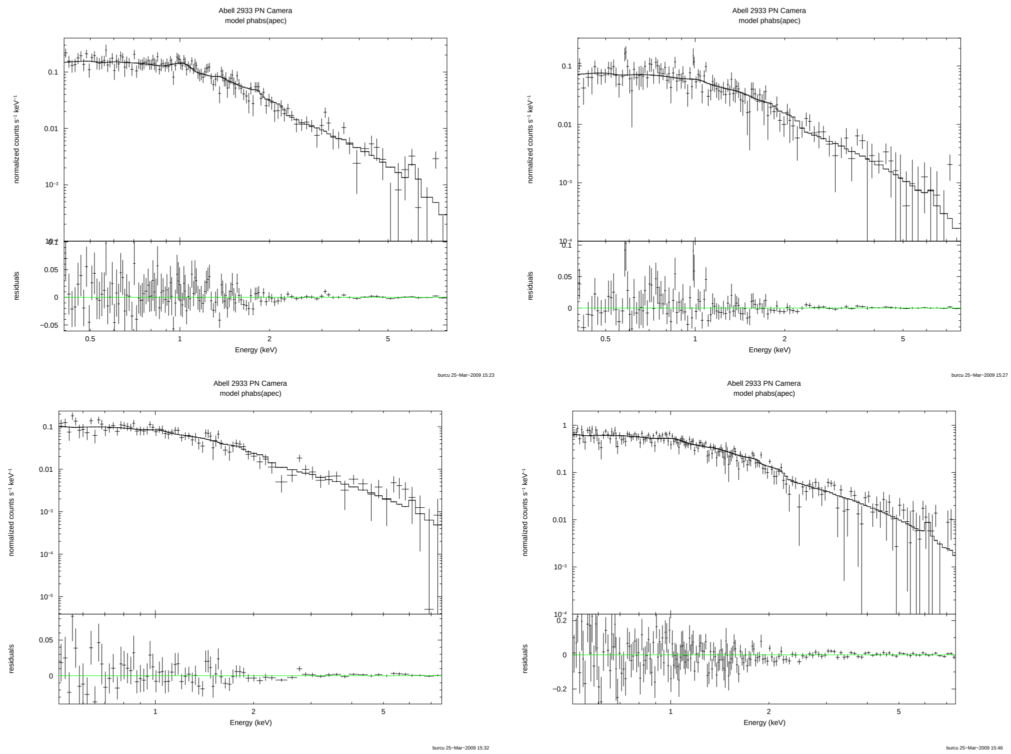

Figure 5.49. Abell 2933, PN spectral fit (APEC) of the four regions (from left to right, top to bottom A, B, C, D)

5.4. Abell 3888

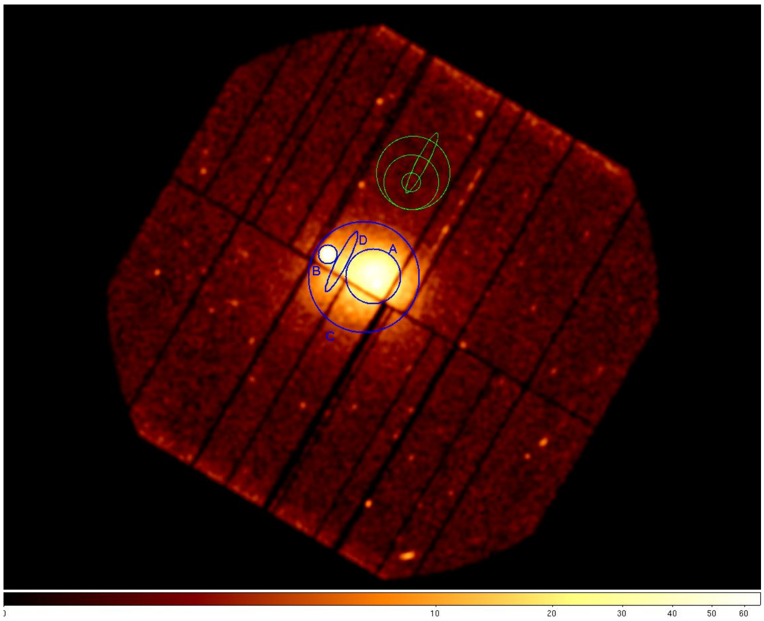

Figure 5.50. Abell 3888, raw image, regions chosen for spectral analysis on PN camera

On the cameras, regions A and B (Figures 5.50 and 5.51) cover 1.5 and 0,5 arc minutes, respectively.

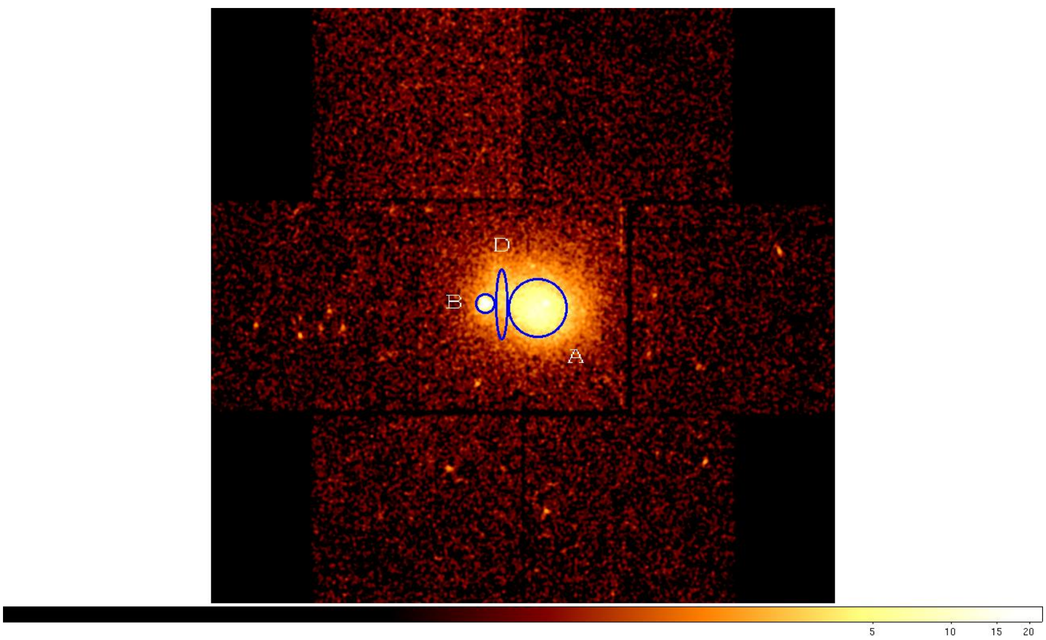

Figure 5.51. Abell 3888, raw image, regions chosen for spectral analysis on MOS2 camera

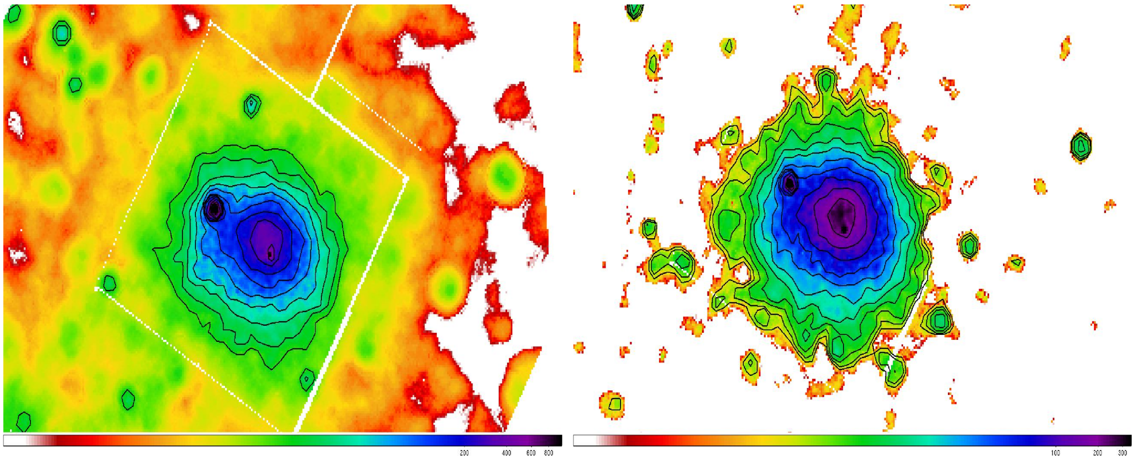

Figure 5.52. Abell 3888, background subtracted and exposure corrected image of MOS cameras in the (0.35-1.25) keV (left) and (2-8) keV (right)

In both soft and hard energy range images (Figure 4.52), the central part and the galaxy at the west side are seen. The connection of these two poles is more clear in the soft band range. The asymmetry of the structure is clear in both images.

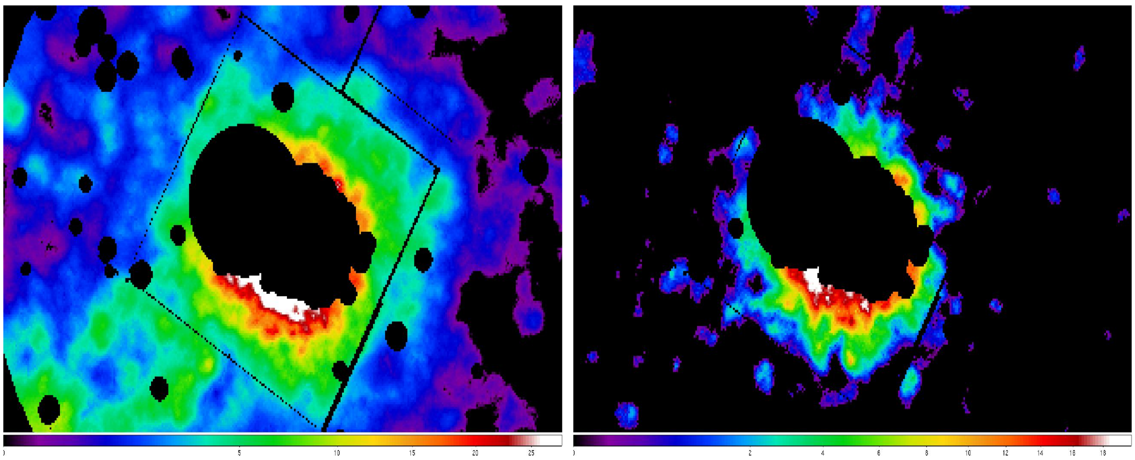

Figure 5.53. Abell 3888, background subtracted and exposure corrected image of MOS cameras with point sources are removed in the (0.35-1.25) keV (left) and (2-8) keV (right)

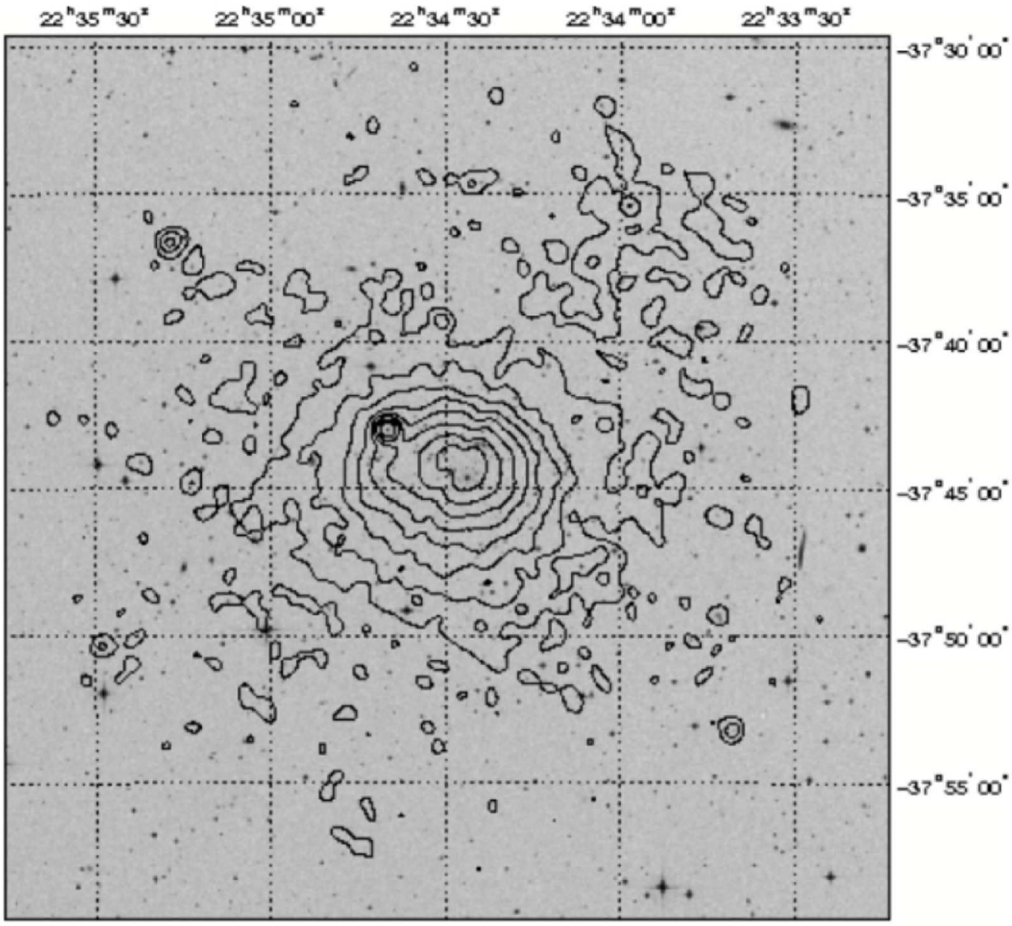

Figure 5.54. Abell 3888, X-ray contours over optical image

For each regions spectra of the two MOS cameras are fitted simultaneously. Spectral results are displayed in Table 4.7 as follows: For both MOS and PN cameras spectral fitting of the region A is done by using chi statistics. Spectrum from MOS1, MOS2 and PN are grouped in 25 and the spectral data counts are 17192, 10590 and 31558, respectively. Reduced chi-squared is 1.0076 for 465 degrees of freedom and 1.0357 for 596 degrres of freedom and the null hypothesis probabilities are 4.455397e-01 and 2.650454e-01, respectively. Difference between weihgted mean value of the temperature and temperature from MOS1 is 1.87 σ, from MOS2 0.08 σ and from PN 1 σ. Difference between weihgted mean value of the metal abundance and metal abundance from MOS1 is 0.5 σ, from MOS2 is 1 σ and from PN is 0.3 σ.

For both MOS and PN cameras spectral fitting of the region B are done by using chi statistics. Spectra from MOS1 and MOS2 are grouped in 15 and that of PN in

25. The spectral data counts are 1927, 1995 and 4188 respectively. For MOS and PN cameras, reduced chi-squared are 1.1601 for 183 degrees of freedom and 1.0178 for 139 degrees of freedom and the null hypothesis probability is 6.792611e-02 and 4.258081e-01, respectively. Difference between weihgted mean value of the temperature and temperature from MOS1 is 2.35 σ, from MOS2 is 1.46 σ and from PN is 0.73 σ. Difference between weihgted mean value of the metal abundance and metal abundance from MOS1 is 1.5 σ, from MOS2 is 1.25 σ and from PN is 0.75 σ.

For both MOS cameras and PN camera spectral fitting of the region C are done by using chi statistics. Spectrum from MOS1, MOS2 and PN are grouped in 15 and the spectral data counts are 6808, 6926 and 9916 respectively. For MOS and PN cameras, reduced chi-squared are 1.1054 for 435 degrees of freedom and 1.0630 for 428 degrees of freedom and the null hypothesis probability is 6.361086e-02 and 1.772502e-01, respectively. Difference between weihgted mean value of the temperature and temperature from MOS1 is 1.55 σ, from MOS2 is 2.3 σ and from PN is 0.6 σ. Difference between weihgted mean value of the metal abundance and metal abundance from MOS1 is 0.84 σ, from MOS2 is 1.32 σ and from PN is 0.37 σ.

For both MOS cameras and PN camera spectral fitting of the region D are done by using chi statistics. Spectrum from MOS1, MOS2 and PN are grouped in 25 and the spectral data counts are 1413, 1375 and 3158 respectively. For MOS and PN cameras, reduced chi-squared are 0.9473 for 90 degrees of freedom, 0.9066 for 109 degrees of freedom and the null hypothesis probabilities are 6.216780e-01 and 7.475805e-01, respectively. Difference between weihgted mean value of the temperature and temperature from MOS1 is 1.71 σ, from MOS2 is 0.64 σ and from PN is 0.36 σ. Difference between weihgted mean value of the metal abundance and metal abundance from MOS1 is 0.5 σ, from MOS2 is 1.25 σ and from PN is 1.5 σ.

Table 5.7. Abell 3888, spectral results of temperature and metal abundances for each regions and their errors

Regions	MOS1		MOS2		PN	
	temperature (keV) & err.	metal abundance (Z_o) & err.	temperature (keV) & err.	metal abundance (Z_o) & err.	temperature (keV) & err.	metal abundance (Z_o) & err.
A	10.05 -0.72/+0.72	0.25 -0.11/+0.11	9.29 -0.88/+0.93	0.22 -0.13/+0.17	8.93 -0.48/+0.53	0.30 -0.07/+0.07
B	4.69 -0.58/+0.64	0.18 -0.18/+0.20	3.70 -0.35/+0.38	0.29 -0.16/+0.18	4.27 -0.29/+0.41	0.21 -0.11/+0.11
C	7.23 -1.24/+1.91	0.56 -0.41/+0.47	7.78 -1.47/+2.07	0.65 -0.45/+0.54	5.76 -0.66/+0.79	0.33 -0.20/+0.22
D	8.84 -0.56/+0.57	0.26 -0.07/+0.07	8.18 -0.38/+0.38	0.19 -0.06/+0.06	8.26 -0.63/+0.65	0.30 -0.07/+0.06

Table 5.8. Abell 3888, weighted means and standart deviations of spectral results

Regions	weighted mean		standart deviation (σ)	
	temperature (keV)	metal abundance (Z_o)	temperature (keV)	metal abundance (Z_o)
A	9.32	0.28	0.39	0.06
B	4.08	0.24	0.26	0.04
C	6.17	0.40	0.69	0.19
D	8.36	0.24	0.28	0.04

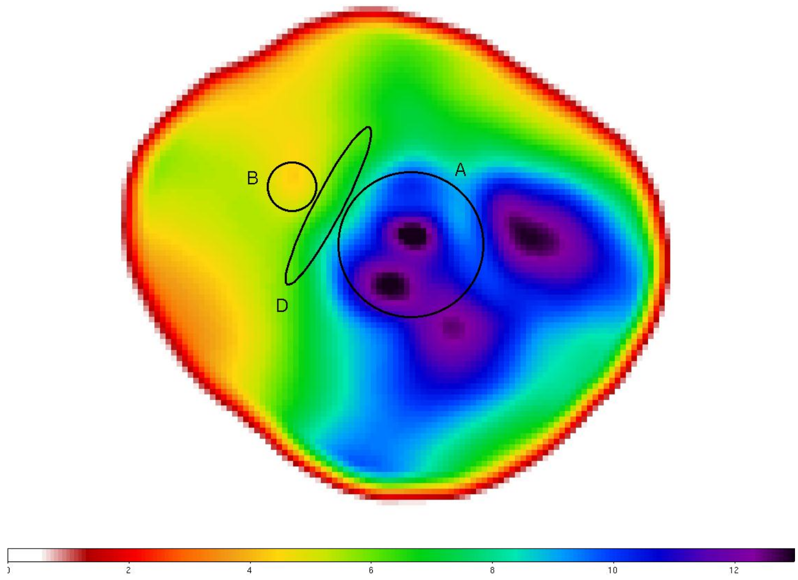

Figure 5.55. Abell 3888, temperature and metal maps extracted with XWSM. Color diagram is between 0-12 keV

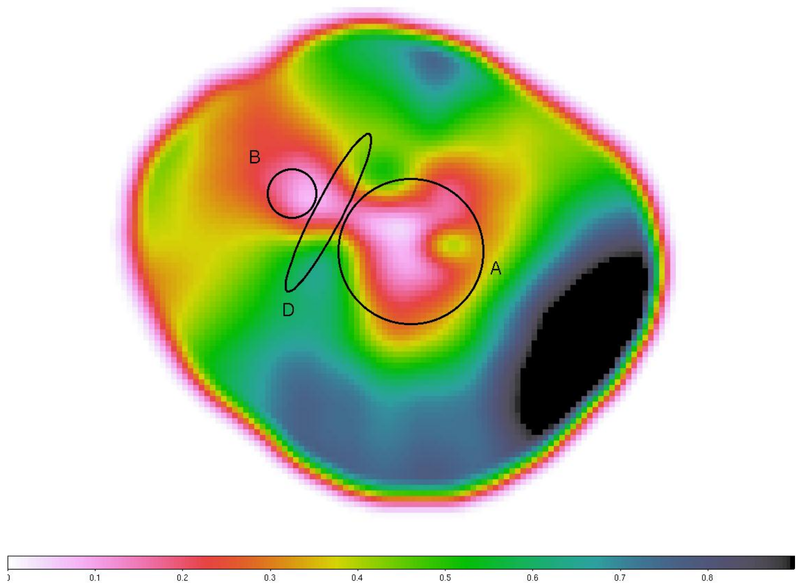

Figure 5.56. Abell 3888, metalicity map extracted with XWSM. Color diagram is between 0-0.8 Z_o

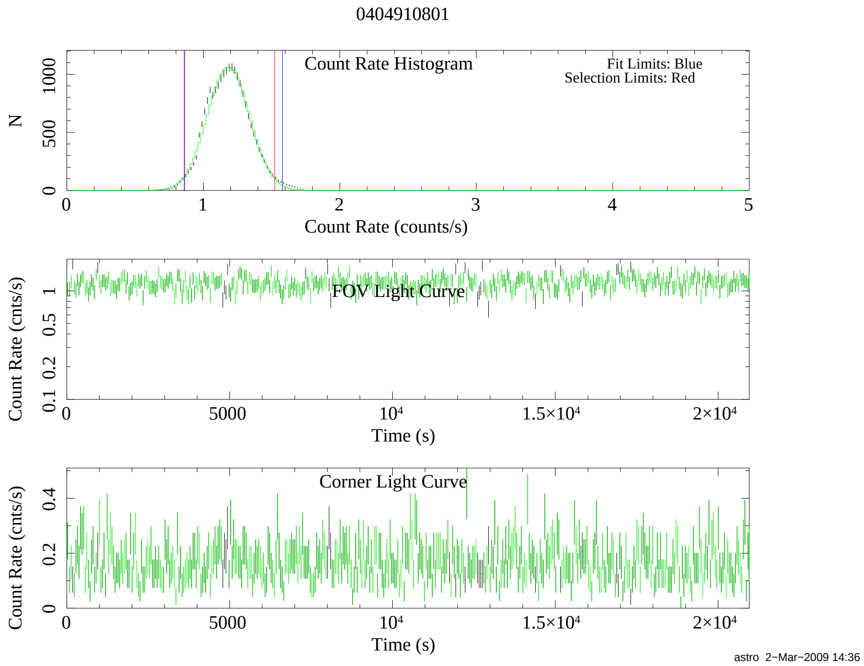

Figure 5.57. Abell 3888, temporal filtering resultsfor the MOS1 observation

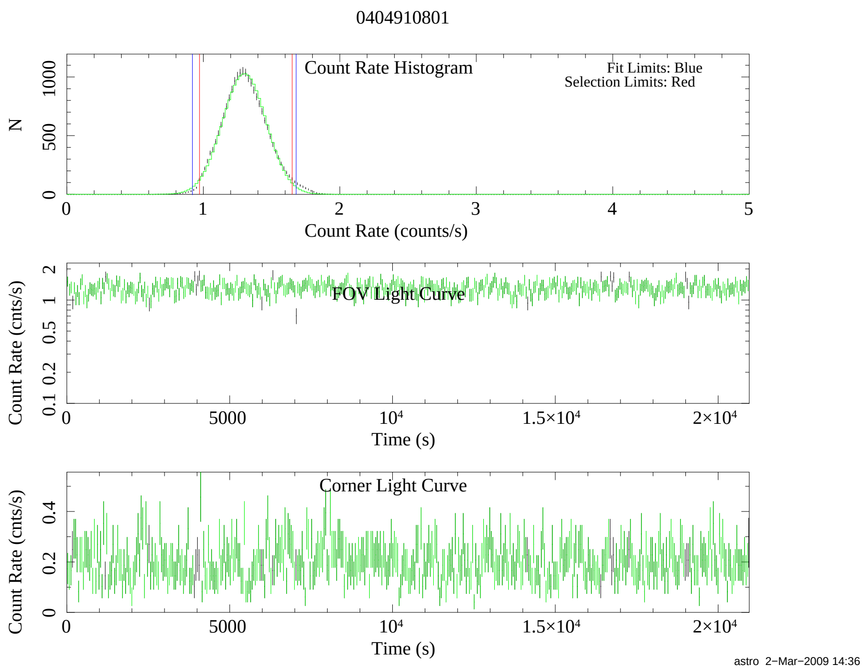

Figure 5.58. Abell 3888, temporal filtering resultsfor the MOS2 observation

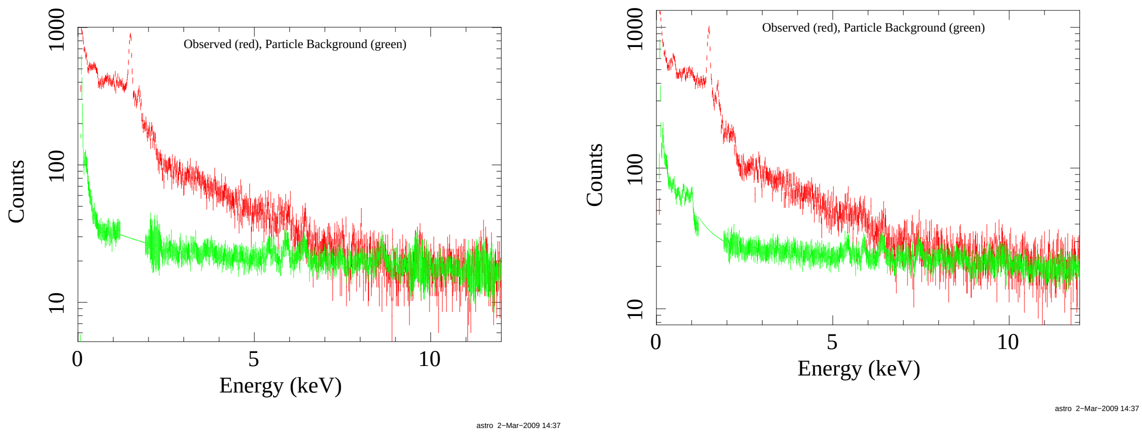

Figure 5.59. Abell 3888, observed spectrum (red) and the model background spectrum (green) of MOS1 and MOS2, respectively

Surface brighteness in soft energy band of the observed spectrum (0.35-1.25 keV) (Figure 4.60) is dominant compared to the hard enrgy band (0.20-8.00 keV) and continues until the near edge of the camera in a decreasing manner but its brightness level is very close to the model partical background spectra's brighteness. Hard energy band brightness continues until $\sim$ 6 arc minute in a decreasing manner while the model partical background spectra begins to increase from the $\sim$ 6 arc minute.

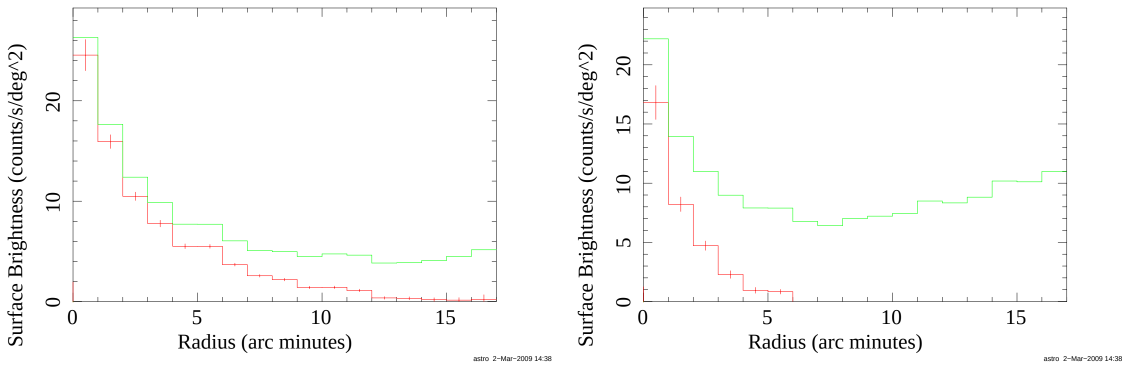

Figure 5.60. Abell 3888, radial profiles of the data for the (350-1250) eV and (200-8000) eV enrgy bands of the whole field of view

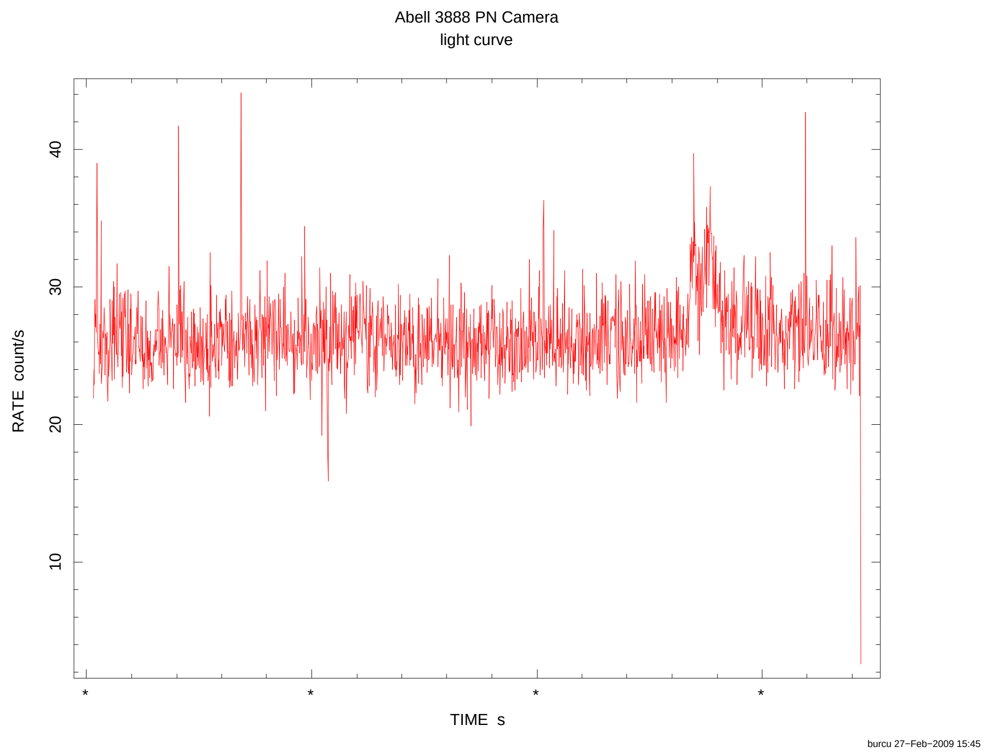

Figure 5.61. Abell 3888, unfiltered light curve of the PN data

We compared the selected background spectrum with the spectrum of the region which we want to make spectral anlysis (Figure 4.62). Spectrum of the region A is above its background spectrum. This spectrum covers the energy range 0.40-7.00 keV. (top-left of the figure). The spectrum of the region B and its background covers the energy range 0.50-7.00 keV and the region B spectrum is above the background. The spectrum of the region C (bottom-left) is above the background spectrum, there is only an emission line around 7 keV in background spectrum which reaches the data spectrum. The spectrum of the region D is also above the background spectrum.

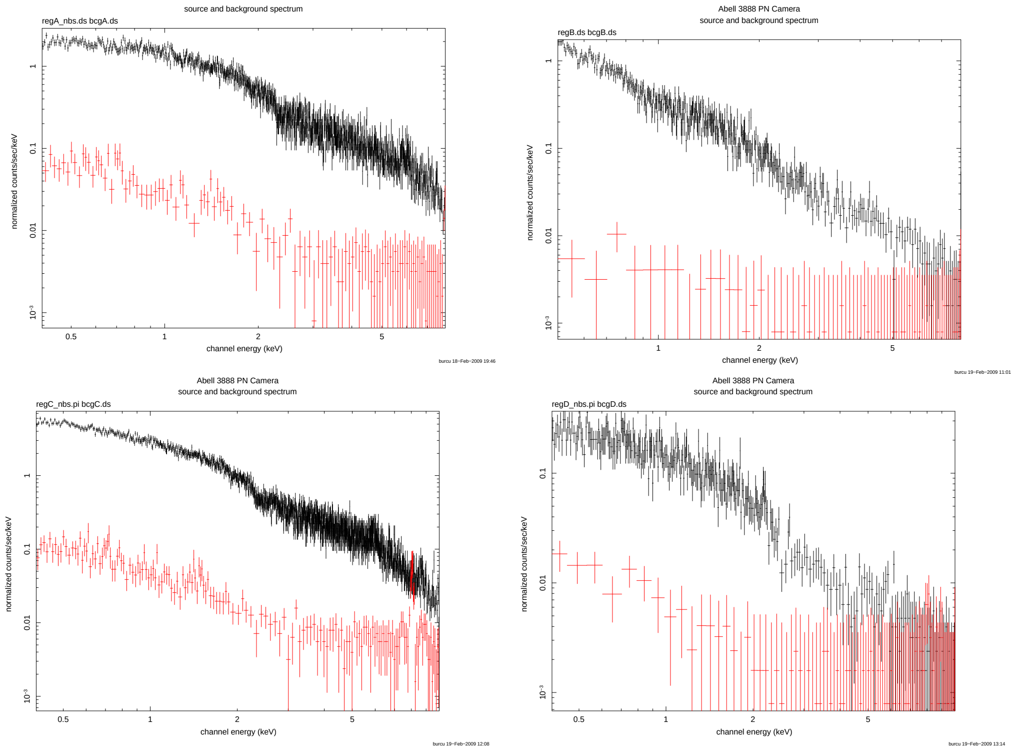

Figure 5.62. Abell 3888, selected regions (from left to right, top to bottom A, B, C, D) and their backgrounds spectra of the PN data

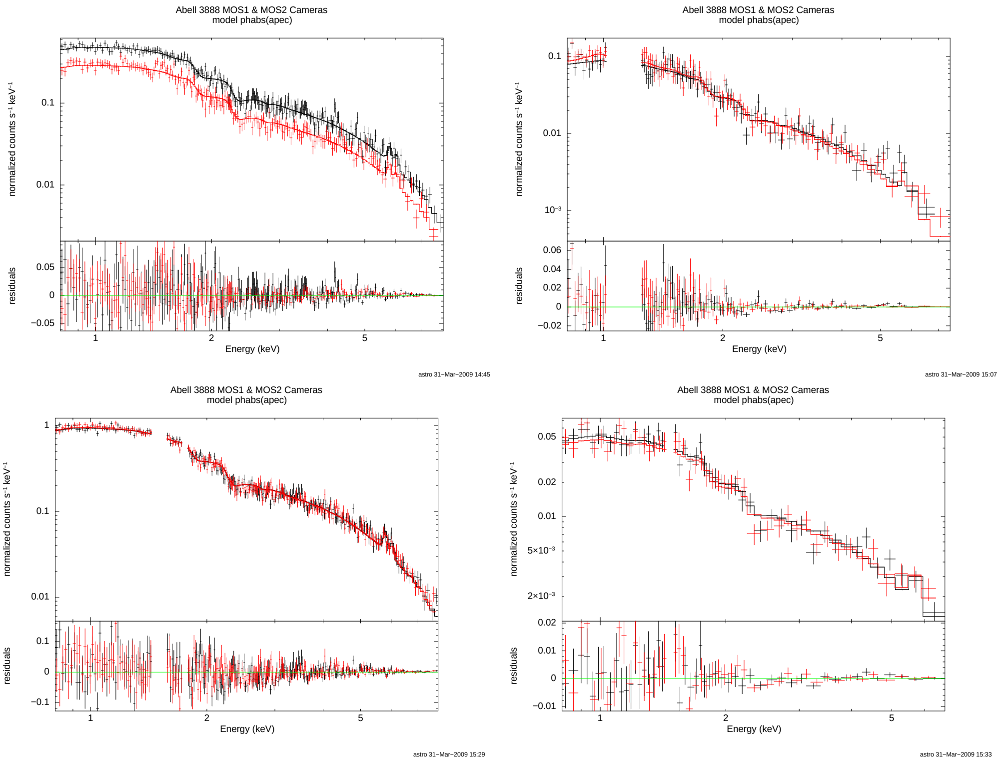

Figure 5.63. Abell 3888, MOS1 and MOS2 spectral fit (APEC) of the four regions (from left to right, top to bottom A, B, C, D)

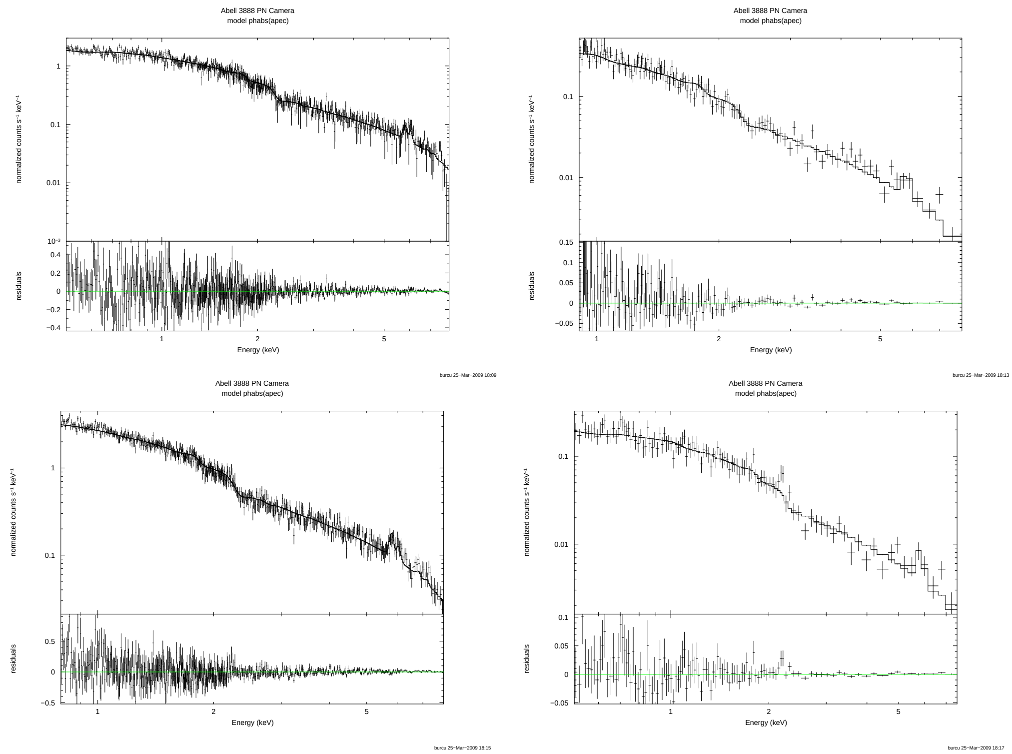

Figure 5.64. Abell 3888, PN spectral fit (APEC) of the four regions (from left to right, top to bottom A, B, C, D)

5.5. Abell 115

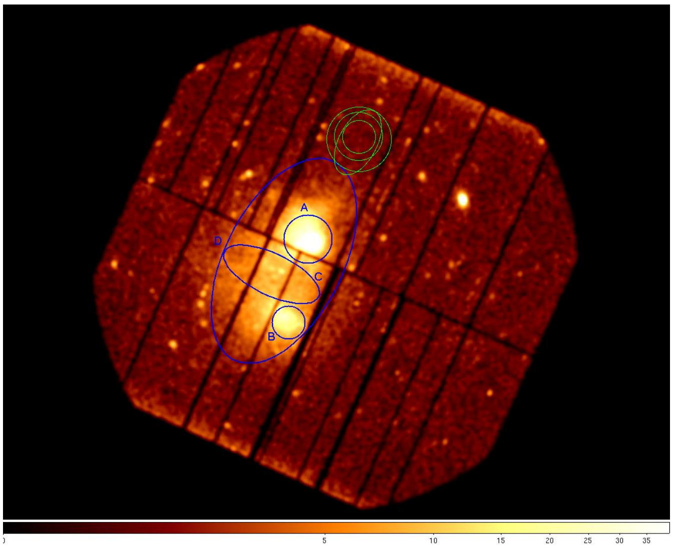

Figure 5.65. Abell 115, raw image, regions chosen to spectral analysis on PN camera

On the cameras, regions A and B (Figures 5.65 and 5.66) cover 1.5 and 1 arc minutes, respectively.

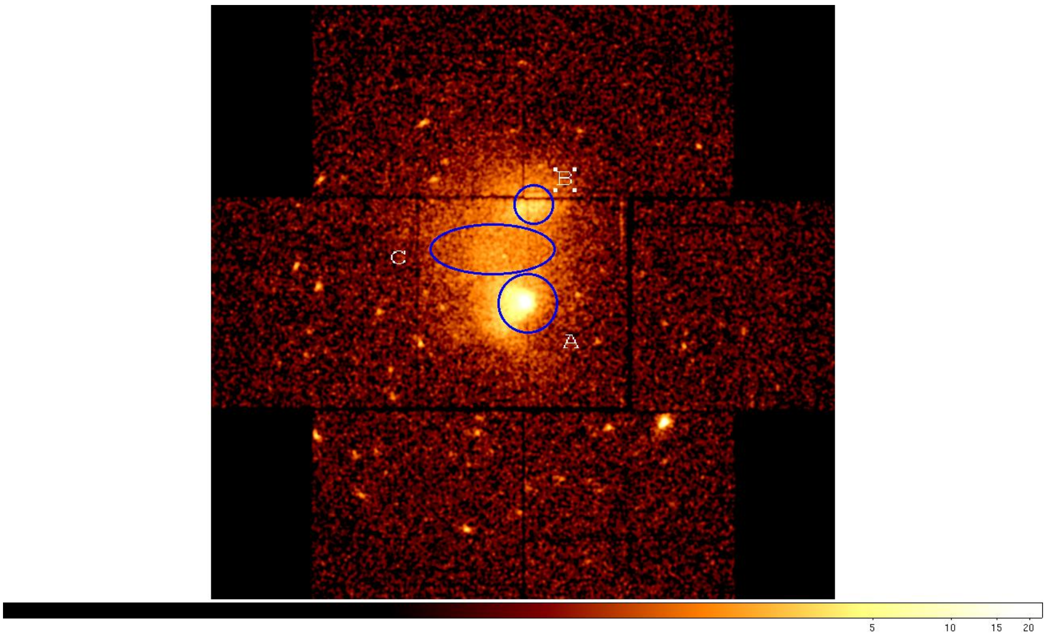

Figure 5.66. Abell 115, raw image, regions chosen to spectral analysis on MOS2 camera

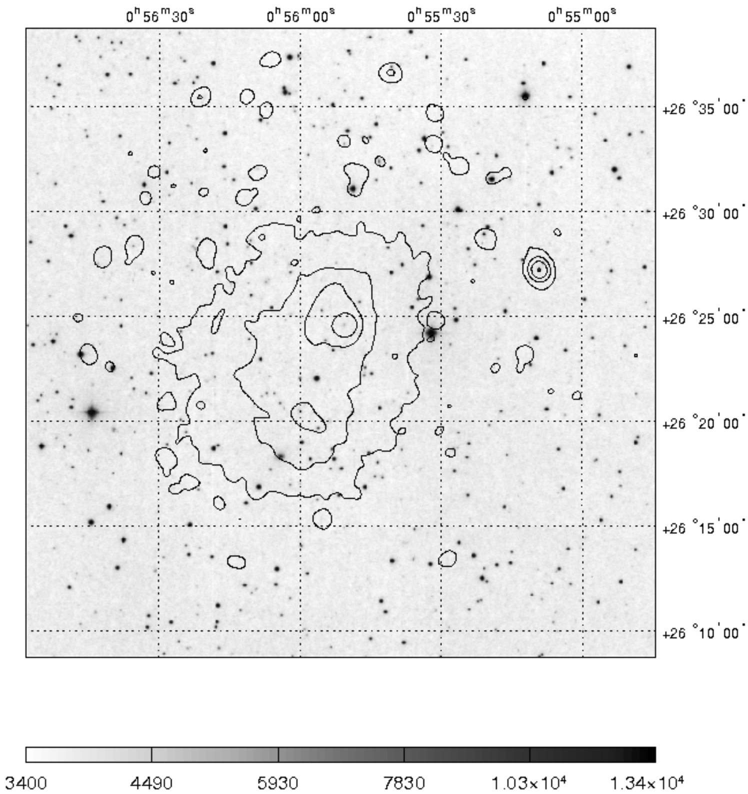

Figure 5.67. Abell 115, X-ray contours over optical image

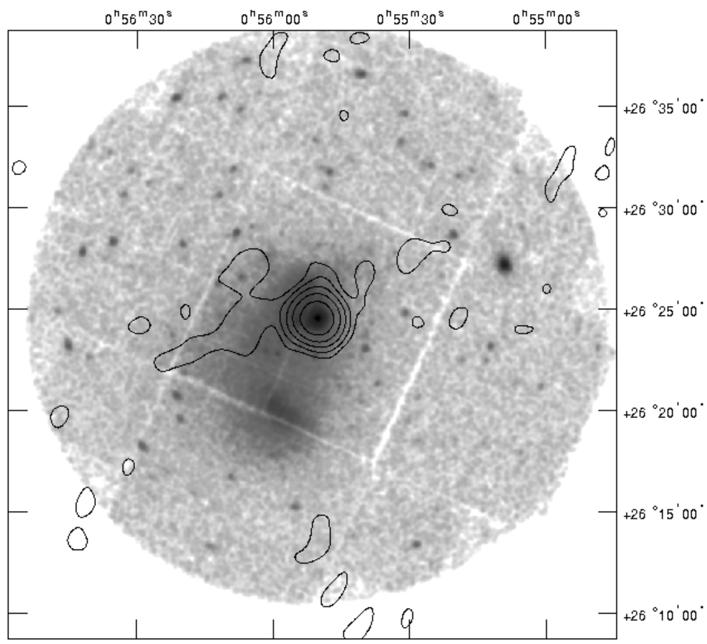

Figure 5.68. Abell 115, radio contours over X-ray image

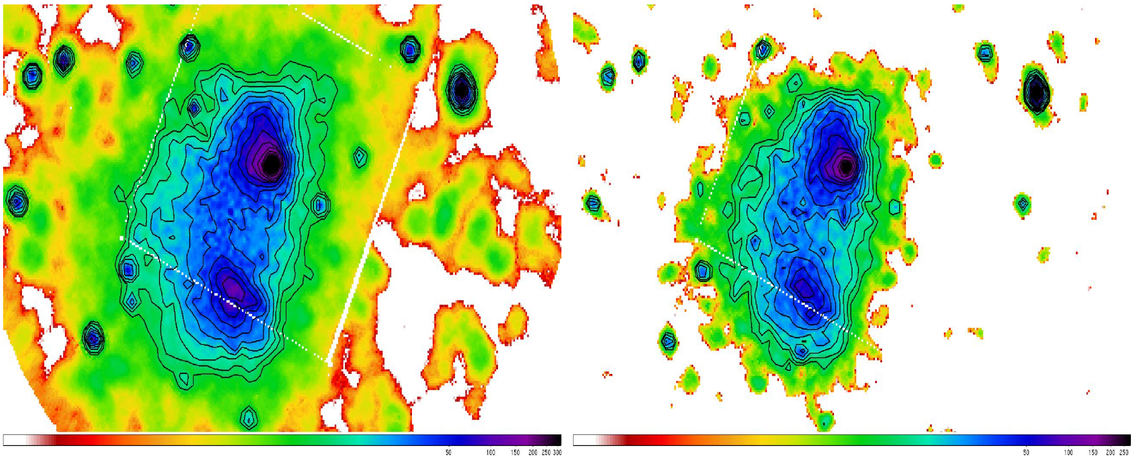

Figure 5.69. Abell 115, background subtracted and exposure corrected image of MOS cameras in the (0.35-1.25) keV (left) and (2-8) keV (right)

In both soft and hard energy range images (Figure 4.69), binary structure is clear. The interaction of the two poles are through the north-west part of the region between the subclumps..

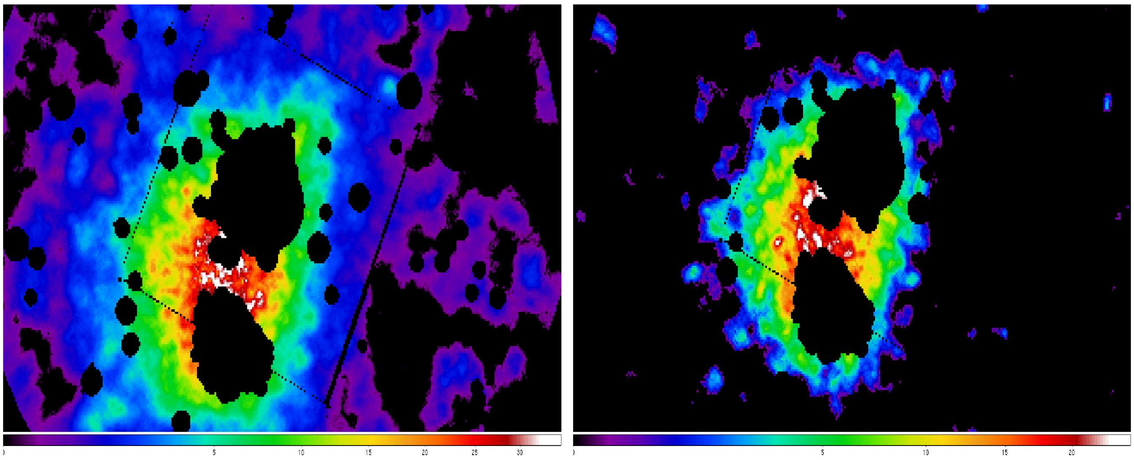

Figure 5.70. Abell 115, background subtracted and exposure corrected image of MOS cameras with point sources are removed in the (0.35-1.25) keV (left) and (2-8) keV (right)

For each regions spectra of the two MOS cameras are fitted simultaneously. Spectral results are displayed in Table 4.9 as follows: For both MOS cameras, spectral fitting of the region A is done by using chi statistics while in the case of PN camera C-statistic is used because with chi square statistics, null hypothesis probability is always smaller than 0.05. Spectra from MOS1 and MOS2 are grouped in 25 and the spectral data counts are 14283 and 13807, respectively. Reduced chi-squared is 1.0616 for 432 degrees of freedom and the null hypothesis probability is 1.814943e-01. Spectrum from PN camera is not grouped, spectral data counts is 19530 and goodness is 49.00 % of realizations are smaller than best fit statistics which is 1291.17 for region A. Difference between weihgted mean value of the temperature and temperature from MOS1 is 1.25 σ, from MOS2 is 2.5 σ and from PN is 0.75 σ. Difference between weihgted mean value of the metal abundance and metal abundance from MOS1 is 0.5 σ, from MOS2 is 1 σ and from PN is 0.25 σ.

For both MOS cameras and PN camera spectral fitting of the region B are done by using chi statistics. Spectra from MOS1, MOS2 and PN are grouped in 15 and the spectral data counts are 3588, 3005 and 5900 respectively. For MOS and PN cameras, reduced chi-squared are 0.90944 for 287 degrees of freedom and 0.92162 for 292 degrees of freedom and the null hypothesis probabilities are 8.624503e-01 and 8.277393e-01, respectively. Difference between weihgted mean value of the temperature and temperature from MOS1 is 1.7 σ, from MOS2 is 0.54 σ and from PN is 0.5 σ. Difference between weihgted mean value of the metal abundance and metal abundance from MOS1 is 0.38 σ, from MOS2 is 1 σ and from PN is 0.63 σ.

For both MOS cameras and PN camera spectral fitting of the region C are done by using chi statistics. Spectrum from MOS1, MOS2 and PN are grouped in 15 and the spectral data counts are 6808, 6926 and 9916 respectively. For MOS and PN cameras, reduced chi-squared are 1.1054 for 435 degrees of freedom and 1.0630 for 428 degrees of freedom and the null hypothesis probability is 6.361086e-02 and 1.772502e-01, respectively. Difference between weihgted mean value of the temperature and temperature from MOS1 is 0.26 σ, from MOS2 is 1.3 σ and from PN is 1.7 σ. Difference between weihgted mean value of the metal abundance and metal abundance from MOS1 is 0 σ, from MOS2 is 0.25 σ and from PN is 1.25 σ.

For both MOS cameras and PN camera spectral fitting of the region D are done by using chi statistics. Spectrum from MOS1, MOS2 and PN are grouped in 25 and 65 and the spectral data counts are 40317, 39896 and 54547 respectively. For MOS and PN cameras, reduced chi-squared are 1.0353 for 717 degrees of freedom and 1.1086 for 475 degrees of freedom and the null hypothesis probability is 2.490671e-01 and 5.076908e-02, respectively. Difference between weihgted mean value of the temperature and temperature from MOS1 is 0.6 σ, from MOS2 is 1.75 σ and from PN is 2.25 σ. Difference between weihgted mean value of the metal abundance and metal abundance from MOS1 is 0.3 σ, from MOS2 is 0 σ and from PN is 0.3 σ.

Table 5.9. Abell 115, spectral results of temperature and metal abundances for each regions and their errors

Regions	MOS1		MOS2		PN	
	temperature (keV) & err.	metal abundance (Z_o) & err.	temperature (keV) & err.	metal abundance (Z_o) & err.	temperature (keV) & err.	metal abundance (Z_o) & err.
A	4.66 -0.22/+0.22	0.26 -0.07/+0.07	4.21 -0.16/+0.23	0.32 -0.07/+0.07	4.60 -0.20/+0.20	0.27 -0.05/+0.03
B	5.04 -0.47/+0.53	0.26 -0.15/+0.17	4.45 -0.42/+0.51	0.15 -0.13/+0.13	4.46 -0.36/+0.36	0.28 -0.11/0.11
C	6.71 -0.54/+0.82	0.21 -0.13/+0.13	6.09 -0.52/+0.53	0.20 -0.11/+0.12	7.69 -0.78/+0.80	0.26 -0.11/+0.12
D	5.59 -0.23/+0.22	0.22 -0.04/+0.04	5.30 -0.16/+0.18	0.23 -0.05/+0.05	5.78 -0.27/+0.27	0.24 -0.05/+0.05

Table 5.10. Abell 115, weighted means and standart deviations of spectral results

Regions	weighted mean		standart deviation (σ)	
	temperature (keV)	metal abundance (Z_o)	temperature (keV)	metal abundance (Z_o)
A	4.51	0.28	0.12	0.04
B	4.59	0.23	0.26	0.08
C	6.61	0.21	0.39	0.04
D	5.51	0.23	0.12	0.03

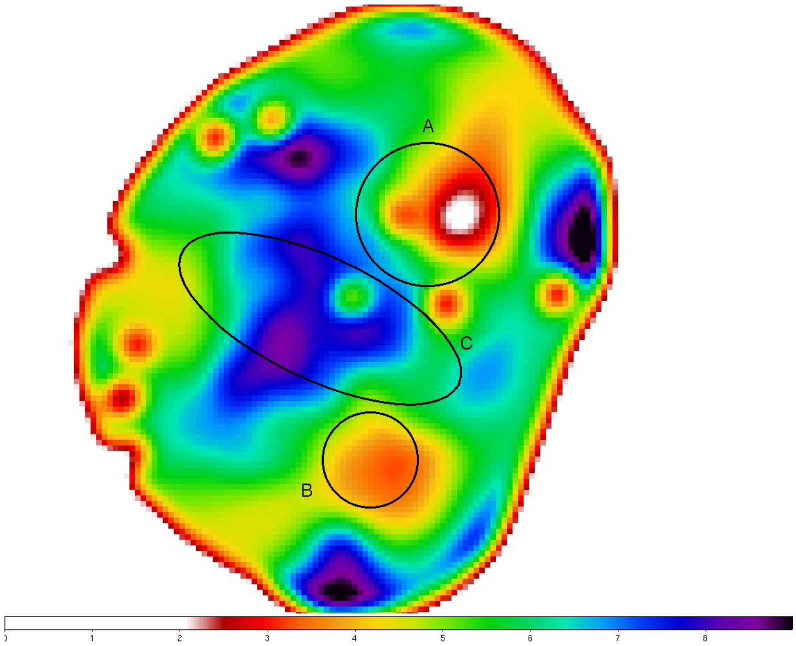

Figure 5.71. Abell 115, temperature map extracted with XWSM. Color diagram is between 0-8 keV

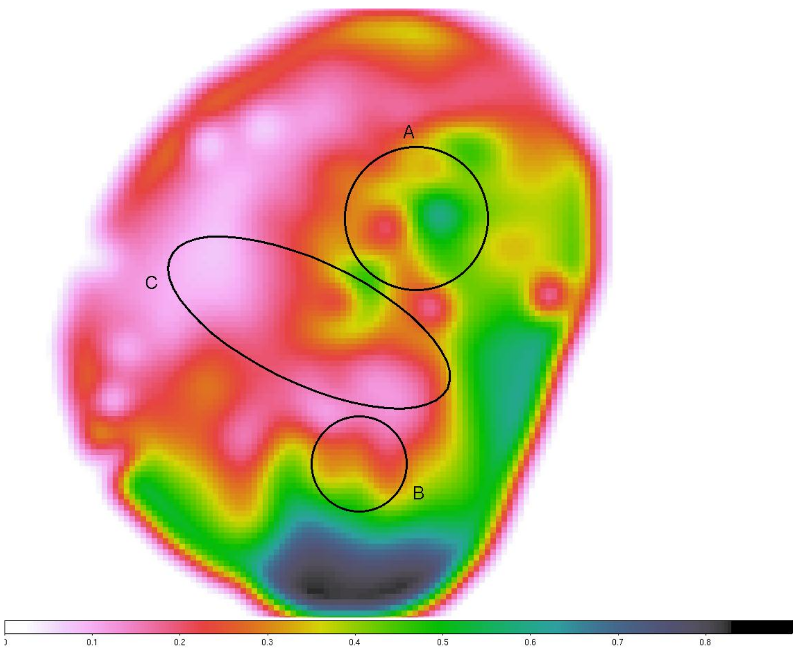

Figure 5.72. Abell 115, metalicity map extracted with XWSM. Color diagram is between 0-0.8 Z_o

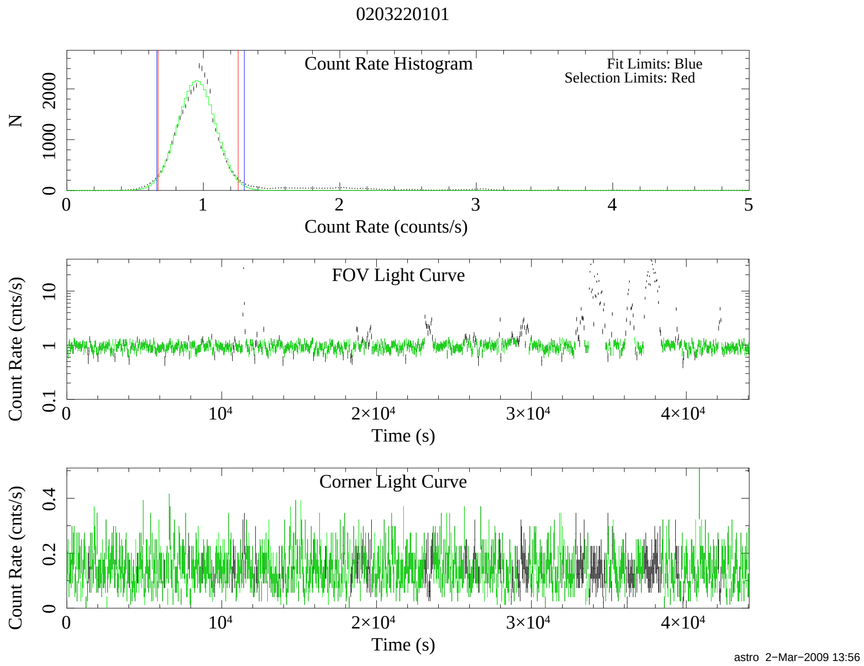

Figure 5.73. Abell 115, temporal filtering results for the MOS1 observation

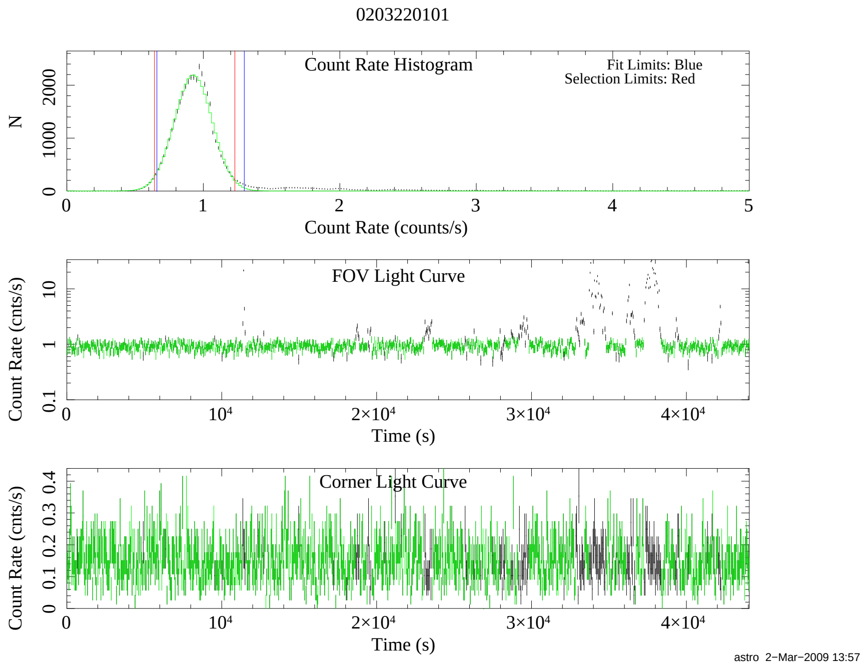

Figure 5.74. Abell 115, temporal filtering results for the MOS2 observation

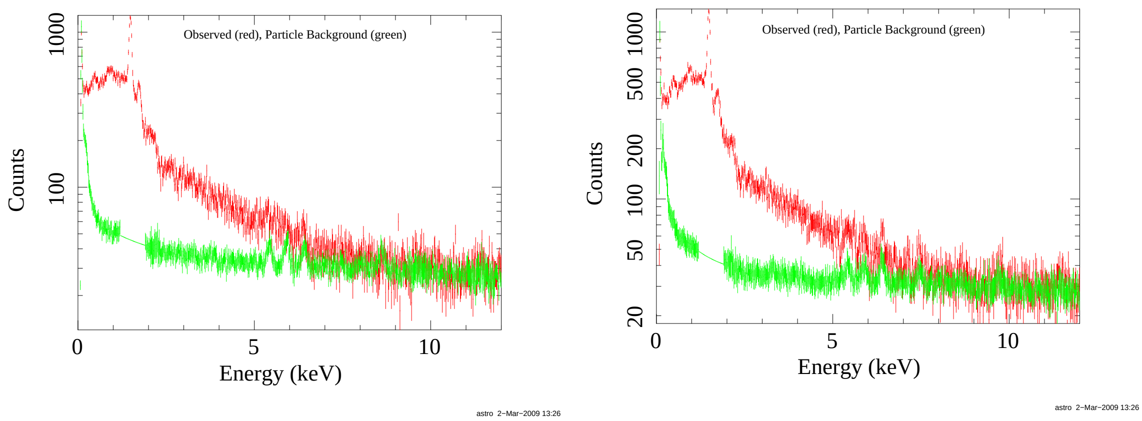

Figure 5.75. Abell 115, observed spectrum and the model partical background spectrum of MOS1 and MOS2, respectively

Surface brighteness in soft energy band of the observed spectrum (0.35-1.25 keV) (Figure 4.76) is dominant than that of the hard enrgy band (0.20-8.00 keV) and continues until the near edge of the camera in a decreasing manner. Approximately between the radius 0-5 arc minutes, surface brighteness levels of the observed and model partical background spectra are very close to each other while in the hard energy band surface brighteness level of the observed spectrum is significantly lower than one of the model partical background which begins to increase after the radius $\sim$ 8 arc minute.

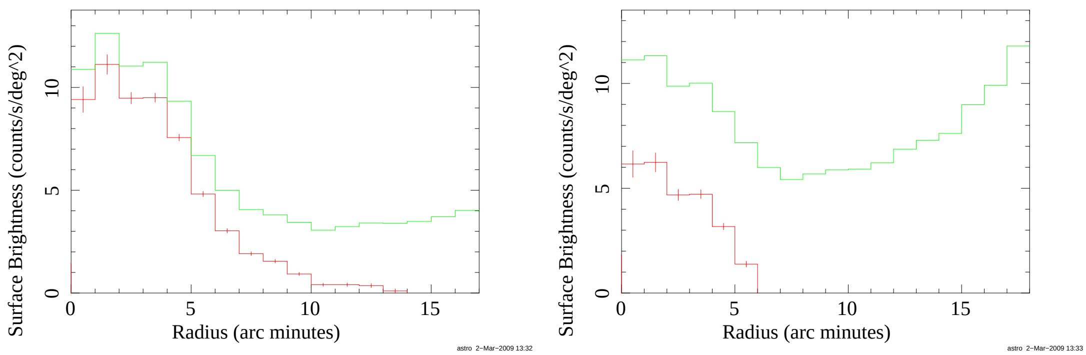

Figure 5.76. Abell 115, radial profiles of the data for the (350-1250) eV and (200-8000) eV energy bands of the whole field of view

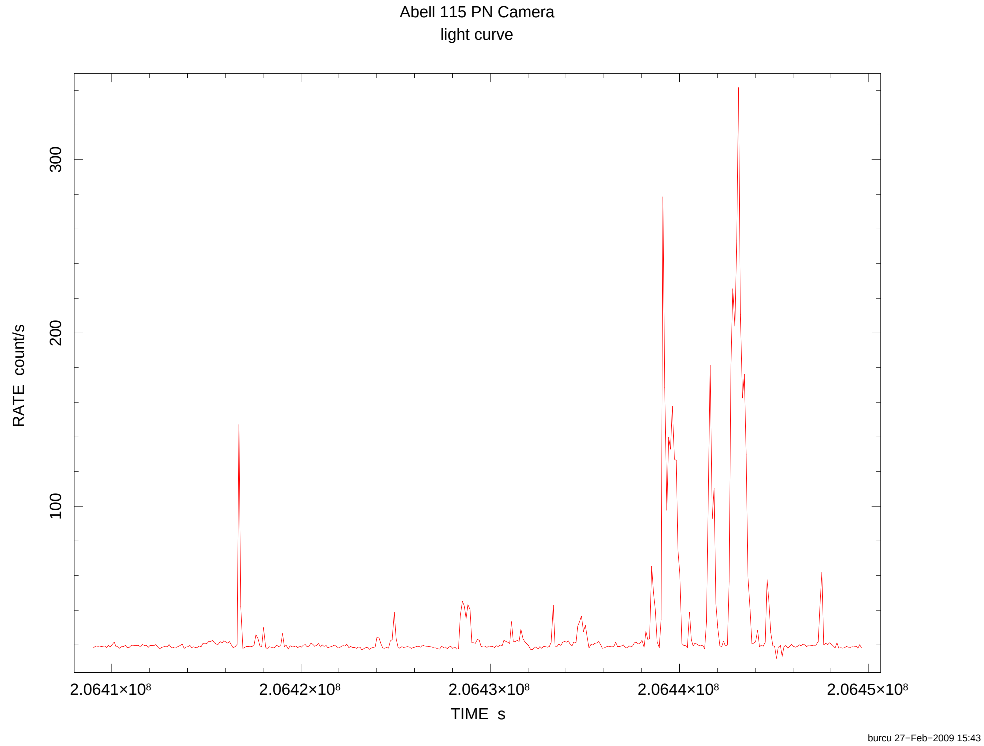

Figure 5.77. Abell 115, unfiltered light curve of the PN data.

We compared the selected background spectrum with the spectrum of the region which we want to make spectral anlysis (Figure 4.78). Spectrum of the region A is above its background spectrum. This spectrum covers the energy range 0.30-8.00 keV. (top-left of the figure). The spectrum of the region B and its background covers the energy range 0.30-10.00 keV and approximatley from 7 keV, the background level is the same with that of the regin B. The same structure is seen in the spectrum of the region C (bottom-left). The spectrum also covers the energy range 0.30-10.00 keV. In most of the energy range the background level is lower than the spectrum of the region D. In all four spectra emission lines of the PN camera are clearly visibles, especially the line around the 8.00 keV.

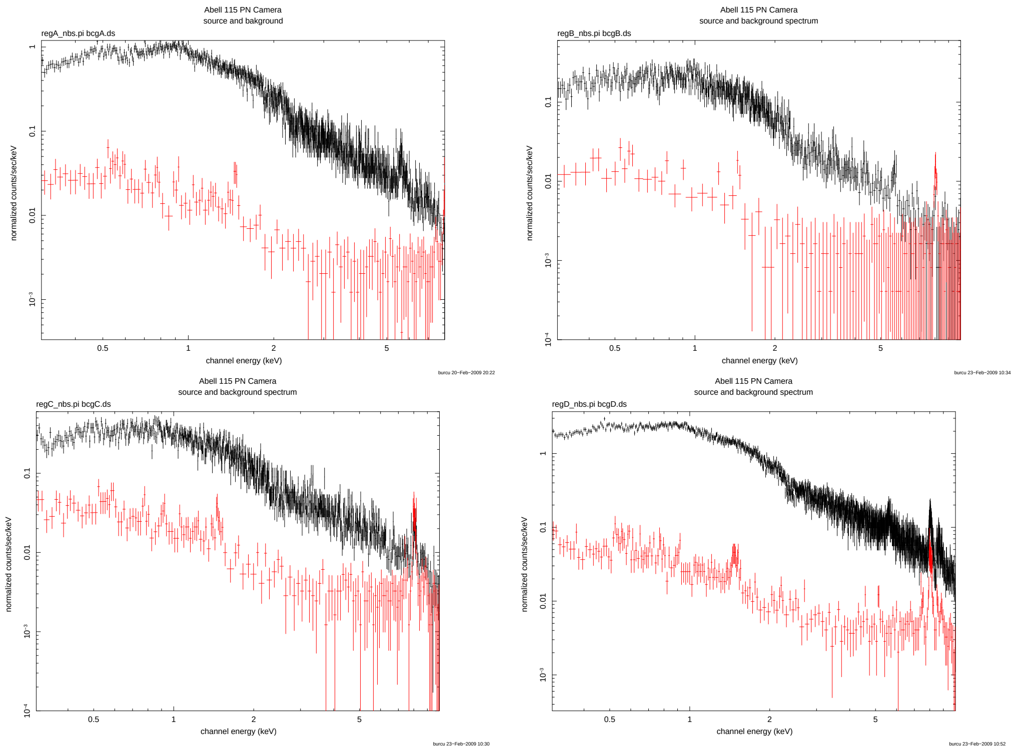

Figure 5.78. Abell 115, selected regions (from left to right, top to bottom A, B, C, D) and their background spectra of the PN data

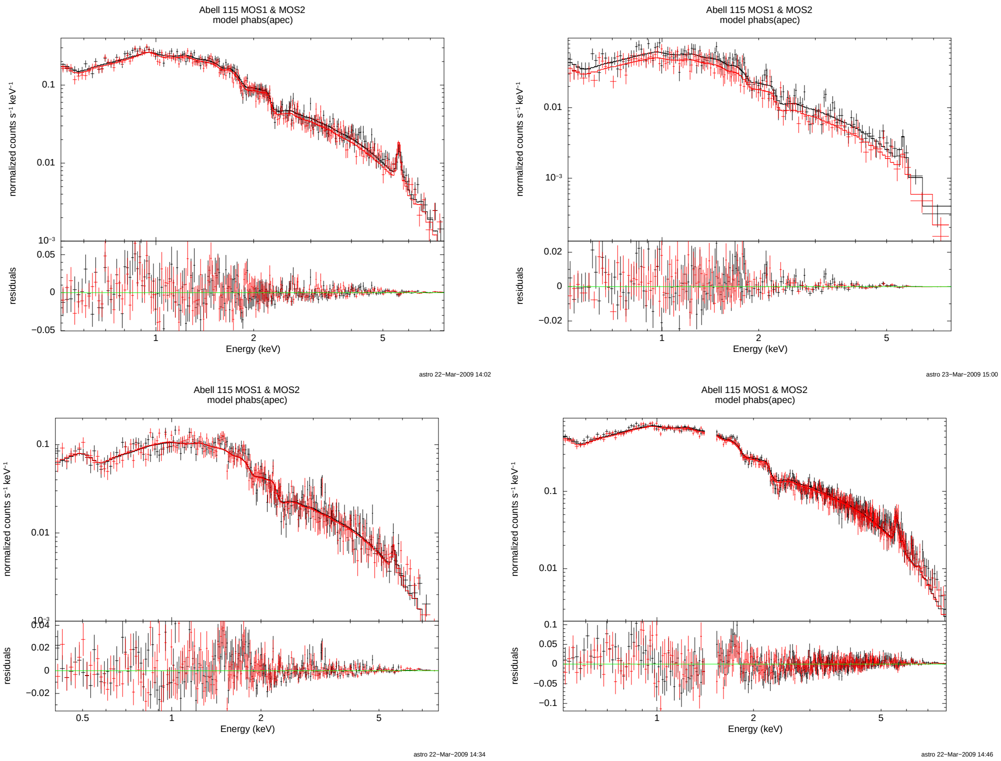

Figure 5.79. Abell 115, MOS1 and MOS2 spectral fit (APEC) of the four regions (from left to right, top to bottom A, B, C, D)

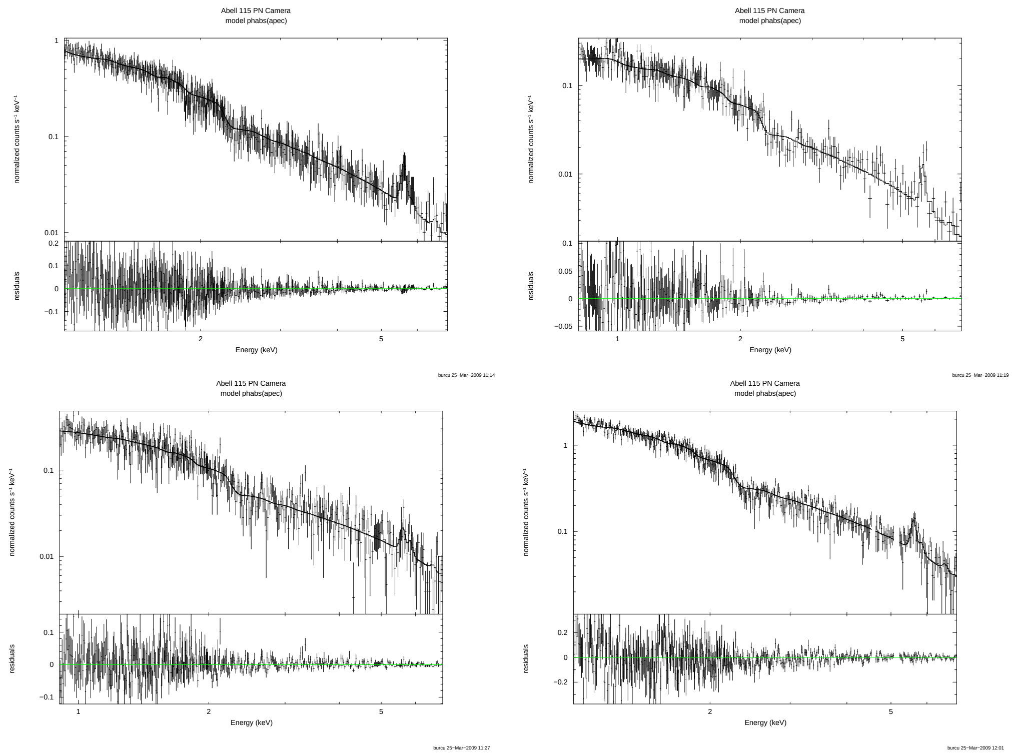

Figure 5.80. Abell 115, PN spectral fit (APEC) of the four regions (from left to right, top to bottom A, B, C, D)

6. DISCUSSION

In this work the following results are obtained:

Abell 3705; our spectral results (see Table 4.1 & 4.2) and temperature map (Figure 4.6) both show that region C is not hotter (1.74 +- 0.38 keV) than regions A (2.89 +- 0.19 keV) and B (1.14+- 0.12 keV). We can say that the ICM gas has a uniform temperature distribution at large scale. There is no shocked hot gas in between the regions A and B, which is probably the epoch we observe is not their first encounter. The hot gas ($\sim 2.89^{+0.19}_{-0.19}$ keV) at the region A is elongated at the direction of region B, perpendicular to the main binary structure. From Figure 4.3, it can be seen that regions A and D are apparently physically connected although, raw images of region D is much fainter than region B. The metal abundance values for regions A, B ,C and E (overall region) are found to be rather low (see Table 4.1) however, the region D (faint region connected to the region A) has a metal abundance of $0.51^{+0.21}_{-0.21}$ Z_o. Our metallicity map results obtained for region D by XWSM is in conflict with the results obtained from the spectral analysis of the same region, this maybe due to the poor statistics since this region is rather faint compared to the other regions. If it is not a chance location at the line of sight, this high metal region can be head of the recent merger sub-group. The elongated gas has the direction of the entrance to the ICM. As a result, Abell 3705 does not show any evidence of a major merger effect. In fact, the optical studies by Zabludoff et al. 2009 [60] also support our findings. Our X-ray studies are in very good agreement of early X-ray studies of Abell 3705 i.e. [60].

Abell 2440; temperature results (see Table 4.3 & 4.4) do not show any significant temperature diffrences between the regions A, B and C. However, according to the temperature map obtained by XWSM (see Figure 4.25), regions A, B and C do not show a uniform temperature distribution with region C (especially its closer part to region A) being hotter than regions A and B. Metal abundances from spectral analysis of regions A ($0.57^{+0.1}_{-0.1}$ Z_o) and B ($0.62^{+0.14}_{-0.14}$ Z_o) are above the average cluster metallicity which is $\sim$ 0.3 Z_o while that of region C values are in good ($0.2^{+0.08}_{-0.08}$ Z_o) is close to the average value [1]. Temperature of the region D is kT=$4.18^{+0.08}_{-0.08}$ keV which is in a reasonable agreement with the result of David et al. [72] Optical observations by Mohr et al. 1996 [61] implies that Abell 2440 is dynamically young and it is classified as a pre-merging cluster by Maurogordato, S. 2006 [75]. X-ray images obtained in this work (see Figure 4.17), with elongation between the two substructures also supports the asymmetry between these regions as mentioned by Mohr et al. 1996 [61], suggesting that there are ongoing gas interactions between them.

Abell 2933; according to our spectral results (see Table 4.5 & 4.6) and especially to the temperature map (see Figure 4.40), region C is hotter than the regions A and B. Metal abundances obtained from spectral analysis are below the average cluster metallicity [1], while those from metallicity map (see Figure 4.41) are at about the average value. X-ray images (see Figure 4.37), especially soft band image, display the connection and elongation between the two poles. Our temperature and image analysis are in a good agreement with Maurogordato, S. 2006 [75] suggesting that Abell 2933 is in a pre-merger phase.

Abell 3888; our X- ray images of the Abell 3888 do not show bimodal structures as clear as other four cluster samples analysed in this work. The raw X- ray images display a spherical structure with a bright source near the center overlapped with a galaxy (see Figures 4.50, 4.51 and 4.54). According to the spectral results (see Table 4.7 & 4.8), the highest temperature value belongs to region A, kT=$9.32^{+0.39}_{-0.39}$ keV which is the central region while the lowest temperature belongs to region B, kT=$4.08^{+0.26}_{-0.26}$ keV. Spectral analysis of the region B is more difficult because of the poor statistics and there is a possibility that the spectral model (APEC) used to fit the data is either inadequate or needs additional components since this region defines mostly a galaxy rather than ICM. Our temperature and metal abundance values obtained from spectral analysis for region D, kT=$8.36^{+0.28}_{-0.28}$ keV and ($0.24^{0.04}_{0.04}$) Z_o, is in a good agreement with XMM-Newton results [78] of kT=$8.8^{+0.65}_{-0.65}$ keV and $\sim$0.2 Z_o. Considering the general dynamics, both spectral results and the temperature map (Figure 4.55) show a temperature distribution which decreases from region A to region B. The X-ray images (Figure 4.52) display an asymmetric elongation between the center and region

B. Multiple galaxy structure as mentioned by Struble & Ftaclas 1994 [66] ,non-uniform temperature distribution of the ICM (Table 4.7 and Figure 4.55) with X- ray images (Figure 4.52) indicate an ongoing activity in the core region of Abell 3888 as in previous observations suggested [69] a phase of merging galaxy groups.

Abell 115; our spectral results (see Table 4.9 & 4.10) and temperature map (see Figure 4.71) obtained in this work show that region C between the two poles is significantly hotter than these pole regions. Our temperature values are in good agreement with the measurement done by ASCA [79] and Chandra [67] except region A which has lower temperature value of kT= $kT = 3.43^{+0.09}_{0.09}$ keV in Chandra observations. Our X-ray analysis and the previous observations indicate a clear merging characteristics, however, the reason of hot ICM between the two poles is not only due to the merging activities there could be also a strong radio jet effect and according to the previous studies there is no direct evidence for shock heating of the ICM, a possible explanation can be the fact that the ICM is heated by viscous dissipation, see i.e. [67], [80].

7. CONCLUSION

In this work, five clusters of galaxies are analysed by using XMM-Newton archived data. Three of them, Abell 2440, Abell 2933 and Abell 115 are found to be in ongoing merging phase, being in a very good agreement with the early studies of them as mentioned above. Abell 3888, is found to be in a dynamic state with a possible merging of galaxy groups being in a very good agreement with its early studies. Only Abell 3705 is found not to show any merging activity, comparing the only very limited work done for it so far, our results show very good agreement with these very limited study. Our studies are consantrated on individual portions (regions) extensively, therefore, the X-ray analyses done in this work for their X-ray spectra and temperature maps cover these individual portions, one by one, extensively. In this study, Abell 3705, Abell 2440, Abell 2933 and Abell 3888 are studied in a rather extensive way compared to the early work done on these clusters for the first time. The temperature and metal abundances of these clusters of galaxies are studied by introducing new methodes and softwares (XMM-ESAS and XWSM) developed, recently. Further studies of these clusters of galaxies are required for the future with more sophisticated X-ray satellites and with longer observational duration.

REFERENCES

1. Böhringer, H., “Clusters of Galaxies ”, Trumper, J. E. and Hasinger, G. (editors) in *The Universe in X-Rays*, pp. 395-430, A & A Library, Springer 2008.

2. Anders, E. and N. Grevesse, “Abundances of the elements - Meteoritic and Solar ”, *Geochimica et Cosmochimica Acta*, Vol. 53, pp. 197-214, January 1989.

3. Sarazin, C. L., “X-Ray Emission From Clusters Of Galaxies ”, Cambridge Astrophysics Series, Cambridge University Press, Cambridge, 1988.

4. Biviano, A., “From Messier To Abell: 200 Years Of Science With Galaxy Clusters ”, *Constructing the Universe with Clusters of Galaxies*, Durret, F. and Gerbal, D. (editors), IAP 2000 Meeting, Paris, 2000.

5. Feretti, L., Gioia, I. M. and Giovannini, G. (editors), *Merging Processes In Galaxy Clusters*, Ast. & Space Sci. Library, Kluwer, 2002.

6. Zwicky, F., “On the Masses of Nebulae and of Clusters of Nebulae ”, *The Astrophysical Journal*, 86, 217, 1937.

7. Abell, G., O., “The Distribution of Rich Clusters of Galaxies ”, *The Astrophysical Journal Supplement Series*, 3, 211, 1958.

8. Byram, E.T., T.A. Chubb and H. Friedman, “Cosmic X-ray Sources, Galactic and Extragalactic ”, *Science*, Vol. 152, 66B, 1966.

9. Bradt, H., W. Mayer, S. Naranan, S. Rappaport and G. Spada, “Evidence for X-Radiation from the Radio Galaxy M87 ”, *The Astrophysical Journal*, Vol.150, p.L199, 161, L1, 1967.

10. Gursky, H., E. M. Kellogg, C. Leong, H. Tananbaum and R. Giacconi, “Detection of X-Rays from the Seyfert Galaxies NGC 1275 and NGC 4151 by the UHURU

Satellite ", *The Astrophysical Journal Letters*, Vol. 165, p.L43, 1971.

11. Fritz, G., A. Davidsen, J. F. Meekins and H. Friedman, "Discovery of an X-Ray Source in Perseus ", *The Astrophysical Journal Letters*, 164, L81, 1971.

12. Leir, A. A. and S. van den Bergh, "A Study of 1889 Rich Clusters of Galaxies ", *The Astrophysical Journal Supplement Series*, Vol.34, p.381-403, 1977.

13. Sarazin, C. L., H. J. Rood and M. F. Struble, "A Table of Redshifts for Abell Clusters ", *Astronomy and Astrophysics*, Vol.108, No.2, p. L7-L10, Apr. 1982.

14. Zwicky, F., E. Herzog and P. Wild, "Catalogue of Galaxies and of Clusters of Galaxies ", Pasadena: California Institute of Technology (CIT), 1961-1968.

15. Just, K., "A Test for Evolution in Cosmology ", *The Astrophysical Journal*, 129, 268J, 1959.

16. Paal, G., "Some Remarks on Empirical Tests of Cosmology ", Communications of the Konkoly Observatory, No. 54 (Vol. IV, 12), p. 1-30, 1964.

17. Bahcall, N.A., "The Relation Between Velocity Dispersion and Central Galaxy Density in Clusters of Galaxies", *The Astrophysical Journal*, Part 1, vol. 247, p. 787-791, Aug. 1, 1981.

18. Faber, S. M. and J. S. Gallagher, "Masses and Mass-to-Light Ratios of Galaxies ", *Annual Review of Astronomy and Astrophysics*, Vol.17. (A79-54126 24-90) Palo Alto, Calif., Annual Reviews, Inc., p. 135-187, 1979.

19. Rood, H.J., "Clusters of Galaxies ", *Reports on Progress in Physics*, Vol.44, p. 1077-1079, 1081-11221981, Oct. 1981.

20. Large, M. I., D. S. Mathewson and C. G. T. Haslam, "A High-Resolution Survey of the Coma Cluster of Galaxies at 408 Mc/s ", *Nature*, Vol.183, pp. 1663, 1959.

21. Costain, A. H. Bridle and P. A. Feldman, “Decametric Radio Identification of an Extragalactic X-Ray Source ”, *The Astrophysical Journal*, Vol. 175, p.L15, 1972.

22. Baldwin, J. E. and P. F. Scott, “Extragalactic Radio Sources with Steep Low Frequency Spectra ”, *Monthly Notices of the Royal Astronomical Society*, Vol.165, p. 259-269, 1973.

23. Slingo, A., “The Structure of Origin of Radio Sources with Very Steep Spectra ”, *Monthly Notices of the Royal Astronomical Society*, Vol. 168, p. 307-330, 1974a.

24. McHardy, I.M., “4C Radio Sources in Clusters of Galaxies. III ”, *Royal Astronomical Society, Monthly Notices*, Vol. 188, p. 495-5231979, Aug. 1979.

25. Ferrari, C., F. Govoni, S. Schindler, A. M. Bykov and Y. Rephaeli, “Observations of Extended Radio Emission in Clusters ”, *Space Science Reviews*, Vol. 134, 1-4, 2008.

26. Feretti, L., R. Fusco-Femiano, G. Giovannini and F. Govoni, ”The Giant Radio Halo in Abell 2163”, *Astronomy and Astrophysics*, Vol.373, p.106-112, 2001.

27. Slee, O. B., A. L. Roy, M. Murgia, H. Andernach and M. Ehle, “Four Extreme Relic Radio Sources in Clusters of Galaxies ”, *The Astronomical Journal*, Vol. 122, Issue 3, pp. 1172-1193, 2001.

28. Röttgering, H. J. A., M. H. Wieringa, R. W. Hunstead and R. D. Ekers, “The Extended Radio Emission in the Luminous X-ray Cluster A3667 ”, *Monthly Notices of the Royal Astronomical Society*, Vol. 290, Issue 4, pp. 577-584, 1997.

29. Sijbring, L.G., “A Radio Continuum and HI Line Study of the Perseus Cluster ”, PhD Thesis, Groningen: Rijksuniversiteit, 1993.

30. Fabian, A. C., J. S. Sanders, S. Ettori, G. B. Taylor, S. W. Allen, C. S. Crawford, K. Iwasawa, R. M. Johnstone and P. M. Ogle, “Chandra Imaging of the Complex X-ray Core of the Perseus cluster ”, *Monthly Notices of the Royal Astronomical*

Society, Vol. 318, Issue 4, pp. L65-L68, 2000.

31. Felten, J. E., R. J. Gould, W. A. Stein and N. J. Woolf, "X-Rays from the Coma Cluster of Galaxies ", *The Astrophysical Journal*, Vol. 146, p.955-958, 1966.

32. Wolff, R. S., R. J. Mitchell, P. A. Charles and J. L. Culhane, "The X-ray Structure of the Perseus Cluster of Galaxies ", *The Astrophysical Journal*, Vol. 208, pt. 1, p. 1-12, Aug. 15, 1976.

33. Wu,X.P., "A Combined Analysis of Cluster Mass Estimates from Strong Lensing, X-ray Measurement and the Universal Density Profile ", *Monthly Notices of the Royal Astronomical Society*, 316, 299, 2000.

34. Finoguenov, A., T. H. Reiprich and H. Bhringer, "Details of the mass-temperature relation for clusters of galaxies ", *Astronomy and Astrophysics*, v.368, p.749-759, 2001.

35. Ota, N., T. Kitayama, K. Masai and K. Mitsuda, "L_X-T Relation and Related Properties of Galaxy Clusters ", *The Astrophysical Journal*, Vol. 640, Issue 2, pp. 673-690, 2006.

36. Markevitch, M., "The L_X-T Relation and Temperature Function for Nearby Clusters Revisited ", *The Astrophysical Journal*, Vol.504, p.27, 1998.

37. Arnaud, M. and A. E. Evrard, "The L_X-T relation and intracluster gas fractions of X-ray clusters ", *Monthly Notices of the Royal Astronomical Society*, Vol. 305, Issue 3, pp. 631-640, 1999.

38. Abell, G.O., "Clustering of Galaxies ", *Annual Review of Astronomy and Astrophysics*, Vol. 3, p.1, 1965.

39. Abell,G.O, "Clusters of Galaxies ", *Galaxies and the Universe*, Allan Sandage, Mary Sandage, and Jerome Kristian (editors), Published by the University of Chicago Press (Stars and Stellar Systems. Vol. 9), Chicago, IL USA, p.601, 1975.

40. Bautz, L. P. and W. W. Morgan, “On the Classification of the Forms of Clusters of Galaxies ”, *The Astrophysical Journall*, Vol. 162, p.L149, 1970.

41. Rood, H. J. and G. N. Sastry, “Tuning Fork, Classification of Rich Clusters of Galaxies ”, *Publications of the Astronomical Society of the Pacific*, Vol. 83, No. 493, p.313, 1971.

42. Oemler, A. Jr., “The Systematic Properties of Clusters of Galaxies. Photometry of 15 Clusters ”, *Astrophysical Journal*, Vol. 194, pp. 1-20, 1974.

43. Morgan, W.W., “The Classification of Clusters of Galaxies ”, *Proceedings of the National Academy of Sciences of the United States of America*, Vol. 47, Issue 7, pp. 905-906, 1961.

44. Ehle, M., I. de la Calle, M. Daz Trigo, R. Gonzlez Riestra, N. Loiseau and P. Rodrguez, “XMM-Newton Users Handbook ”, version 2.6, 2008.

45. Snowden, S. L. and K. D. Kuntz, “The XMM-Newton ABC Guide: An Introduction to XMM-Newton Data Analysis ”, version 2.01, 2004.

46. All SAS Threads, *http://xmm2.esac.esa.int/sas/8.0.0/documentation/*.

47. De La Calle, I. and Loiseau, N., (editors), “User Guide to the XMM-Newton Science Analysis System ”, issue 5.0, 2008.

48. Arnaud, K., B. Dorman and C. Gordon, ”Xspec An X-Ray Fitting Package”, user’s guide version 12.3.1, 2007.

49. The Astrophysical Plasma Emission Code, *http ://cxc.harvard.edu/atomdb/ sources_ apec.html*.

50. Nousek, J. A., and D. R. Shue, “χ^2 and C Statistic Minimization for Low Count Per Bin Data ”, *The Astrophysical Journal*, 342:1207-1211, 1989.

51. Xspec and Low Count Spectra, *http ://astrophysics.gsfc.nasa.gov./XSPECwi−ki/low_count_spectra.*

52. Snowden S. L. and K. D. Kuntz, "Cookbook for Analysis Procedures for XMM-Newton EPIC MOS Observations of Extended Objects and The Diffuse Background ", version 2.0, 2007.

53. Hasinger, G., "Cosmic X-Ray Background ", Trumper, J. E. and Hasinger, G. (editors) in *The Universe in X-Rays*, pp. 456-475, Astronomy and Astrophysics Library, Springer 2008.

54. Lumb, D., "EPIC Background Files XMM-SOC-CAL-TN-0016 ", issue 2.0, 2002.

55. Snowden, S. L., M. R. Collier and K. D. Kuntz, "XMM-Newton Observation of Solar Wind Charge Exchange Emission ", *The Astrophysical Journal*, Vol. 610, Issue 2, pp. 1182-1190, 2004.

56. Bourdin, H., J. L. Sauvageot, E. Slezak, A. Bijaoui and R. Teyssier, "Temperature Map Computation for X-ray Clusters of Galaxies ", *Astronomy and Astrophysics*, Vol.414, p.429-443, 2004.

57. Adami, C., A. Mazure, P. Katgert and A. Biviano, "The ESO Nearby Abell Cluster Survey VII. Galaxy Density Profiles of Rich Clusters of Galaxies ", *Astronomy and Astrophysics*, 336, 63-82, 1998.

58. Gonzalez, A. H., D. Zaritsky and A. I. Zabludoff, "A Census of Baryons in Galaxy Clusters and Groups ", *The Astrophysical Journal*, 666: 147-155, 2007.

59. Girardi, M., A. Biviano, G. Giuricin, F. Mardirossian and M. Mezzetti, "Velocity Dispersions in Galaxy Clusters ", *The Astrophysical Journal*, 404:38-50, 1993.

60. Sivanandam, S., A. I. Zabludoff, D. Zaritsky, A. H. Gonzalez and D. D. Kelson, "The Enrichment of the Intracluster Medium ", *The Astrophysical Journal*, 691:1787-1806, 2009.

61. Mohr, J. J., M. J. Geller and G. Wegner, “A Dynamical Analysis of the Poor Galaxy Clusters Abell 2626 and Abell 2440 ”, *The Astrophysical Journal*, Vol.112, No.5, 1996.

62. Valotto, C. A., H. Muriel, B. Moore, and D. G. Lambas, “Faint Galaxy Population in Clusters: X-Ray Emission, cD Halos and Projection Effects ”, *The Astrophysical Journal*, 601:67-73, 2004.

63. Kolokotronis, V., S. Basilakos, M. Plionis and I. Georgantopoulos, “Searching for Cluster Substructure Using APM and ROSAT Data ”, *Monthly Notices of the Royal Astronomical Society*, Vol.320, Issue 1, pp. 49-60, 2001.

64. Krick, J. E., R. A. Bernstein and K. A. Pimbblet, “Diffuse Optical Light in Galaxy Clusters I. Abell 3888 ”, *The Astronomical Journal*, 131:168-184, 2006.

65. Struble, M. F. and C. Ftaclas, “The Intrinsic Shape of Clusters of Galaxies: Correlations Among Flattening, Richness and Velocity Dispersion ”, *The Astronomical Journal*, Vol. 108, No.1, p. 1-23, 1994.

66. Gutierrez, K. and H. Krawczynski, “The Off-Axis Galaxy Cluster Merger A115 ”, *The Astrophysical Journal*, 619:161-168, 2005.

67. Feretti, L., I. M. Gioia, G. Giovannini, L. Gregorini and L. Padrielli, “High Resolution Radio and X-Ray Observations of A115 ”, *Astronomy and Astrophysics*, Vol.139, No.1, p. 50-54, 1984.

68. Riley, J. M. and G. G. Pooley, “Observations of 31 Extragalactic Radio Sources with the Cambridge 5-km Telescope at 5 GHz ”, *Royal Astronomical Society, Memoirs*, Vol.80, pt. 3, p. 105-137, 1975.

69. Rakos, K. D., J. M. Schombert, A. P. Odell and S. Steindling, “Cluster Populations in A115 and A2283 ”, *The Astrophysical Journal*, 540:715-725, 2000.

70. Abell, G. O., H. G. Jr. Corwin and R. P. Olowin, “A Catalog of Rich Clusters of

Galaxies ", *The Astrophysical Journal Supplement Series*, 70:1-138, 1989.

71. Einasto, M., J. Einasto, E. Tago, V. Mller and H. Andernach, "Optical and X- Ray Clusters as Tracers of the Superclusters- Void Network I. Superclusters of Abell and X- Ray Clusters ", *The Astronomical Journal*, 122: 2222-2242, 2001.

72. David, L. P., A. Slyz, C. Jones, W. Forman, S. D. Vrtilek and K. A. Arnaud, "A Catalog of Intracluster Gas Temperatures ", *The Astrophysical Journal*, 412, 479, 1993.

73. Pearce, F. R., P. A. Thomas and H. M. P. Couchman, "Head-On Mergers of Systems Containing Gas ", *R.A.S. Monthly Notices*, Vol.268, No.4, P. 953, 1994.

74. Maurogordato, S., "Merging clusters of galaxies ", *Bernards Cosmic Stories, Conference*, Valencia, 2006

75. Krick, J. E. and R. A. Bernstein, "Diffuse Optical Light in Galaxy Clusters II. Correlations with Cluster Properties ", *The Astronomical Journal*, 134:466-493, 2007.

76. Böhringer, H., P. Schuecker, L. Guzzo, C. A. Collins, W. Voges, R. G. Cruddace, A. Ortiz-Gil, G. Chincarini, S. De Grandi, A. C. Edge et al., "The ROSAT-ESO Flux Limited X-Ray Galaxy Cluster Survey", *Astronomy and Astrophysics*, 425, 367-383, 2004.

77. Snowden, S. L., R. F. Mushotzky, K. D. Kuntz and D. S. Davis, "A Catalog of Galaxy Clusters Observed by XMM-Newton ", *Astronomy and Astrophysics*, 478, 615-658, 2008.

78. Shibata, R., H. Honda, M. Ishida, T. Ohashi and K. Yamashita, "Temeperature Variation in the Cluster of Galaxies Abell 115 Studied with ASCA ", *The Astrophysical Journal*, 524:603-611, 1999.

79. Barrena, R., W. Boschin, M. Girardi and M. Spolaor, "The Dynamical Status of the Galaxy Cluster Abell 115 ", *Astronomy and Astrophysics*, 469, 861-872, 2007.

80. Schechter, P., L. and P. J. E. Peebles “On the Significance of the Luminosities of First-Ranked Members of Sparse Groups of Galaxies ”, *The Astrophysical Journal*, Vol. 209, pp. 670-677, 1976.

81. Dupke, R. A. and R. E. III White, “Metallicity Gradients in the Intracluster Gas of Abell 496 ”, *The Astrophysical Journal*, V.537, Issue 1, pp. 123-133, 2000.

82. Arnaud, M., S. Majerowicz, D. Lumb, D. M. Neumann, N. Aghanim, A. Blanchard, M. Boer, D. J. Burke, C. A. Collins, M. Giard et al., “XMM-Newton observation of the distant (z=0.6) galaxy cluster RX J1120.1+4318 ”, *Astronomy and Astrophysics*, V.390, p.27-38, 2002.